Synthesis and Characterization of Ensembles Containing Zinc Oxide Nanocrystals and Organic or Transition Metal Dyes to Probe the Early Events in a Dye-Sensitized Solar Cell.

A DISSERTATION
SUBMITTED TO THE FACULTY OF THE GRADUATE SCHOOL
OF THE UNIVERSITY OF MINNESOTA
BY

Julia Erin Saunders

IN PARTIAL FULFILLMENT OF THE REQUIREMENTS
FOR THE DEGREE OF
DOCTOR OF PHILOSOPHY

Wayne L. Gladfelter

August 2011

Acknowledgements

I sincerely thank my advisor, Wayne Gladfelter, for all he has done during my time at the University of Minnesota. Under his guidance, I developed my scientific acumen while learning from him what it takes to be a successful professional. I am also grateful to Prof. David Blank and Prof. Kent Mann for their scientific advice during my graduate school career.

I am thankful for the generous financial support from the Department of Energy, Basic Sciences Division, the University of Minnesota Materials Research Science and Engineering Center (MRSEC), the Minnesota Initiative for Renewable Energy and the Environment (IREE), the National Renewable Energy Laboratory (NREL) and the University of Minnesota Department of Chemistry.

Lastly, I thank my family for their unwavering support, honesty, humor and perspective. I'm a lucky gal.

To Ben,
of course

Table of Contents

List of Tables

List of Figures

Chapter 1: Introduction

1.1 Renewable Energy

Prior to the 1970's, alternative sources of energy in the United States consisted mainly of holdovers from the Industrial Revolution of the 1800s such as hydropower, the combustion of biomass, and geothermal energy. The reliance on these energy sources was geographically dependent and, even then, was only successful in areas with a strong local demand. Not until the financial crisis caused by the 1973 Organization of the Petroleum Exporting Countries (OPEC) oil embargo was there a more wide-spread demand for carbon-free energy sources. The skyrocketing oil prices coupled with an uncertain supply, motivated the original call for increasing research into alternative energy options. Currently, there is still a desire to curtail the United States' reliance on foreign oil, but emphasis for developing alternative energy sources today relies heavily on research that links an increase in carbon dioxide production to an increase in global warming.

It is unlikely that one type of alternative energy will provide enough power to completely replace our dependence on fossil fuels for energy, but the Department of Energy, along with numerous other advisory and research boards, is hopeful that a combination of nuclear energy, energy from biofuels, hydroelectric power, geothermal power, photovoltaic energy, and wind power may be enough to meet our energy demands. Only 7% of all energy consumed in the United States in 2008 came from renewable resources, and of that, only 1% came from photovoltaics (PV).[1] Although solar cells are robust, do not require a specific geographical location and can conveniently be placed on rooftops, the primary reason for their limited use is due to their high cost. The

average cost for PV electricity is approximately one order of magnitude higher than the average cost for electricity obtained from fossil fuels.[2] The past thirty years have seen a 20% decrease in PV module cost for each doubling of production but, even so, to achieve massive implementation of PV devices, costs need to be substantially decreased. One way to combat the price disparity between energy obtained from fossil fuels and that from solar cells is to increase the efficiency of the PV devices so that the same implementation costs produce more electricity.

1.2 Photovoltaic Devices

Conventional solar cells, such as those made from crystalline silicon, maintain performance over many decades and account for over 80% of all PV devices produced. Laboratory modules have an energy conversion efficiency as high as 24.4% while their commercial counterparts have a maximum efficiency around 16%.[2] The overall efficiency of a device is dependent on the combined efficiencies of three factors: light absorption, charge separation and charge transport. Inorganic semiconductors have been established as useful materials to use in photovoltaic devices. Semiconductors absorb light that is greater than or equal to the energy that separates the electron filled valence band from the empty conduction band, or band gap (E_G). Silicon has a band gap of 1.1 eV which means electrons (e^-) are promoted from the valence band to the conduction band, leaving behind positively charged holes (h^+), when $h\upsilon \geq 1.1$ eV (Figure 1.1). Recombination of the electron-hole pairs is minimized when an external electric field is applied and the electrons migrate through the conduction band in one direction while the

holes migrate through the valence band in the opposite direction. Efficient transport is achieved only for defect-free crystalline materials that have long coherent lengths. This requirement of high-quality material is the primary reason solar cell production costs are high. If, however, the light absorption, charge separation and charge transport processes do not all occur in the same pristine material, but rather in different, less expensive and easily processed materials, the overall production costs of solar cells would decrease while maintaining device efficiency. This is the premise of dye-sensitized solar cells (DSSCs) and is the motivation behind the research presented herein.

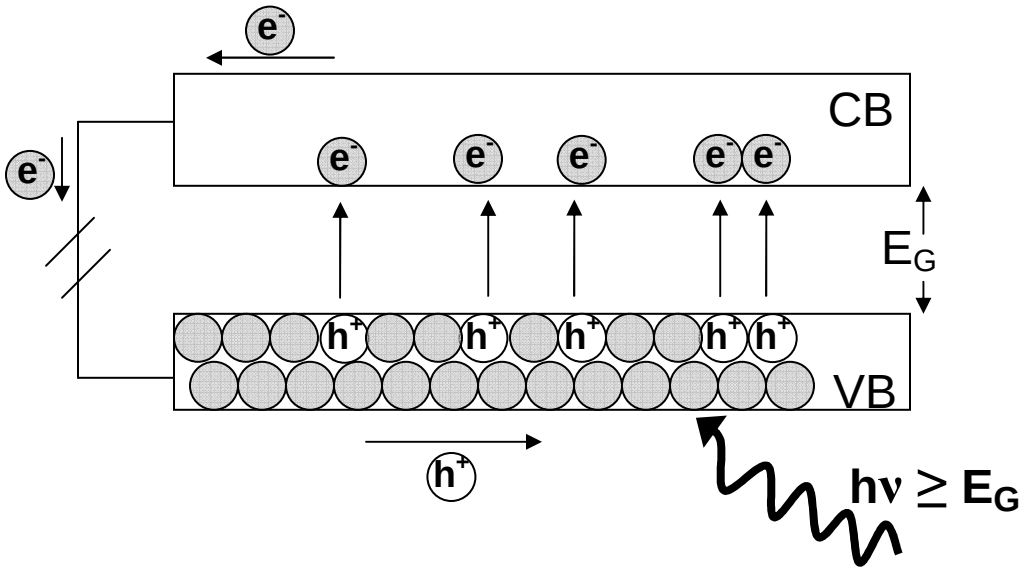

Figure 1.1 Schematic of how a semiconductor transforms light into electrical energy as described above.

1.3 Research Goals and Accomplishments

The goal of this research was to synthesize well-defined dyads of ZnO nanocrystals and visible-light absorbing dyes to better understand the specific charge transfer events that occur within a dye-sensitized solar cell. Research was initially directed towards understanding ZnO nanocrystals, including their syntheses, growth and possible formation from zinc hydroxide. Later research focused on synthesizing and fully characterizing ZnO:dye ensembles using a variety of spectroscopic techniques; dye attachment was verified and quantified while the quenching mechanism for one of the ensembles was explored in detail. Finally, ultra-fast laser spectroscopy was used to observe the initial electron transfer events of the ensemble.

1.4 Thesis Organization

Chapter 2 establishes the necessary background and motivation for this thesis project. An overview of DSSCs is included, as well as a summary of the sensitization of semiconducting nanocrystals.

Chapter 3 describes the experiments conducted with visible-light absorbing dyes (both organic and metal-centered dyes) on ZnO nanocrystals to elucidate the binding and static quenching behavior of the system. It also includes modeling that corroborates the results.

Chapter 4 details the electron transfer dynamics of the terthiophene dye on ZnO nanocrystals obtained through time-resolved experiments using ultrafast spectroscopy. Much of the research described in this chapter involved collaboration with Adam Huss of David Blank's group. Included is the spectroelectrochemistry of the terthiophene dye which was carried out with assistance from members of Kent Mann's group, specifically Darren Ceckanowicz.

Chapter 5 contains relevant research pertaining to ZnO, including synthetic methods, spectroscopy, observations of growth and the synthesis of $Zn(OH)_2$.

Chapter 2: Background on Dye-Sensitized Solar Cells

In general, the operation of a photovoltaic device is divided into three main steps: **light absorption, charge separation, and charge transport/collection**. The overall efficiency of a device is dependent on the combined efficiency of each of the three steps. An important feature of dye-sensitized solar cells is the unique ability to manipulate and maximize all three of the abovementioned components with proper material selection and device construction.

2.1 Concept for Semiconductor Sensitization.

The energy available to us from the sun is different for each specific location on earth and is dependent on air quality, season, latitude, altitude, weather and time of day. The American Society for Testing and Materials (ASTM) along with research and development laboratories developed a standard terrestrial solar spectral irradiance distribution to provide a common reference for evaluating PV materials (Figure 2.1).[3] The atmospheric conditions chosen were considered to be a reasonable average for the lower 48 states of the United States over the course of a year. The figure illustrates the amount of energy available to us from the sun at varying wavelengths. Due to their large band gap energy, TiO_2 (3.2 eV, ~ 388 nm) and ZnO (3.37 eV, ~ 368 nm) are only able to absorb high energy, ultra-violet light, which accounts for less than 5% of the energy available from the sun. If, however, a molecule that absorbs visible, or even infrared, light is attached to the semiconductor, the amount of light that can be absorbed is expanded which increases the efficiency of the system.

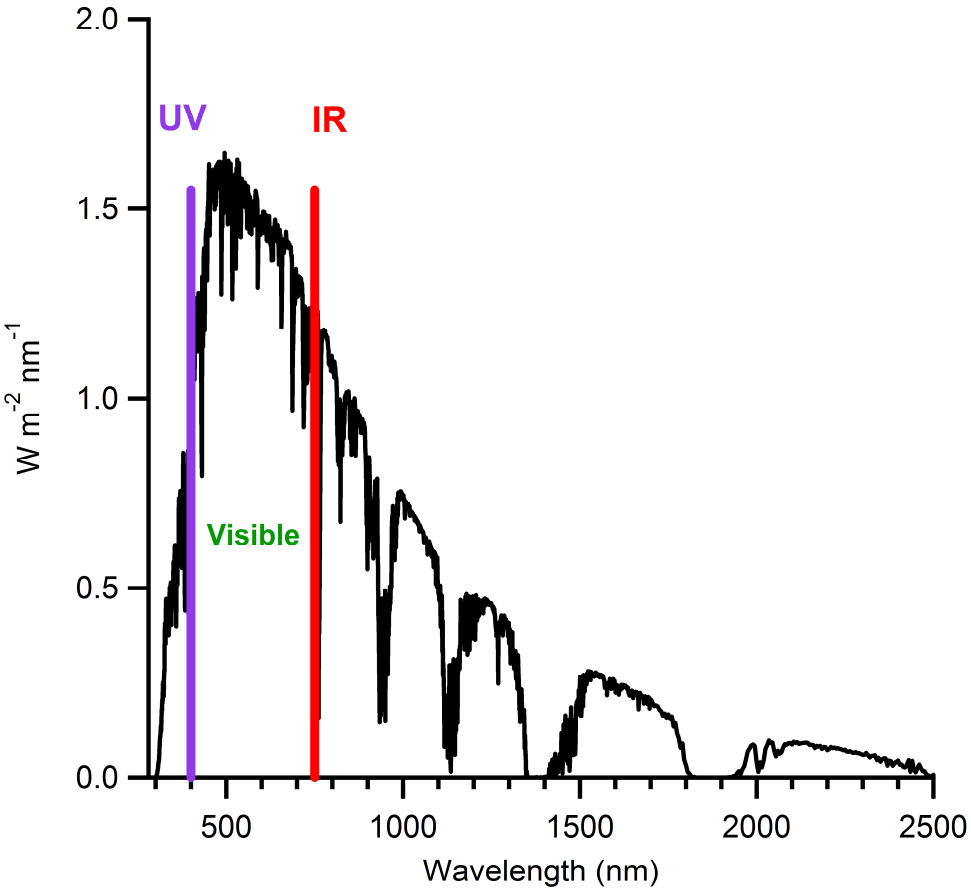

Figure 2.1 Standard total spectral irradiance at air mass 1.5 as a function of wavelength under specific atmospheric conditions which describe the standard US atmosphere as designated by the American Society for Testing and Materials (ASTM G-173-03).[3]

2.2 History.

The first significant study of semiconductors sensitized by dyes occurred in the 1870's by Vogel as he explored silver halide emulsions used in photography. With the addition of dyes to the emulsions, Vogel was able to extend significantly the photoresponse of the silver halide into the red and infrared, thereby introducing broad-spectrum photographic film.[4] Research on sensitization of semiconductors for use in solar

cells began in the 1960's where it was noted that dyes should be adsorbed to the semiconducting surface in a closely packed monolayer to increase efficiency.[5-8] Energy conversion efficiencies of solar cells comprised of sensitized semiconductors remained <1% until Grätzel and O'Reagan's successful work in 1991 in which they achieved a conversion efficiency greater than 7% as they changed the smooth surface of the semiconductor into a rough TiO_2 nanoparticle film with ~1000 times the surface area of the original film.[9] In 1993, Nazeeruddin and Grätzel[10] increased the efficiency to 10% but little has been gained in terms of efficiency since then, with 11.1% reached in 2006.[11] The solar cell originally described by Grätzel and coworkers is referred to as a *dye-sensitized solar cell* (DSSC) or *Grätzel cell*.

2.3 Operation of Dye-Sensitized Solar Cells.

A simple schematic of a DSSC is shown (Figure 2.2). The major component is a thick (typically 10 - 20 μm), porous film made from crystalline nanocrystals (typically 5-30 nm in diameter) of a high band gap energy material (typically TiO_2 or ZnO) to which a monolayer of sensitizer or visible-light absorbing dye is adsorbed. The entire component is submerged in a redox couple electrolyte, such as the iodide/triiodide couple, that penetrates the network of nanocrystals on the film. The cell is contained on the front by a transparent conducting oxide coated glass substrate and on the back by a catalyst (often platinum) coated glass substrate. An external load is connected to the electrodes to complete the circuit.

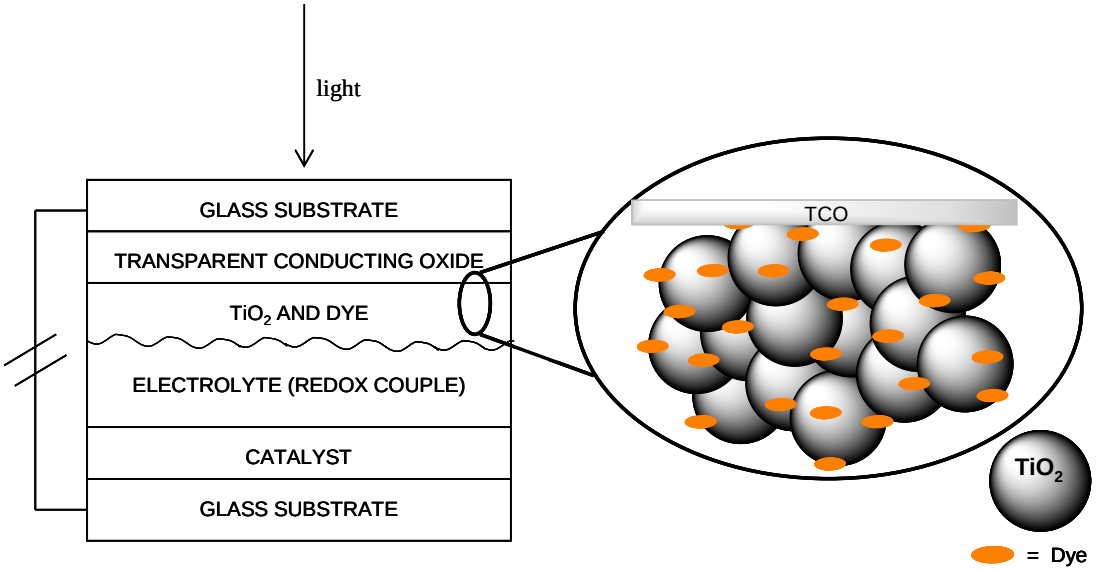

Figure 2.2 Schematic representation of a DSSC including a magnified image of the TiO_2 film to which dye molecules are adsorbed.

In a sensitized solar cell, the dye molecules are responsible for light absorption. However, a monolayer of molecules on a flat surface, such as a smooth electrode, are capable of absorbing a small percentage of the incoming light. More light can be absorbed if the thickness of the dye layer is increased, but only those molecules in direct contact with the semiconductor can contribute to the charge separation step. Grätzel and O'Reagan's contribution was to increase the TiO_2 surface area by substituting a highly porous, nanocrystalline film for a smooth film. With a monolayer of dye now adsorbed to the surface of the nanocrystalline film, approximately 99% of the light could be absorbed and all adsorbed dye molecules were in direct contact with the semiconductor.[9]

Figure 2.3 depicts an energy diagram for each interface found in a generic DSSC. Light passes through the working electrode of a transparent conducting oxide and through

the nanocrystalline TiO_2 film. If the energy of the incoming light is one that can be absorbed by the dye, based on the dye's highest occupied molecular orbital (HOMO) and lowest unoccupied molecular orbital (LUMO), an electron will be promoted from the molecule's ground state into its excited state. If the excited electrons in the LUMO are high enough in energy, they are injected into the conduction band of the TiO_2. Injected electrons percolate through the semiconductor network to reach the transparent conducting oxide photoanode where they are passed through a load to reach the cathode. An electrolyte containing a redox couple is present in the cell to be reduced by the cathode, completing the cell cycle. Another purpose of the redox couple is to prevent immediate charge recombination of the electron in the TiO_2 conduction band to the ground state of the dye by reducing the oxidized dye molecule. Charge separation within the cell is supported by a kinetically slow interfacial recombination rate between the injected electron and the oxidized dye as well as the presence of the electrolyte around the nanocrystal to neutralize any influential electric field.[5] The driving force for the cell is the potential difference between the conduction band edge of the semiconductor and the redox potential of the electrolyte.[12]

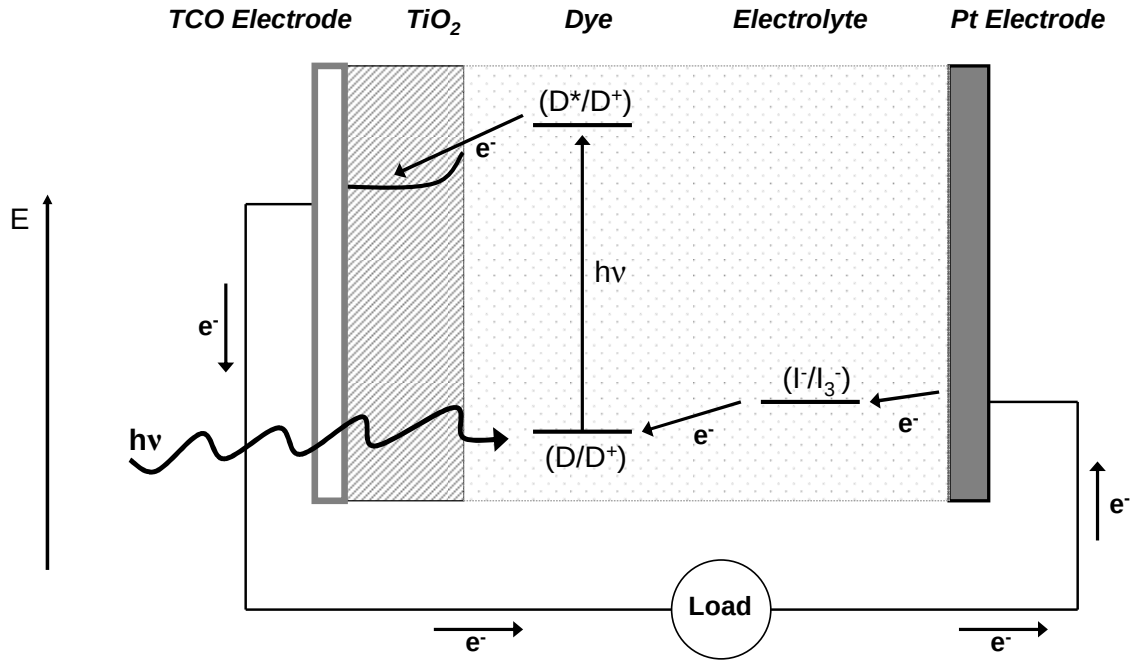

Figure 2.3 Schematic energy diagram (not to scale) of the interfaces involved with electron movement in a DSSC.

The cycle can be summarized using chemical reactions as shown in the following equations:[13]

$D + h\upsilon \longrightarrow D^*$	Absorption	(eq. 2.1)
$D^* \longrightarrow D^+ + e^-(TiO_2)$	Electron injection	(2.2)
$2D^+ + 3I^- \longrightarrow 2D + I_3^-$	Dye reduction	(2.3)
$I_3^- + 2e^-(Pt) \longrightarrow 3I^-$	Redox pair reduction	(2.4)
$e^-(Pt) + h\upsilon \longrightarrow e^-(TiO_2)$	Overall cell	(2.5)

2.4 Materials and Optimization Attempts for Dye-Sensitized Solar Cells.

The greatest advantage DSSCs offer the photovoltaic community, is the unique ability to tailor and control the light absorption, charge separation, and charge transport properties of a device by judiciously selecting the appropriate materials. The rest of this chapter examines the first two steps in detail, as they are most relevant to the original research presented in the subsequent chapters of this thesis.

2.4.1 Sensitizers and Light Absorption.

There are several issues to consider when choosing an appropriate sensitizer. Ideally, the sensitizer would absorb all light below ~900 nm to optimize light absorption. Its excited state redox potential must be sufficiently high that the transfer of electrons from the excited state of the dye to the conduction band of the semiconductor is energetically and kinetically favorable but not too high that the kinetics lie within the Marcus inverted region. The process of electron injection must be fast enough to compete with other, unwanted relaxation or reaction pathways. The dye must be able to attach to the surface of the semiconductor with suitable anchoring groups. Finally, the dye must be stable enough to undergo repeated redox cycles for long-term use.[14] Although organic dyes have been explored and will be discussed later, the best photovoltaic performance so far has come from robust ruthenium polypyridyl complexes.[9-11,14,15] Currently, the N3 and N719 dyes, shown in Figure 2.4, are seen as standards in the field.[16]

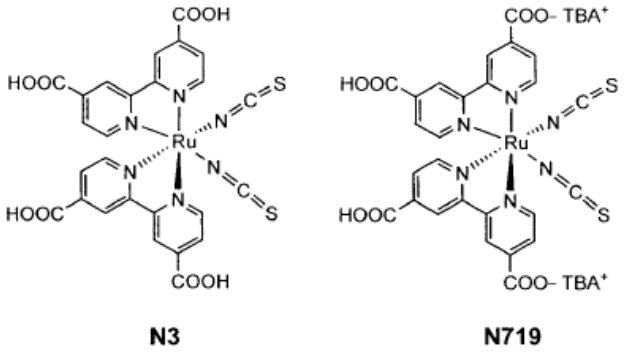

Figure 2.4 Molecular structure of cis-di(thiocyanato)bis(2,2′-bipyridyl)-4,4′-dicarboxylate ruthenium(II) as the protonated, N3 form and as the deprotonated, N719 form.

In octahedral complexes such as $RuCl_6^{4-}$ or $Ru(NH_3)_6^{2+}$ ruthenium(II) has a low-spin, d^6 electron configuration as shown in Figure 2.5. When excited, it undergoes a metal centered (MC) transition and an electron is promoted from the dπ orbital into the higher energy dσ* orbital. If the ruthenium is coordinated to a bipyridine ligand, excitation of the molecule leads to promotion of a t_{2g}-like metal electron into the lower-lying π* orbital of the ligand instead of the higher energy e_g-like orbital of the metal and is labeled a metal-to-ligand charge transfer (MLCT). In the ruthenium polypyridyl case, the process has been extensively studied[17-21] and is well understood, providing further motivation for their use in DSSCs. Polypyridine ligands are light absorbing, electron accepting and can be modified with substituents. Modifications can be made to alter the attachment chemistry, change the distance from the metal center to the semiconductor, and control the excited state reduction potential of the molecule in an effort to best match the energy of the ligand's LUMO with the conduction band energy of the semiconductor.

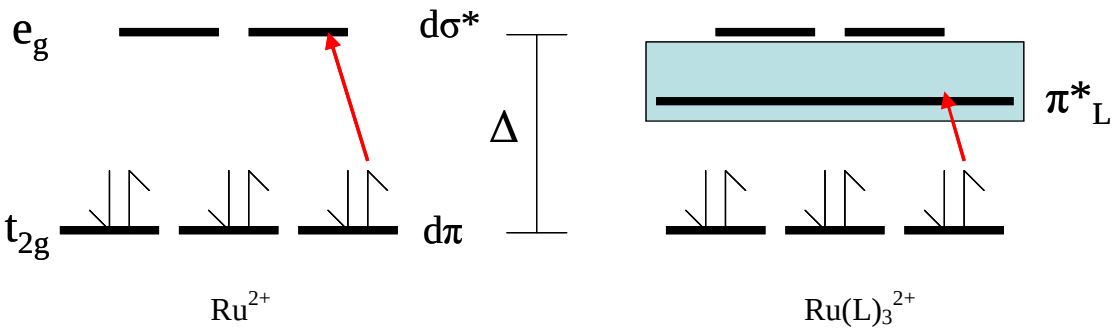

Figure 2.5 Energy diagram illustrating the metal centered transition of Ru^{2+} and the metal-to-ligand charge transfer transition of ruthenium polypyridyl.

In early experiments, sensitizers were physisorbed to semiconductor films by dipping the substrate into a solution of the dye and letting it air dry. It was quickly realized that controlling the binding process was important and by the 1970s dyes were prepared with specific functional groups (linkers) that would allow them to be covalently bound to semiconductor surfaces.[22] This led to a more even distribution of dyes on a surface, better surface coverage, and an increased stability of the dyes on the surface (minimal desorption). Foremost, it was realized that the covalent bond increases the electronic coupling strength between the molecular orbital of the dye and the semiconductor levels, allowing for faster rates of injection.[23] Phosphonates and carboxylic acid derivatives, such as amides, carboxylates, esters and acid chlorides, dominate the literature as anchoring groups of choice for metal oxide substrates but amines, silanes, and ethers have also been used.[14,24-26] All of the listed functional groups react with a semiconductor surface, forming covalent bonds. For carboxylic acid groups,

a variety of binding modes have been characterized[26] while equilibrium binding constants ranging from 2000 to 3 x 10^5 M^{-1} were recorded.[26-31]

Metal-free organic dyes have also found a place in semiconductor sensitization due, in part, to the high cost of ruthenium but more for their ease of syntheses, high extinction coefficients, and more options for light absorption.[32] Major drawbacks include molecular instability over time, sharp absorption bands in the visible region that limit the percentage of light that can be used,[33] and short excited state emission lifetimes.[34-36] Using oligoenes (Figure 2.6), Arakawa and coworkers were the first to make significant advancements in the use of organic dyes for DSSCs[37,38] with similar research conducted by Yanagida and coworkers[39] and Kim and coworkers.[40] The dialkylaminophenyl groups of these molecules serve as the electron donating groups and the cyanoacrylic acid group directs the electron to the attached semiconductor and serves as the linking group.

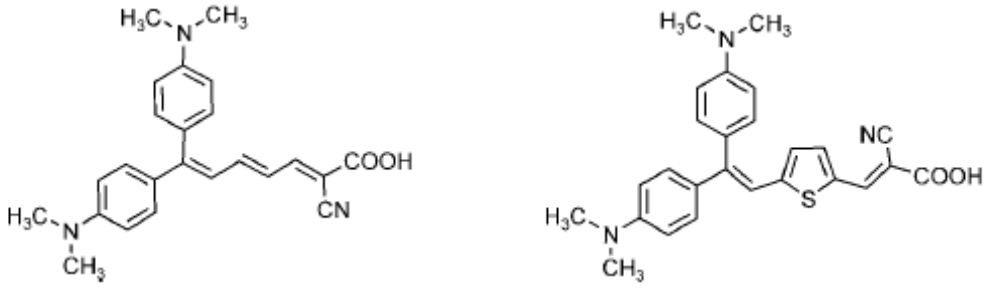

(a) **(b)**

Figure 2.6 Molecular structure of 2-cyano-7,7-bis(4-dimethylaminophenyl)hepta-2,4,6-trienoic acid[37,39] **(a)** and 3-{5-[2,2-bis(4-dimethylaminophenyl)vinyl]-thiophene-2-yl}-2-cyano-acrylic acid[38] **(b).**

Porphyrins[41-46] and coumarins, with and without cyanoacrylic acid groups, [35,38,47-49] have been used to sensitize semiconductors with reasonable success. The main

drawbacks to using coumarin molecules include short excited-state lifetimes and higher rates of charge recombination due to their strong intermolecular π-π interactions[32] while chemical instability, narrower absorption bands and lengthy syntheses are associated with prophyrins.[42]

Thiophenes have been recognized for their sensitizing potential for a variety of reasons.[50] The chemistry is well established and includes many ways to add or alter substituents, subsequently controlling the electronic properties of the molecule and making it an attractive choice for matching sensitizer to semiconductor energy levels.[51-54] Oligothiophenes are recognized for their stability in various oxidation states and for their excellent charge transport properties, attributed to a stabilization of the conjugated chain by the sulfur atoms. Another advantage of using terthiophenes is that they tend to have broad absorbance spectra at longer wavelengths, stemming from the reduced LUMO energy related to the number of conjugated π bonds. An example of their stability in DSSCs under both thermal and light stresses was illustrated by Qin *et al*. with a novel organic dye (Figure 2.7)[55] although many researchers have used them as sensitizers in DSSC-type applications.[28,33,50,56-61]

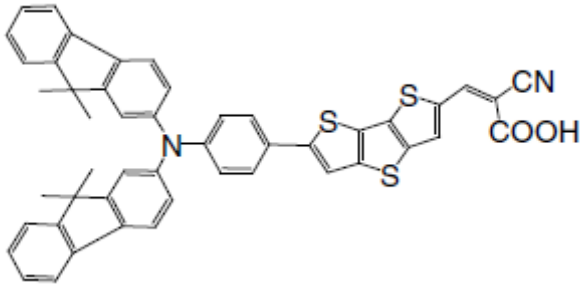

Figure 2.7 Molecular structure of 3-{6-[*N*,*N*-bis(9,9-dimethylfluoren-2-yl)phenyl]dithieno[3,2-*b*;2′,3′-*d*]thiophen-2′-yl}-2-cyanoacrylic acid.[55]

2.4.2 Charge Separation.

The charge separation component of a DSSC occurs at the dye-semiconductor interface after the sensitizer has absorbed the necessary amount of energy to excite an electron. If the process is energetically favorable, the electron will be transferred to the semiconductor, physically separating it from the dye. The kinetics and mechanism for electron injection are strongly dependent on the conduction and valence band energies of the semiconductor as well as the excited state reduction potential of the dye (Figure 2.8). Electron injection (charge separation) is achieved primarily from the enthalpic difference between the LUMO energy of the dye and the conduction band of the semiconductor coupled with the difference between the HOMO of the dye and the redox energy of the electrolyte.[12] Entropic factors associated with the high density of states in the semiconductor compared with the relatively small amount of dye on the surface leads to a charge separation driving force of approximately 0.1 eV as determined by Cahen *et al.*[12]

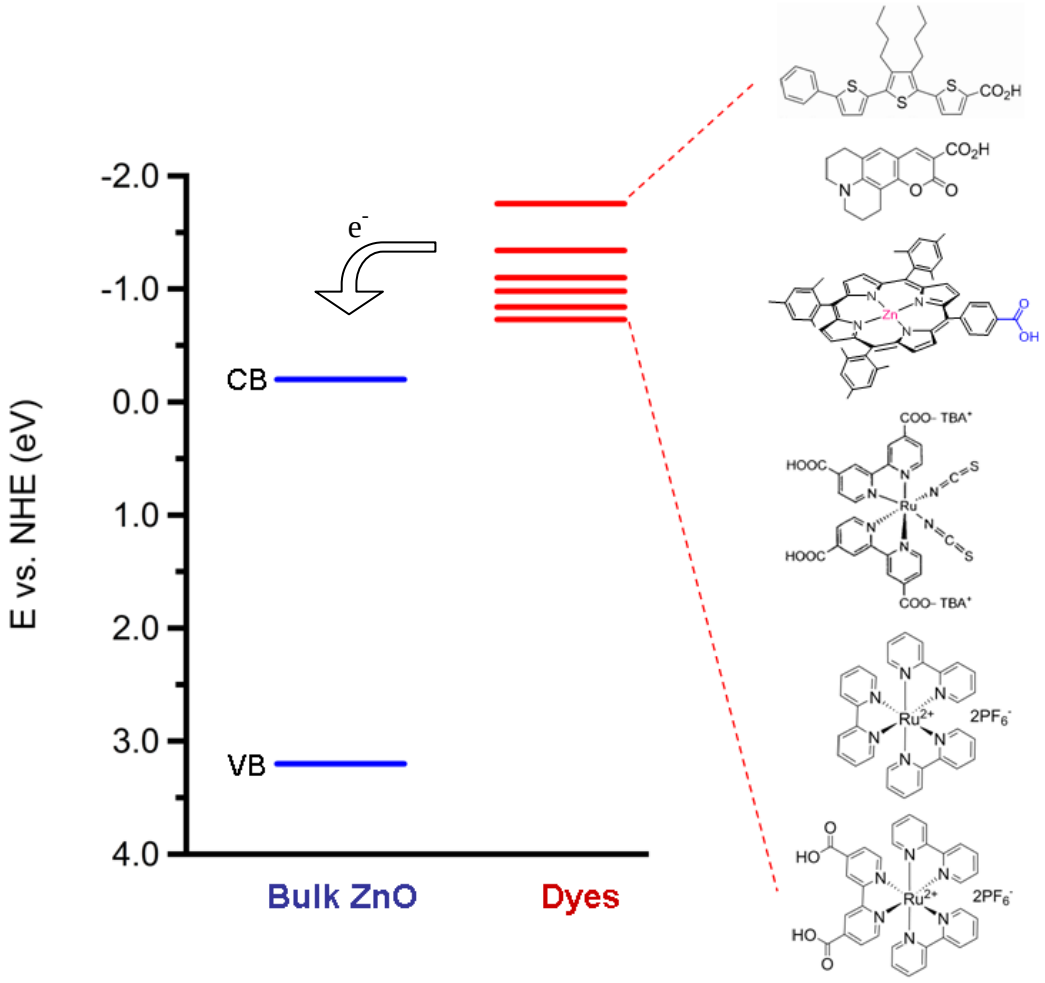

Figure 2.8 Energy diagram (eV) vs. NHE of the conduction and valence band energies of bulk ZnO compared to the excited state reduction potentials of six dyes: a phenyl terthiophene carboxylic acid, Coumarin 343, a zinc porphyrin carboxylic acid, N719, tris(bipyridine) ruthenium(II) and a carboxylic acid substituted tris(bipyridine) ruthenium(II).

Although the mechanism for charge separation in a DSSC is straight-forward, the kinetics are not. Despite numerous experimental and computational efforts, complications

arising from surface heterogeneity of the semiconducting film have made results difficult to interpret.[62-65] Rates of injection vary between <100 fs and hundreds of picoseconds and are sensitive to preparation conditions of the DSSC.[66-72] Although there are disagreements regarding the transient spectroscopy assignments,[73-76] the interfacial electron transfer process is one of the fastest chemical processes known. Researchers have used colloidal dispersions of semiconductors in an effort to mitigate heterogeneous surface issues frequently associated with the disagreement in injection timescales but this topic will be discussed in further detail in Section 2.5. For the remainder of this section, we will consider semiconductor films only. Hupp and coworkers compiled the most current literature data measuring the half-life time of each process involved in a working DSSC so as to better grasp the competing dynamics (Figure 2.9).[77] In each case, the desirable process occurred faster than its corresponding competitive process, shown in the same color. An important point, as made by Hupp, is there is little kinetic overlap in a DSSC so shifting, for example, the conduction band energy negatively would *not* increase charge collection efficiency.[77] This balance of rates can also be described using Marcus Theory.

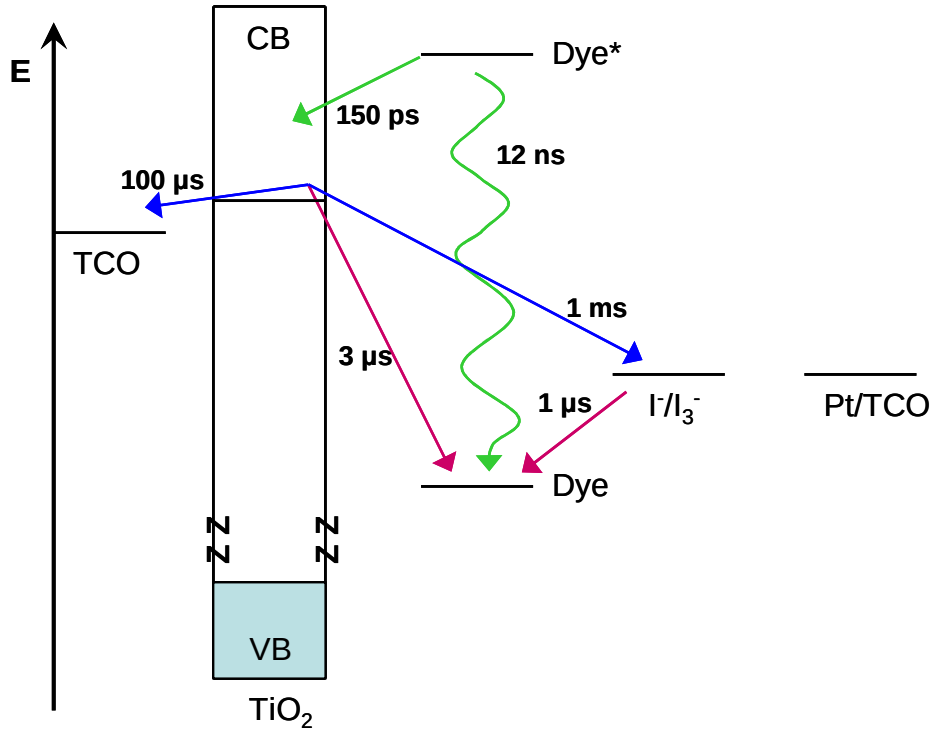

Figure 2.9 Electron dynamics of a DSSC with half-life times listed for each process.

Marcus Theory explains that the rate of electron transfer is dependent on the Gibbs free energy (ΔG^0) of the system. Marcus solved for the crossing point of the two parabolas, each representing the potential energy of the reactants and products involved in an electron transfer process (Figure 2.10).

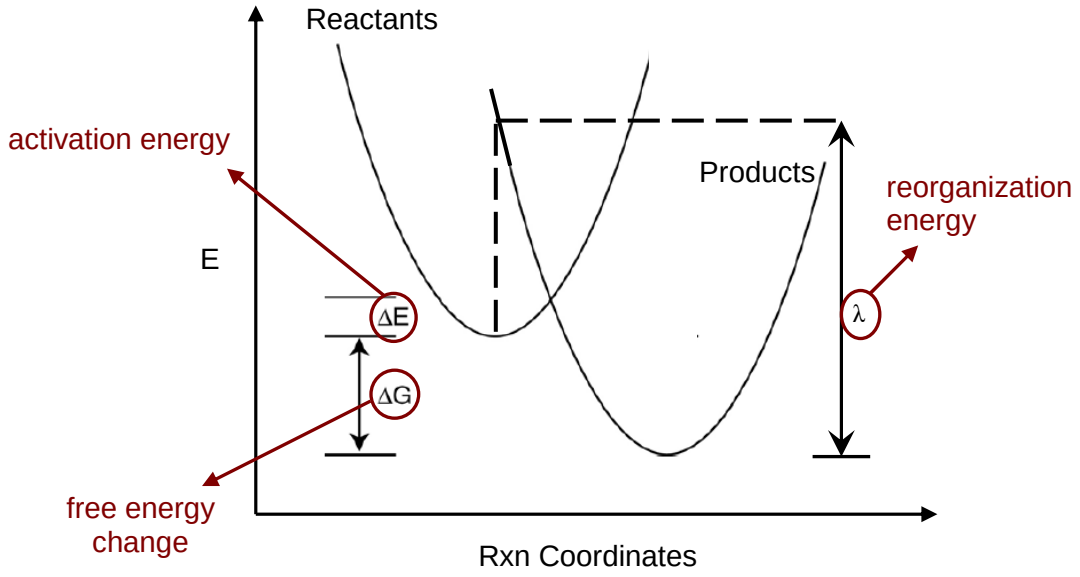

Figure 2.10 Schematic representing the potential energy surface for the nuclear motion the reactants (left parabola) and products (right parabola) as a function of the reaction coordinate for electron transfer within the Marcus normal region.

Based on the thermodynamic parameters of the system, Marcus Theory states that, to a certain point, the rate of electron transfer increases as the Gibbs free energy becomes more negative or the process becomes more exergonic (Figure 2.11a). The maximum rate of electron transfer occurs when the change in Gibbs free energy is equal to the energy required to reorganize the system once the electron is transferred (Figure 2.11b). After this point is reached, the rate of electron transfer *decreases* as the process becomes more exergonic, putting it in the "Inverted Region" of Marcus Theory,[78] as shown in Figure 2.11c. The slow back-electron-transfer in a DSSC is often described using this inverted

region[79] and the electron transfer rate coefficient can be solved from the systems' thermodynamic parameters.[78,80]

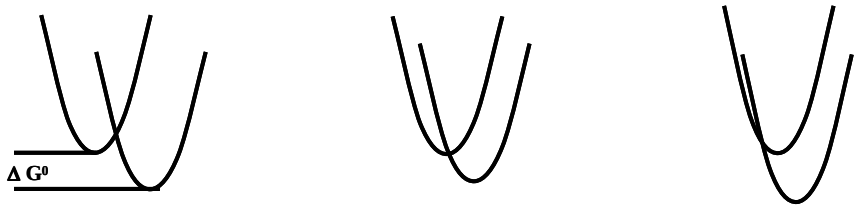

Normal: an increase of ΔG^0 decreases the rate

Maximum k_{ET}: No activation barrier so maximum rate

Inverted: an increase of ΔG^0 increases the rate

a **b** **c**

Figure 2.11 Marcus Theory explaining the rate of electron transfer in the **a)** Marcus Normal region, **b)** Barrierless region, and **c)** Marcus Inverted region.

2.4.3 Charge Transport and Semiconductors.

Once the charge is separated in a DSSC, the electron is transported in the semiconductor nanostructure and the hole is transported in the electrolyte. Originally diffusion was suggested as the mechanism by which electrons moved to the back contact of a DSSC[81], but this has since been modified. Charge transport within an intrinsic semiconductor is predicted to be difficult due to charging. Brus and coworkers found that the electrolyte ions effectively screen the injected electrons present in the semiconducting film which decreases the electrostatic charge (buildup of electrons) and implies that the injected electrons will remain close to the surface of the particle, rather than migrate into the high dielectric constant center.[12,82] Based, in part, that the injected electrons are

located at the film surface, the current model for electron transport describes the semiconductor film as a network of individual particles through which the electrons percolate, hopping from one particle to another.[14,23,83] Grain surface barriers are negligible due to the small size of the nanoparticles. Electron transport is achieved through the trapping and detrapping of electrons at different energy depths on the nanoparticle surface, leading to a distribution of transport times.[14] The path of traps visited by electrons is dependent on the incident light intensity where low light leads to deep trap participation and slow transport times while intense light leads to both deep and shallow trap participation with faster transport times.[84] An area requiring more research is the effect of the electrolyte charge on electron transport within the semiconducting film. It is often assumed that the moving electron pairs with a nearby cation in the electrolyte to move as a neutral species. Studies, however, have shown that the cation movement can lag behind that of the electron at rates similar to that of ion diffusion in solutions.[14,85,86] A more complete description of the role that electrolyte ions play in charge transport within the semiconductor is still needed. Finally, once the electrons have moved through the film they reach the back contact where they can be collected due to a small electric potential drop between the nanoparticle film and the contact material.[87]

Although the bulk of DSSCs are fabricated with TiO_2 films,[62,76,80,88-90] research has also been directed towards using films of ZnO[66,68,71,77,91-94] and, to a lesser extent, SnO_2.[95,96] Oxide semiconductors are good candidates for use in photoelectrochemistry due to their low cost, low toxicity and wide band gap energies, which make them transparent and stable against photocorrosion. The relative positions of the conduction

and valence band energies for these materials is favorable for use in DSSCs as they match well with the other cell components.

Titania is the more common semiconductor layer used in DSSCs and is found in the most efficient DSSC created to date.[11] Titania has a band gap of 3.2 eV and is most frequently found in either the anatase or rutile crystal structure. Most DSSCs contain anatase TiO_2 although Frank and coworkers found the use of rutile particles to yield comparable results.[97] At 300 K, TiO_2 has an electron mobility of 4 $cm \cdot V^{-1}s^{-1}$ (anatase) or 0.1 $cm \cdot V^{-1}s^{-1}$ (rutile).[98]

Zinc oxide films have been used as an alternative to TiO_2 in DSSCs, primarily to explore the complexities of substituting the semiconductor film with a different material but also because ZnO has an electron mobility fifty times greater (205 $cm \cdot V^{-1}s^{-1}$ at 300K) than that of anatase TiO_2 which may be beneficial in the electron transport process. Zinc oxide is most commonly found in the wurtzite crystal structure and Table 2.1 details additional selected physical properties of ZnO.

Table 2.1 Physical Properties of ZnO.

Property	**Value**
Density	5.606 g/cm^3 at 300 K
Exciton binding energy	60 meV
Electron mobility	205 $cm^2\ V^{-1}\ s^{-1}$
Hole mobility	180 $cm^2\ V^{-1}\ s^{-1}$
Static dielectric constant	8.47

Index of refraction	2.09 (λ=450 nm)

2.5 Site Heterogeneity and Use of Oxide Colloids.

As discussed previously, the complexity of the nanocrystalline semiconducting film makes it difficult to interpret experimental and computational results regarding the charge transfer kinetics. Dispersions of nanocrystals can provide binding orientations or configurations that are more homogenous, providing fewer variables when examining the interfacial charge transfer between the dye and the nanocrystal. Use of TiO_2 NCs in place of films has been documented.[34,99-107] Sundström and coworkers measured the electron injection from Fluorescein 27 to dispersions of TiO_2 NCs and compared that to the electron injection from Fluorescein 27 to thin films of nanocrystalline TiO_2.[108,109] They found that injection into the films required a multiexponential fit that incorporated at least three time constants from sub-100 fs to 8 ps whereas the injection into the TiO_2 NC dispersion occurred with a distinguishing time constant of 300 fs. Janssen and coworkers examined dispersions of TiO_2 NCs to which solutions of terthiophene-based dyes were added and used time-correlated, single-photon counting luminescence studies to determine a rate constant of charge separation ~1.7 x 10^{11} s^{-1} along with a binding constant of 8.5 x 10^4 M^{-1}.[28] Several papers were published by Hupp and coworkers that explored electrostatically binding various dye molecules to the surface of negatively charged SnO_2 NCs in aqueous solutions.[83,110-112] They determined a binding constant of 2.5 x 10^6 M^{-1} for a $Ru(bpy)_3^{2+}$ dye on 15 nm diameter SnO_2 NCs using a Langmuir isotherm.[111] This value is consistent with the work performed by both Rodgers and coworkers as well as Meisel and coworkers.[113,114] Hupp and coworkers also probed the

back electron transfer kinetics from colloidal SnO_2 to a series of dyes to better understand the thermodynamic driving force effects. Depending on the chosen dye, they were able to see kinetic behavior that was in the Marcus normal region, the Marcus inverted region or experienced barrierless kinetics.[112] Although the binding behavior and electron transfer kinetics using either TiO_2 or SnO_2 NCs has been established, less is known about the analogous studies using ZnO.

There are numerous reports of DSSCs containing ZnO films, some of which include information regarding the electron injection kinetics associated with dye molecules adsorbed to a ZnO film.[24,66,68,69,71,77,91-94,96,115-117] Conversely, there are few reports of direct measurement of the same kinetics in a ZnO NC system dispersed in solution. Castner and coworkers found that Coumarin 343 fluorescence emission was quenched with the addition of ZnO NCs but did not have direct evidence of charge injection, although it was inferred.[35] Adam and Drew investigated the impact that acceptor state density had on the electron transfer from a zinc porphyrin to a ZnO NC and found a single electron transfer time constant of ~300 ps.[118] It is with all this in mind that the research detailed in the following pages was conducted.

Chapter 3: Binding and Static Quenching Behavior of Visible-Light Absorbing Dyes on Monodispersed Zinc Oxide Nanocrystals*

3.1 Introduction.

Several studies have reported the use of ZnO in dye-sensitized solar cells (DSSCs).[66,68,71,77,91-94] A concern with using nanocrystalline films in DSSCs is that the surface heterogeneity of the film impacts the charge transfer dynamics and clear explanations of the processes are difficult to obtain. In an attempt to reduce this impact, a number of researchers have turned to the study of colloidal particle dispersions, especially of TiO_2 and SnO_2.[28,83,102,103,110-114,119-123] The work described in this chapter primarily examines complexation of two different dyes to the surface of ZnO nanocrystals (NCs): 3',4'-dibutyl-2-phenyl-2,2':5',2"-terthiophene-5"-carboxylic acid (**1-CO_2H**) or bis(2,2′-bipyridine)(4,4′-dicarboxy-2,2′-bipyridine)ruthenium(II) bis(hexafluorophosphate) (**2**) (Figure 3.1). In both cases they yielded fully dispersible ensembles in which site heterogeneity was minimized.

* This chapter is adapted from: Rossini, J.E.; Huss, A.S.; Bohnsack, J.N.; Blank, D.A.; Mann, K.R.; Gladfelter, W.L. *J. Phys. Chem. C* **2011**, 115, 11.

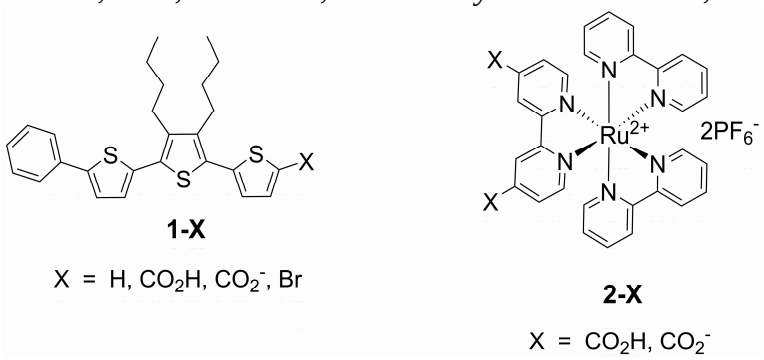

Figure 3.1 Molecular structure of 3',4'-dibutyl-2-phenyl-2,2':5',2''-terthiophene-5''-X **(1-X)** and bis(2,2′-bipyridine)(4,4′-X-2,2′-bipyridine)ruthenium(II) bis(hexafluorophosphate) (**2-X**).

Monodispersed NCs can be prepared by a variety of methods.[124-132] Despite the ease of preparation, only two reports have appeared describing the charge injection kinetics from the excited state of an attached dye molecule into ZnO NCs. Castner and coworkers reported that coumarin 343 is quenched by ZnO nanocrystals but had no direct evidence of a charge injection mechanism.[35] Huss et al. reported that the charge injection rate from the excited state of a zinc porphyrin into ZnO NCs depended on the NC size.[133] In the following pages, the syntheses of well-defined ZnO/dye complexes are described, and their attachment chemistry and quenching behavior probed.

3.2 Experimental Details.

3.2.1 General.

Absolute ethanol, tetramethylammonium hydroxide ($NMe_4OH{\cdot}5H_2O$), zinc acetate ($Zn(CH_3COO)_2{\cdot}2H_2O$), dimethylsulfoxide (DMSO), and ethyl acetate were used

without further purification. 3',4'-Dibutyl-2-phenyl-2,2':5',2''-terthiophene (**1-H**) and 3',4'-dibutyl-2-phenyl-2,2':5',2''-terthiophene-5''-bromide (**1-Br**),[134] **1-CO_2H**,[135] and **2-CO_2H**[21] were prepared as previously reported by members of Kent Mann's research group. Electronic absorption spectra were collected on an Online Instruments Cary-14 conversion spectrometer. The steady-state emission spectra were recorded on a Spex Fluorolog 1680 0.22 m double spectrometer using a xenon source. Fluorescence spectra were corrected to compensate for changes in the instrument's sensitivity at longer wavelengths. All spectroscopy was performed in quartz cuvettes with a 3 mm path length using absolute ethanol unless otherwise noted. The IR spectra of solids (KBr pellet) were recorded on a Nicolet MAGNA-IR 560 spectrometer. Throughout this paper, the number of moles and/or concentration of ZnO NCs refers to the number (or concentration) of discreet NCs in the dispersion.

3.2.2 ZnO Nanocrystal (NC) Synthesis.

The synthesis of ZnO nanocrystals was adapted from Gamelin and coworkers.[130] A 0.55 M ethanolic solution of $NMe_4OH•5H_2O$ (7.73 mL, 4.25 mmol) was dripped into a 0.1 M DMSO solution of $Zn(CH_3COO)_2·2H_2O$ (25 mL, 2.51 mmol) over 30 to 180 s and allowed to stir at room temperature (ca. 24 °C) for 5 - 30 m. The longer reaction times led to larger particles. The diameters were determined using electronic absorption spectra as described in the Results section. To induce precipitation, an aliquot of the solution was removed and added to three times the volume of ethyl acetate. The turbid mixture was centrifuged using a LW Scientific Ultra – 8V centrifuge. After decanting the liquid the

white pellet was added to ethanol to yield an optically clear dispersion of ZnO nanocrystals. Attempts to clean the ZnO NC surface by reprecipitating the NCs and redispersing them in ethanol yielded turbid dispersions that were not useful for the experiments described here.

3.2.3 Quenching of 1-CO_2H Emission by ZnO NCs.

In a typical experiment, a range of 0.01-10.0 mL ZnO NCs (1.22×10^{-11}-1.22×10^{-8} mol) were added to ten vials each containing 3.8×10^{-6} M (4.2×10^{-8} mol) **1-CO_2H** in ethanol. A control vial had the same amount of **1-CO_2H** as the other vials but contained 5 μL 0.100 M $NMe_4OH \cdot 5H_2O$ to deprotonate the molecule. Ethanol was added until all vials contained 11.0 mL. Emission (λ_{ex}=370 nm) and electronic absorption spectra were recorded. All emission intensities were compared to the control sample.

3.2.4 Addition of ZnO NCs to 3',4'-Dibutyl-2-phenyl-2,2':5',2"-terthiophene-5"-bromide (1-Br).

Zinc oxide nanocrystals (5.5×10^{-9} mol) were added to a 2.77×10^{-4} M (2.77×10^{-7} mol) ethanolic solution of **1-Br**. The emission spectrum (λ_{ex}=365 nm) was recorded and compared to the emission of the same concentration of dye without ZnO present.

3.2.5 Adsorption of 1-CO_2H on ZnO NCs.

In a typical experiment, ten vials each containing 2×10^{-9} mol ZnO NCs in ethanol were prepared. To each vial a different amount (0.02-6 mL) of 6.2×10^{-5} M **1-CO_2H** in

EtOH was added. A stock solution (15 mL, 6.2 x 10^{-5} M) of **1-CO_2^-**, prepared by deprotonating **1-CO_2H** with 10 μL of 0.100 M $NMe_4OH \cdot 5H_2O$, was used to prepare ten vials that each had the same quantity of **1-CO_2^-** as was present in the vials containing the ZnO NCs and **1-CO_2H**. Ethanol was added until all vials contained 7.0 mL. The emission spectra (λ_{ex}=370 nm) and electronic absorption spectra were recorded. Emission intensities were compared between vials with and without ZnO present.

3.2.6 Addition of Sodium Acetate to (1-CO_2^-)$_n$ZnO.

A vial containing an ethanol solution of **1-CO_2H** (6.0 mL, 6.24 x 10^{-8} mol) and a dispersion of ZnO NCs (0.5 mL, 1.57 x 10^{-9} mol) was prepared. The NCs were 2.7 nm in diameter. A second vial contained a solution of **1-CO_2^-** (6.5 mL, 6.24 x 10^{-8} mol). Aliquots (5 x 10^{-6} – 4 x 10^{-4} L) of 0.012 M $Na(CH_3COO) \cdot 3H_2O$ were added to each vial. The emission spectra (λ_{ex}=370 nm) and electronic absorption spectra of each sample were recorded following the addition of every aliquot. This procedure was repeated until there were no further spectral changes. The number of moles of acetate adsorbed on the ZnO NCs was calculated from the difference between the amount of unbound (emissive) **1-CO_2^-** present in solution before and after acetate addition. The number of moles of unbound **1-CO_2^-** present in solution was determined from $mol^{total}_{1-CO_2^-}\left(I_{(1-CO_2^-)_n ZnO} / I_{1-CO_2^-}\right)$ where $I_{(1-CO_2^-)_n ZnO}$ and $I_{1-CO_2^-}$ are the emission intensities of the dye/NC dispersion and of a solution having the same concentration of dye without the NCs, respectively. The total number of moles of **1-CO_2^-** present in the mixture is represented by $mol^{total}_{1-CO_2^-}$.

3.2.7 Addition of Zinc Acetate to 1-CO_2^-.

A 9.60 x 10^{-6} M ethanol solution of **1-CO_2^-** was prepared. To this were added aliquots of a 0.012 M solution of zinc acetate in ethanol such that that Zn^{2+} concentration ranged from 9.23 x 10^{-6} to 9.23 x 10^{-4} M. No change in the electronic absorption spectra of the combined solutions were detected, however, the emission maximum increased by 6 nm. The integrated emission intensity decreased by 13%.

3.2.8 Addition of Zinc Acetate to $(1\text{-}CO_2^-)_n$ZnO.

A vial containing an ethanol solution of **1-CO_2H** (6.5 mL, 6.24 x 10^{-8} mol) and a dispersion of ZnO NCs (0.5 mL, 1.57 x 10^{-9} mol) was prepared. The NCs were 2.7 nm in diameter. Aliquots (5 x 10^{-6} – 4 x 10^{-4} L) of 0.012 M $Zn(CH_3COO)_2 \cdot 2H_2O$ were added to each vial. The emission spectra (λ_{ex}=370 nm) and electronic absorption spectra of each sample were recorded following the addition of every aliquot. This procedure was repeated until there were no further spectral changes.

3.2.9 Addition of 2-CO_2H to ZnO NCs with Isolation of $(2\text{-}CO_2^-)_n$ZnO.

Zinc oxide NCs were synthesized as described above but prior to precipitation with ethyl acetate, a 10.0 mL aliquot of the reaction mixture (contained zinc acetate and $NMe_4OH \cdot 5H_2O$ in DMSO/EtOH) was added to 2.0 mg **2-CO_2H** and allowed to stir (ca.

30 min) at room temperature. The **(2-CO_2^-)$_n$**ZnO ensembles were precipitated with 30 mL ethyl acetate, centrifuged and decanted to leave a yellow-orange colored pellet. The pellet (ca. 2.5 x 10^{-8} mol ZnO NCs) was used to make a KBr pellet for IR analysis or was dispersed in ethanol for all other spectroscopy. The concentration of **2-CO_2H** not attached to the ZnO surface was determined quantitatively from the absorbance value of the decanted solution using a molar absorptivity constant of 1.4 x 10^4 $M^{-1}cm^{-1}$ for the dye in ethanol.[136] The concentration of the decanted solution was 7.14 x 10^{-6} M while the starting concentration of **2-CO_2H** was 1.493 x 10^{-5} M.

3.3 Results.

Attachment of **2-CO_2H** on the surface of ZnO nanocrystals was first explored. Confirmation of attachment was determined visually and by FT-IR spectroscopy. Although ZnO films efficiently quench the excited state of **2-CO_2^-**, the ZnO colloid did not. We established that the excited state potential of the dye is too low for electron transfer to the conduction band of the ZnO NCs. Subsequently, **1-CO_2H** was chosen as an alternative dye due to its higher excited state reduction potential. The photoluminescence of **1-CO_2^-** was quenched with the addition of ZnO NCs and a detailed study of both its adsorption onto and quenching by ZnO NCs is discussed in this chapter.

3.3.1 ZnO.

There are a number of syntheses that use zinc acetate to produce dispersions of ZnO nanocrystals.[125,128,130-132] The specific procedure used in this study[130] was chosen

because it was simple, reproducibly formed ZnO NCs of a specific size and generated NCs that were stable in ethanol. It is well known that, due to quantum confinement effects, the onset of electronic absorption shifts to lower energies as the nanocrystals become larger in diameter (Figure 3.2).

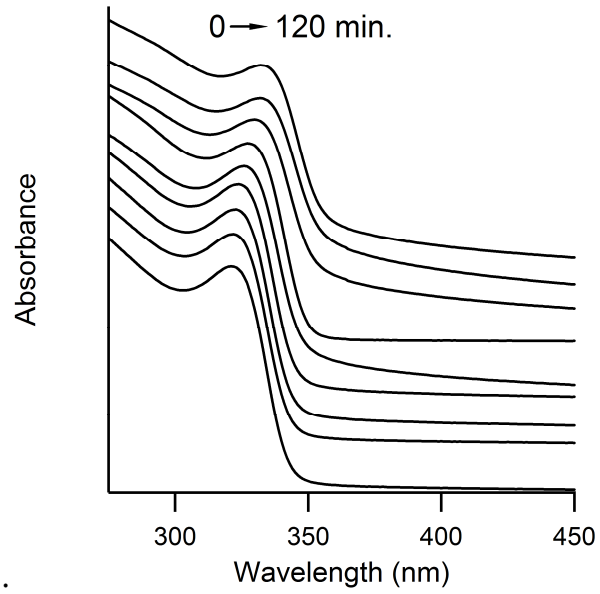

Figure 3.2 Effect of reaction time on electronic absorption spectra of ZnO NC dispersions. Small aliquots of NCs were removed after 0, 3, 5, 10, 20, 45, 60, 90, and 120 minutes, precipitated, dispersed in EtOH and their absorbance recorded. The spectra are vertically offset to show the bathochromic shift as the reaction time increased.

This is consistent with previous experimental[125,130,132,137,138] and theoretical[139-142] studies showing that the band-gap energy is dependent on NC diameter. The diameters of the ZnO NCs were calculated using the absorption spectra wavelengths at the inflection point and a model based on tight-binding theory.[142] Based on previous work, the tight-binding method agreed with XRD and TEM results while the effective mass model overestimated NC diameter.[127] The inflection point was determined by the "differentiate" function in

Igor Pro software. The actual equation used to determine particle diameter from the wavelength at the inflection point is shown in equation 3.1 and was obtained by plotting Sarma and coworkers' data in Microsoft Excel and fitting it with the function of best fit, where ΔE is the difference between the absorption energy at the inflection point (eV) and the bulk band gap energy of ZnO (3.3 eV).

$$\text{ZnO diameter (nm)} = e^{\left(\frac{\ln\left[\frac{\Delta E}{1.7823}\right]}{-1.4925}\right)} \tag{3.1}$$

Using the diameter of the NCs, we determined the number of ZnO units per NC (equation 3.2) and, assuming 100% conversion of Zn^{2+} from zinc acetate to ZnO, calculated the moles of ZnO NCs present for each experiment (equation 3.3).

$$\frac{4}{3}\pi(r)^3\left(1x10^{-21}\frac{cm^3}{nm^3}\right)\left(5.606\frac{g}{cm^3}\right)\left(\frac{1\text{mol ZnO}}{81.4\text{g ZnO}}\right)\left(6.02x10^{23}\frac{\text{ZnO units}}{\text{NC ZnO}}\right) \tag{3.2}$$

$$\text{g } Zn(CH_3CO_2)_2\cdot 2H_2O\left(\frac{1\,\text{mol } Zn(CH_3CO_2)_2\cdot 2H_2O}{219.5\text{g } Zn(CH_3CO_2)_2\cdot 2H_2O}\right) \text{ x } \left(\frac{1\text{mol ZnO}}{1\text{mol } Zn(CH_3CO_2)_2\cdot 2H_2O}\right)\left(\frac{1\text{mol NC}}{\text{X units ZnO}}\right) \tag{3.3}$$

The emission spectra (Figure 3.3) of the ZnO NCs displayed the characteristic green emission (λ_{max} ~530 nm) most often attributed to surface oxygen vacancies and a weak emission (λ_{max} ~350 nm) due to the band gap transition.[137,143,144]

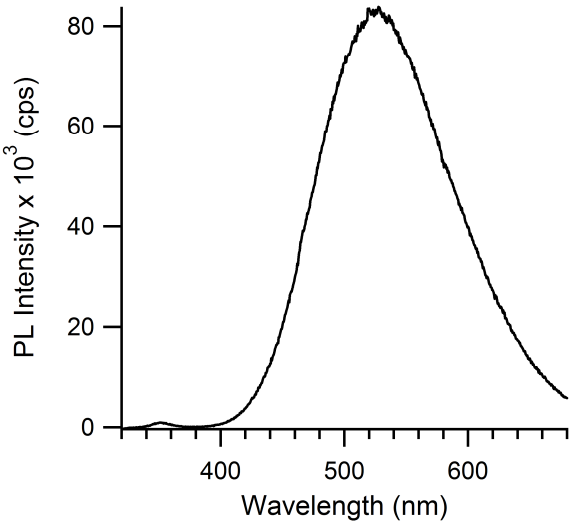

Figure 3.3 Emission from ZnO dispersion in EtOH (λ_{ex} = 290 nm). Approximate ZnO diameter was 3.25 nm.

3.3.2 Characterization of $(2\text{-}CO_2^-)_n$ZnO.

The initial evidence for attachment of **2-CO_2H** to the dispersed NCs was the centrifuged, orange pellet obtained from the precipitation of the reaction mixture containing zinc acetate, $NMe_4OH{\cdot}5H_2O$ and **2-CO_2H** in DMSO/EtOH by ethyl acetate. Because ZnO NCs form a white pellet when centrifuged and **2-CO_2H** is soluble in ethyl acetate, formation of the orange pellet suggested binding. Additional support for binding was obtained through FT-IR analysis. The orange pellet was added to dry KBr and attachment was verified by comparison of the spectra of **2-CO_2H** before and after binding to ZnO NCs (Figure 3.4). The bands at 1605, 1467 and 1447 cm^{-1} for the **2-CO_2H** were attributed to C=C aromatic stretches. A carbonyl asymmetric stretch was assigned to the band at 1734 cm^{-1} for the **2-CO_2H** but disappeared when ZnO NCs were

added. Meanwhile, broad bands appeared in the 1680-1530 cm^{-1} region. These bands were observed in binding a similar dye to ZnO films and were assigned as a carboxylate asymmetric stretch associated with bidentate binding.[24] Also observed upon addition of ZnO NCs was the disappearance of both the PF_6^- band at 840 cm^{-1} and the broad region from ~1288-1152 cm^{-1}. Disappearance of the PF_6^- band was indicative of the overall dye charge becoming neutral in the presence of ZnO. If both carboxylic acid groups were deprotonated on binding to the ZnO, the dye molecule would become neutral and the PF_6^- counter-anion would no longer be required for charge-balance purposes.

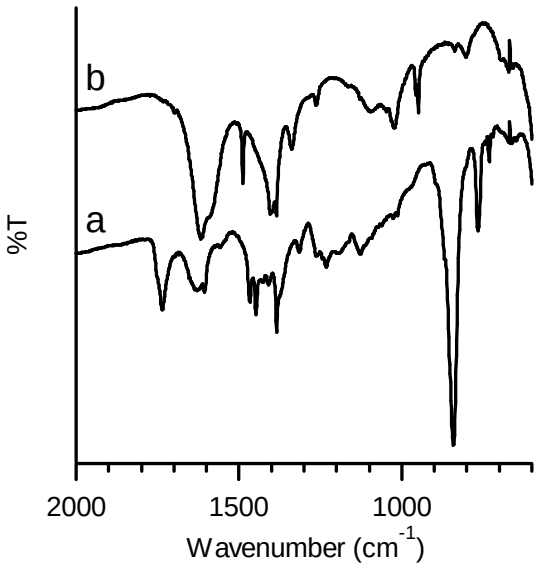

Figure 3.4 FT-IR spectra of a) **2-CO_2H** and b) **(2-CO_2^-)**$_n$ZnO in KBr pellets.

3.3.3 Quantifying $(2\text{-}CO_2^-)_n$ZnO.

The amount of **2-CO_2^-** adsorbed to the ZnO NCs in **$(2\text{-}CO_2^-)_n$**ZnO ensembles was quantified from electronic absorption spectroscopy (Figure 3.5). The absorbance of the decanted solution obtained after precipitating and centrifuging **$(2\text{-}CO_2^-)_n$**ZnO was analyzed at 454 nm, the MLCT region of the dye, and compared to the absorbance intensity of the original concentration of **2-CO_2H**.

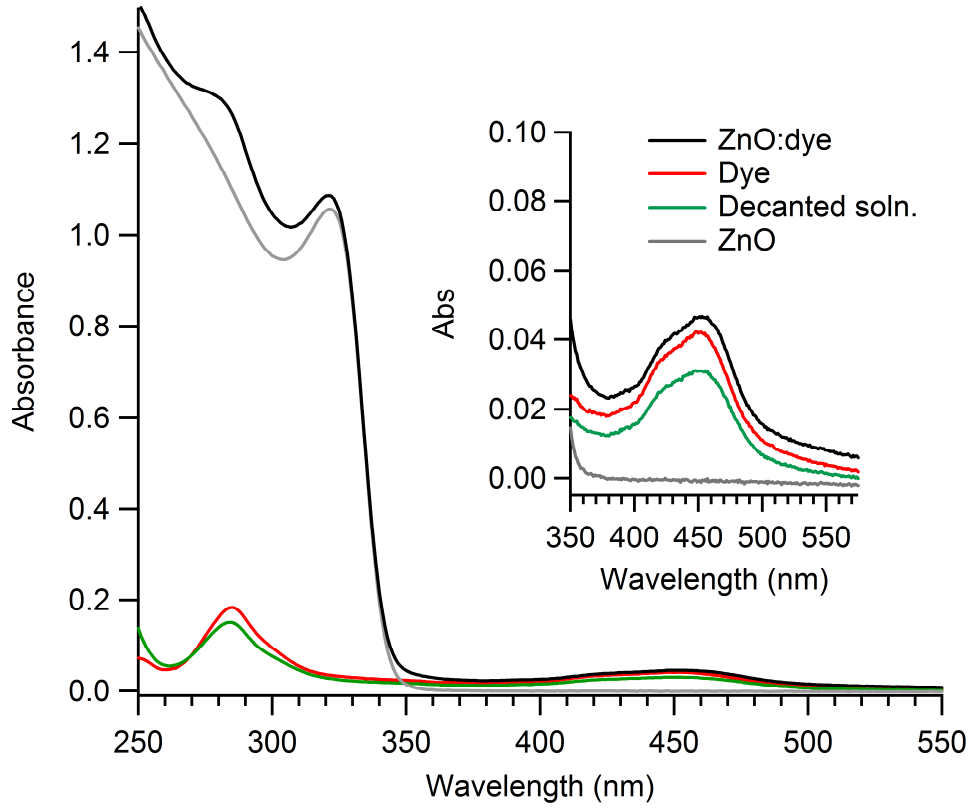

Figure 3.5 Electronic absorption of **2-CO_2H** (red), **$(2\text{-}CO_2^-)_n$**ZnO (black), ZnO NCs (gray) and the remaining **2-CO_2H** that did not bind to the ZnO (green).

The concentration of the decanted solution was 7.14 x 10^{-6} M while the starting concentration of dye was 1.49 x 10^{-5} M. Because separation between bound and unbound dye was achieved, any dye remaining in the decanted solution was considered unbound. This value was subtracted from the value of the original amount of **2-CO_2H** to calculate the moles of dye adsorbed to the ZnO surface. In a typical experiment, an average of 1-2 dye molecules were adsorbed to the surface of the ZnO nanocrystals. Equation 3.4 describes the equilibrium expression for the ensemble.

$$K_{eq} = \frac{[ZnO : Ru(bpy)_2(dcbpy)]}{[ZnO][Ru(bpy)_2(dcbpy)^{2+}]} \quad (3.4)$$

3.3.4 Reaction of 2-CO_2H with ZnO NCs.

Steady-state emission spectra (λ_{ex}=454 nm) were used to observe possible charge transfer events between **2-CO_2H** and the ZnO NCs, as seen in the literature for ZnO films.[14,24,94,145,146] However, the emission of **2-CO_2^-** was not quenched by the addition of ZnO NCs in this study. Instead, emission intensity from the **2-CO_2^-** remained relatively the same or even increased slightly when ZnO NCs were added. The excited-state reduction potential for **1-CO_2H** in acetonitrile is -0.73 eV vs NHE.[70] We concluded that for the size NCs used in these experiments, the rate of radiative decay for **2-CO_2^-** was competitive with the rate of electron injection and so although the thermodynamics of the ensemble were favorable, the kinetics were not.

3.3.5 Reaction of 1-CO_2H with ZnO NCs.

As described in the literature, we expected that **1-CO_2H** would bind to the ZnO NC through a deprotonated carboxylic acid. Infrared spectroscopy shows that upon binding to the ZnO NC, the strong carboxylic acid stretch of **1-CO_2H** at 1671 cm^{-1} disappears (Figure 3.6). The vibrations at 949, 957 and 1488 cm^{-1} in the **(1-CO_2^-)**$_n$ZnO spectrum are due to $N(CH_3)_4^+$ remaining from the ZnO synthesis.

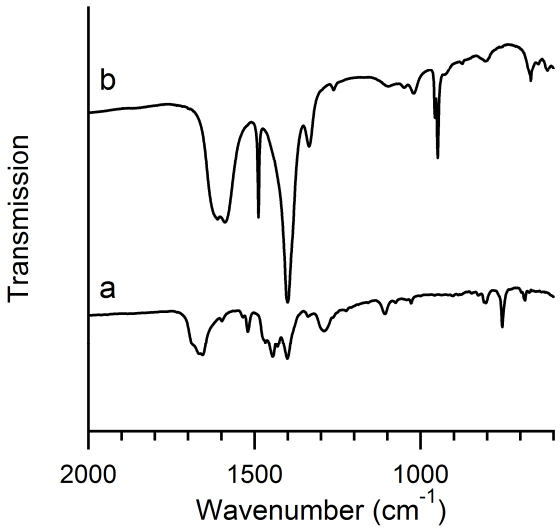

Figure 3.6 FT-IR spectra of a) **1-CO_2H** and b) **(1-CO_2^-)**$_n$ZnO in KBr pellets.

The emission of ethanol solutions containing **1-CO_2H** (λ_{max} = 493 nm) was quenched with the addition of ZnO NCs (Figure 3.7). To probe the importance of the anchoring group, ZnO NCs were also added to a solution of **1-Br** (Figure 3.8). Replacing the -CO_2H substituent with bromide was expected to impair binding to NCs. The

observation of no change in **1-Br** emission when ZnO NCs were added to the solution suggests a static quenching mechanism for **1-CO_2^-**. For all quantitative comparisons outlined in the rest of this chapter, the emission of dye in the presence of ZnO was always compared to the emission of **1-CO_2^-** (deprotonated by NMe_4OH) rather than **1-CO_2H**, because all spectroscopic evidence confirms that both bound and free dye in solution are present as the anion.

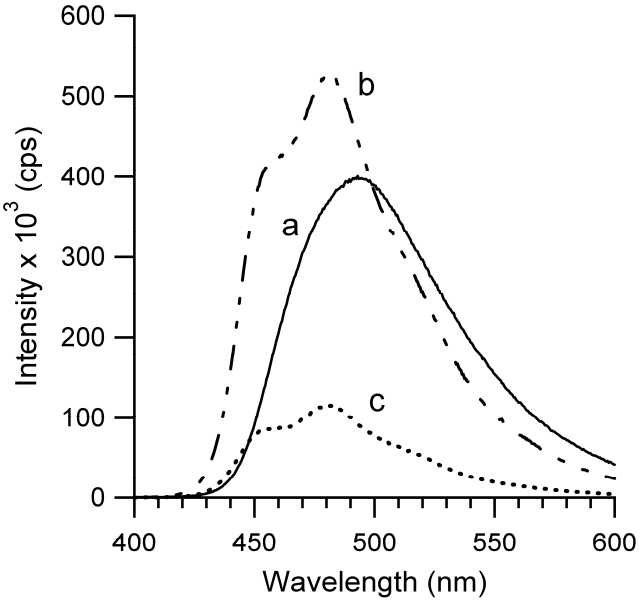

Figure 3.7 Emission of a) **1-CO_2H** b) **1-CO_2^-** and c) **(1-CO_2^-)$_n$**ZnO (λ_{ex} = 450 nm) in ethanol. The concentrations of **1-CO_2H** or **1-CO_2^-** for spectra a-c were 4.16 x 10^{-5} M and the concentration of ZnO NCs present in spectrum c was 2.00 x 10^{-6} M.

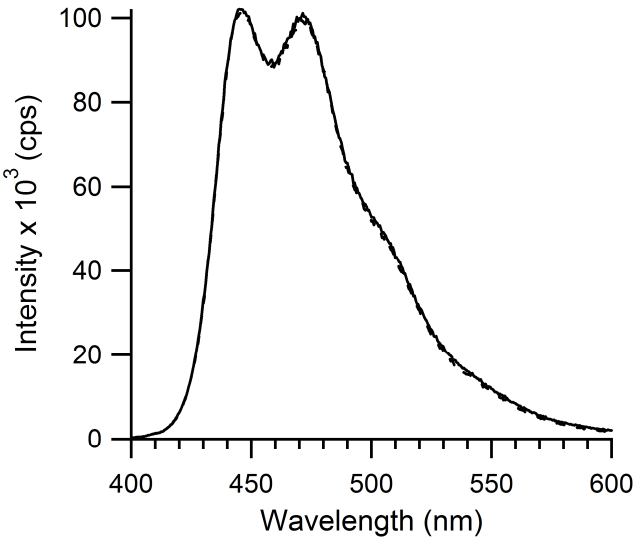

Figure 3.8 Emission of **1-Br** (dashed line) and emission of **(1-Br)** with ZnO NCs present (solid line) in ethanol (λ_{ex} = 465 nm).

3.3.6 Adsorption Isotherms.

Binding of **1-CO_2H** to ZnO NCs was examined as a function of NC diameter and dye concentration. Employing the assumption that all dye molecules bound to ZnO NCs were quenched allows the concentration of bound and unbound dye to be determined at equilibrium. The experimental values of number of moles of dye bound to the NCs (mol_{ads}) were determined using the expression $mol^{total}_{1-CO_2^-}\left(1-(I_{(1-CO_2^-)_n ZnO}/I_{1-CO_2^-})\right)$ where $I_{(1-CO_2^-)_n ZnO}$ and $I_{1-CO_2^-}$ are the emission intensities of the dye/NC dispersion and of a solution having the same concentration of dye without the NCs, respectively. The total number of moles of **1-CO_2^-** present in the mixture is represented by $mol^{total}_{1-CO_2^-}$. To correct for varying concentrations of ZnO NCs used in separate experiments, the moles of adsorbed dye were divided by the moles of ZnO NCs. The results are shown in Figure

3.9. The results were fit to a Langmuir isotherm (eq. 3.5) and optimized using a non-linear least-squares method. The isotherm describes the amount of dye molecules on the ZnO NC as a function of the equilibrium concentration of **1-CO_2^-** at a constant temperature.

$$mol_{ads} = mol_{ads}^{\max} \bullet \frac{K_{ads} \bullet [\mathbf{1\text{-}CO_2^-}]_{eq}}{1 + K_{ads} \bullet [\mathbf{1\text{-}CO_2^-}]_{eq}} \tag{3.5}$$

The analysis yields the maximum amount of dye that can be adsorbed to the ZnO nanocrystal surface ($mol_{ads}^{\max}$) as well as a dye-ZnO adsorption constant (K_{ads}) (Table 3.1). The maximum amount of dye correlates with NC surface area. The K_{ads} for the three experiments yielded an average Langmuir adsorption constant of K_{ads} = 1.5 ± 0.2 x 10^5 M^{-1}.

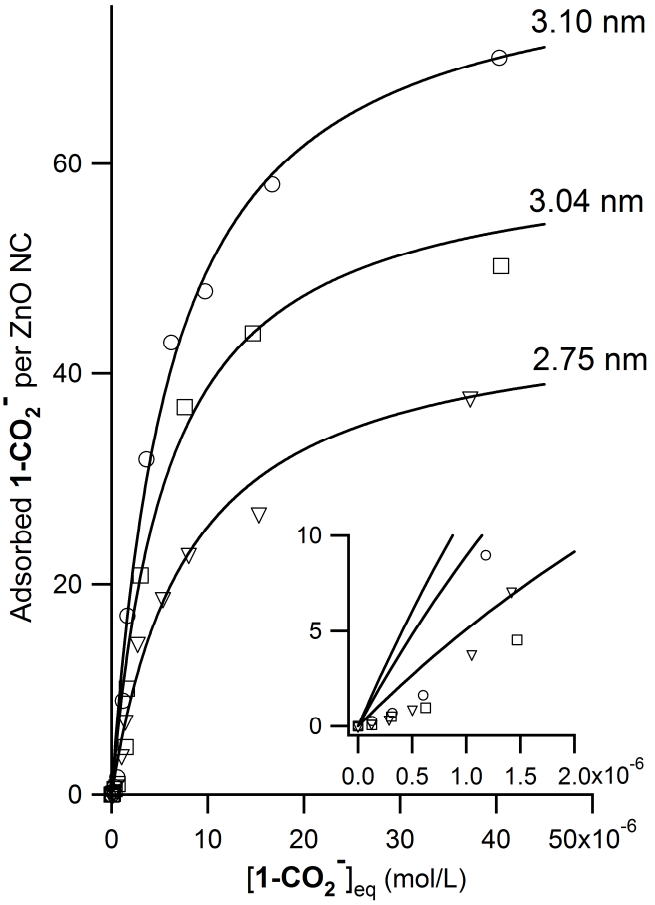

Figure 3.9 Adsorption isotherms of **1-CO_2H** on ZnO NCs (data points) fit with a Langmuir equation (eq. 3.5) (solid line) for samples containing different diameters of ZnO. The experimental points are based on emission measurements as described in the Results section.

Table 3.1 Adsorption Isotherms for **1-CO_2^-** on ZnO NCs.

Model	ZnO dia. (nm)	K_{ads} (M^{-1})	K_2 (M^{-1})	Zn^{2+}/NC	sites/NC (mol_{ads}^{max})
Langmuir (eq. 3.5)	2.8	1.24×10^5	-	-	46
Eqs. 3.7 – 3.11		1.37×10^5	1.37×10^7	1.2	45
Langmuir (eq. 3.5)	3.0	1.70×10^5	-	-	61
Eqs. 3.7 – 3.11		3.27×10^5	1.67×10^7	3.9	54
Langmuir (eq. 3.5)	3.1	1.24×10^5	-	-	81
Eqs. 3.7 – 3.11		2.29×10^5	1.69×10^7	5.4	78

Inspection of Figure 3.9 in the low dye concentration region (see inset) reveals a systematic deviation of the data from ideal behavior. Despite having access to all sites on the NCs, the added dye is not quenched. The extent of this low concentration regime was estimated by determining the interception with the abscissa based on the measurements for dye concentrations between 0.5 - 2 x 10^{-6} M. When the intercepts are divided by the concentration of NCs the ratios are 1.9, 4.7 and 5.2, respectively for the 2.8, 3.0 and 3.1 nm NC dispersions. The ratios increase monotonically with NC surface area. As discussed in greater detail below we assign this behavior to the presence of small quantities of free or loosely bound Zn^{2+} on the surface of the NCs that compete with the NC for complexation of the dye. Providing the Zn^{2+} binds the dye more strongly than does the NC, the observed behavior is expected. This hypothesis requires that Zn^{2+} itself does not quench the emission of the dye. As determined in separate experiments, addition

of **1-CO_2H** to an ethanol solution of zinc acetate does not result in quenching of the emission.

The fit shown in Figure 3.10 used to capture the deviation is based on the model described below in which small concentrations of free Zn^{2+} compete with the ZnO NCs for complexing **1-CO_2^-**.

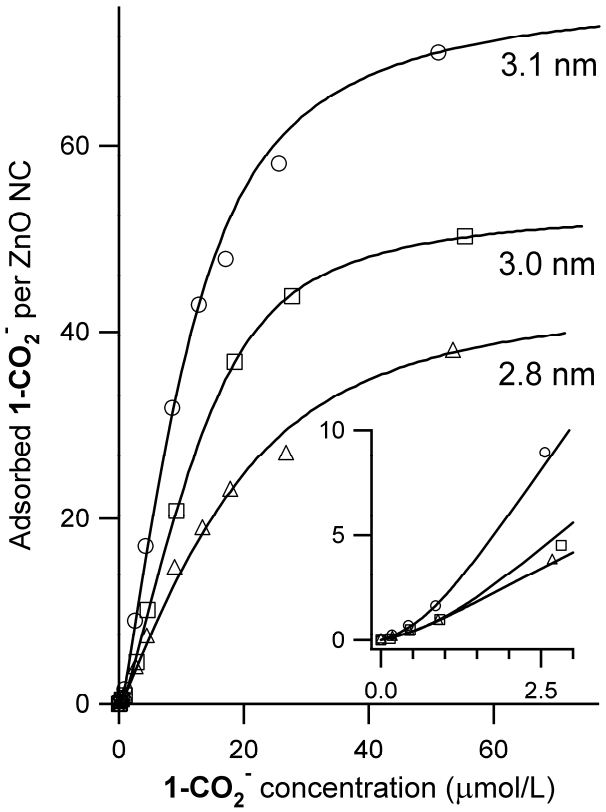

Figure 3.10 Adsorption isotherms of **1-CO_2H** on ZnO NCs (data points) fit with equations 3.7 – 3.11 (solid line) for samples containing different diameters of ZnO. The experimental points are based on emission measurements as described in the Results section.

3.3.7 Stern-Volmer Behavior of 1-CO_2H and ZnO NCs.

Stern-Volmer plots (Figure 3.11) were generated for ZnO NCs having diameters of 2.8, 3.0 and 3.1 nm. The plot of I_0/I shows an initial linear region at low quencher (ZnO NC) concentration, consistent with the Stern-Volmer equation (eq. 3.6) for static quenching.

$$\frac{I_0}{I} = 1 + K_{ads}[ZnO] \tag{3.6}$$

As the ratio of dye to ZnO decreases to approximately 20, however, further addition of ZnO NCs causes a reduction in quenching efficiency. At the highest quencher concentration studied, where the ratio of dyes to NCs approaches one, the value of I_0/I levels off.

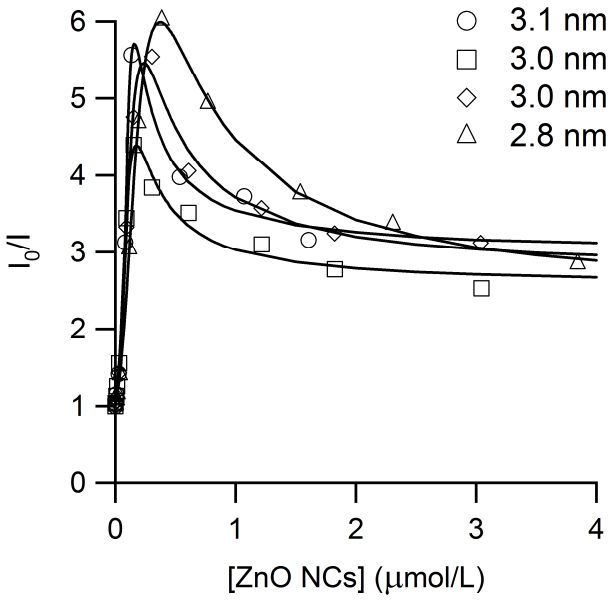

Figure 3.11 Stern-Volmer plot of **1-CO_2H** quenched by ZnO NCs (data points) fit with equations 3.7-3.11 (solid line).

3.3.8 Modeling the Adsorption Isotherm and Stern-Volmer Behavior.

One possibility for the unusual behavior observed at low dye:ZnO ratios is competitive binding to free Zn^{2+}. In order to test this hypothesis we considered the following series of equilibrium and mass balance expressions (eqs. 3.7-3.11),

$$K_{ads} = \frac{\left[\mathbf{1}-\mathbf{CO_2^-}\right]_{ZnO}}{\left[\mathbf{1}-\mathbf{CO_2^-}\right]_{eq} \bullet ZnO_{open}} \tag{3.7}$$

$$K_2 = \frac{\left[\mathbf{1}-\mathbf{CO_2^-}\right]_{Zn^{2+}}}{\left[\mathbf{1}-\mathbf{CO_2^-}\right]_{eq} \bullet Zn^{2+}_{open}} \tag{3.8}$$

$$\left[\mathbf{1}-\mathbf{CO_2^-}\right]_{initial} = \left[\mathbf{1}-\mathbf{CO_2^-}\right]_{eq} + \left[\mathbf{1}-\mathbf{CO_2^-}\right]_{ZnO} + \left[\mathbf{1}-\mathbf{CO_2^-}\right]_{Zn^{2+}} \tag{3.9}$$

$$ZnO_{sites} = sites/NC \bullet ZnO_{NC} = \left[\mathbf{1}-\mathbf{CO_2^-}\right]_{ZnO} + ZnO_{open} \tag{3.10}$$

$$Zn^{2+}_{sites} = Zn^{2+}/NC \bullet ZnO_{NC} = \left[\mathbf{1}-\mathbf{CO_2^-}\right]_{Zn^{2+}} + Zn^{2+}_{open} \tag{3.11}$$

where K_{ads} and K_2 represent the relationship between the amount of dye bound to a site ($\left[\mathbf{1}-\mathbf{CO_2^-}\right]_{ZnO}$ or $\left[\mathbf{1}-\mathbf{CO_2^-}\right]_{Zn^{2+}}$), the amount of unbound sites (ZnO_{open} and Zn^{2+}_{open}) and the concentration of free dye $\left[\mathbf{1}-\mathbf{CO_2^-}\right]_{eq}$ in solution at equilibrium. They are analogous to the Langmuir adsorption constants for dye binding to a ZnO or Zn^{2+} site, respectively. The concentration of dye $\left[\mathbf{1}-\mathbf{CO_2^-}\right]_{initial}$ and number of ZnO nanocrystals (ZnO_{NC}) added to the system were known. It was assumed that there was a constant amount of Zn^{2+}

added with each ZnO nanocrystal addition and that only one dye could bind to a ZnO site or Zn^{2+} ion. Zn^{2+}/NC represents the amount of Zn^{2+} present for each ZnO NC, and *sites/NC* represents the number of binding sites available for each nanocrystal.

This series of equations was solved using the Matlab software package to determine the amount of dye bound to ZnO as a function of added dye or ZnO, for isotherm and Stern-Volmer data sets, respectively. Assuming that only dyes bound to a ZnO site were non-emissive we could then fit our isotherm and Stern-Volmer data sets by using K_{ads}, K_2, *Sites/NC*, and Zn^{2+}/NC as fitting parameters. The assumptions implicit in the model will be discussed below. Figures 3.10 and 3.11 show the results of this fitting procedure. Best fit parameters for isotherm data are shown in Table 3.1 and those for Stern-Volmer data are shown in Table 3.2. For comparison, Table 3.1 also lists values for K_{ads} and *sites/NC* obtained using the standard Langmuir isotherm model (with no consideration of the possible presence of Zn^{2+}). The model based on eqs. 3.7 – 3.11 increases the value of K_{ads} slightly but has little impact on $mol_{ads}^{\max}$. The values of Zn^{2+}/NC from the fits agree well with the estimates based on the intercepts noted earlier.

The hypothesis that a finite amount of available Zn^{2+} is introduced to the system with the NCs is consistent with our results. It is also consistent with reports of the reaction of ZnO films with dyes bearing acid anchoring groups, which note the formation of the Zn^{2+} complexes that may subsequently agglomerate.[117,147] The basis for identifying a quantity of available zinc ion, as opposed to simply etching the surface of a NC results from the finite values of Zn^{2+}/NC obtained in the model. It is hard to understand why etching would be limited to a few zinc ions per NC.

Table 3.2 Modeling Results of Stern-Volmer Experiments

ZnO diameter (nm)	K_{ads} (M^{-1})	K_2 (M^{-1})	Zn^{2+}/NC	sites/NC (mol_{ads}^{max})
2.8	1.49×10^6	1.82×10^7	2.3	49
3.0	1.06×10^6	2.54×10^7	1.2	40
3.0	2.42×10^6	2.05×10^7	2.7	35
3.1	7.21×10^6	3.56×10^7	3.8	37

3.3.9 Effect of Sodium Acetate on $(1\text{-}CO_2^-)_n$ZnO.

A dispersion of $\mathbf{(1\text{-}CO_2^-)_n}$ZnO was prepared using 2.7 nm diameter NCs in which the concentration of $\mathbf{1\text{-}CO_2^-}$ was adjusted to yield the maximum degree of quenching (corresponding to a maximum in the Stern-Volmer plot in Figure 3.11). As increasing amounts of sodium acetate were added to this solution, a return of the $\mathbf{1\text{-}CO_2^-}$ emission (Figure 3.12) is observed, suggesting that acetate displaces $\mathbf{1\text{-}CO_2^-}$ from the ZnO NC. There were no changes to the absorption spectra following the addition of sodium acetate. Calculation of the adsorbed acetate is described in the experimental section.

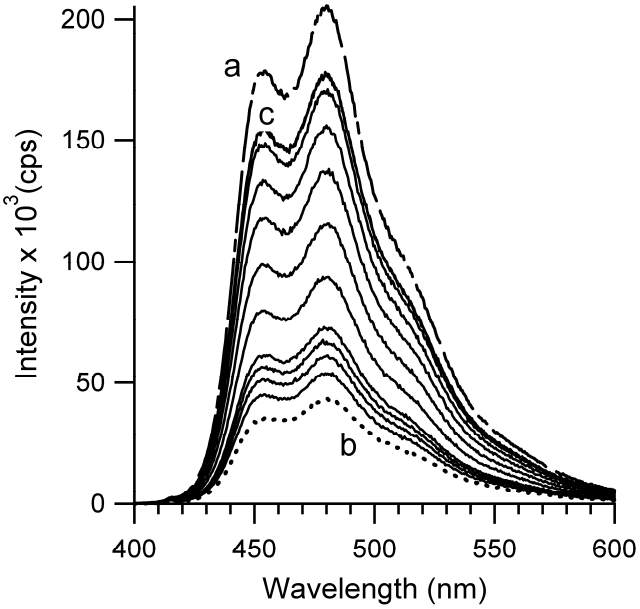

Figure 3.12 Emission from ethanol solutions of pure **1-CO_2^-** (a), **(1-CO_2^-)**$_n$ZnO dispersions at maximum quenching (b) and subsequent additions of sodium acetate to (b) up to 1.8 x 10^{-5} mol (c) (λ_{ex} = 370 nm).

A graph of the data is shown in Figure 3.13 along with a fit based on a competitive Langmuir adsorption (eq. 3.12). Assuming that each adsorbed acetate displaces one **1-CO_2^-** and that the value of the dye adsorption constant (K_{ads}) was unchanged from the results determined for dye binding alone, the variables used to fit the data were the acetate binding constant (K_{ads}^{OAc}) and the maximum amount of acetate adsorbed ($mol_{\max}^{OAc}$). No attempt was made to include the small effect that free Zn^{2+} would have had on the result.

$$mol_{ads}^{OAc} = mol_{\max}^{OAc} \bullet \frac{K_{ads}^{OAc} \bullet [\mathbf{O}Ac^-]_{eq}}{1 + K_{ads} \bullet [\mathbf{1-CO_2^-}]_{eq} + K_{ads}^{OAc} \bullet [\mathbf{O}Ac^-]_{eq}} \qquad (3.12)$$

The value of K_{ads}^{OAc} was 6100, consistent with the observation that a ~25 fold excess of sodium acetate was needed to displace half of the adsorbed **1-CO_2^-**. The value of $mol_{\max}^{OAc}$ was 6.2 x 10^{-8} mol, which corresponds to 40 acetate ions per NC. This agrees with the value (Table 3.1) of 46 sites/NC of adsorbed dye for a slightly larger NC (2.8 nm).

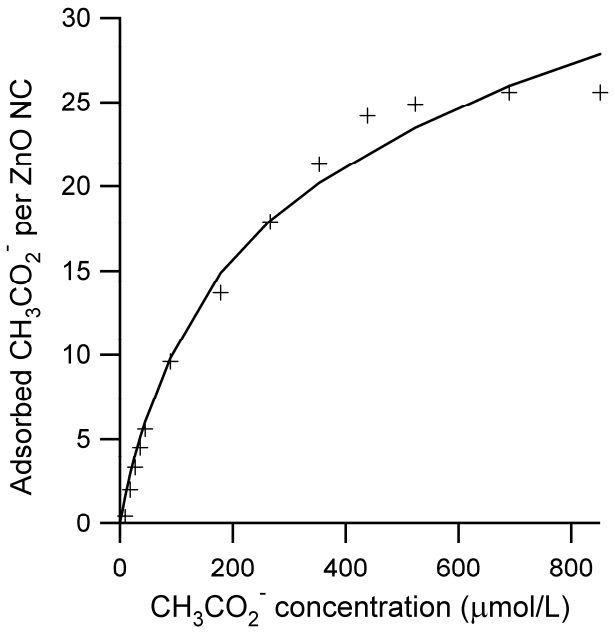

Figure 3.13 Substitution by acetate of **1-CO_2^-** from **(1-CO_2^-)**$_n$ZnO fit with eq. 3.12. The NC diameter was 2.7 nm. The determination of the amount of adsorbed acetate is based on the emission intensity of **1-CO_2^-** as described in the experimental section.

3.3.10 Effect of Zinc Acetate on 1-CO_2^-.

A solution of **1-CO_2^-** was prepared with the same concentration used in the previous sodium acetate experiment. As increasing amounts of zinc acetate were added to this solution, the integrated emission intensity decreased by 13%, the emission

wavelength increased 6 nm, and a change in the spectral shape was observed (Figure 3.14). The change in spectral shape and red-shift in energy suggests complexation of Zn^{2+} to **1-CO_2^-**. There were no changes to the absorption spectra following the addition of zinc acetate.

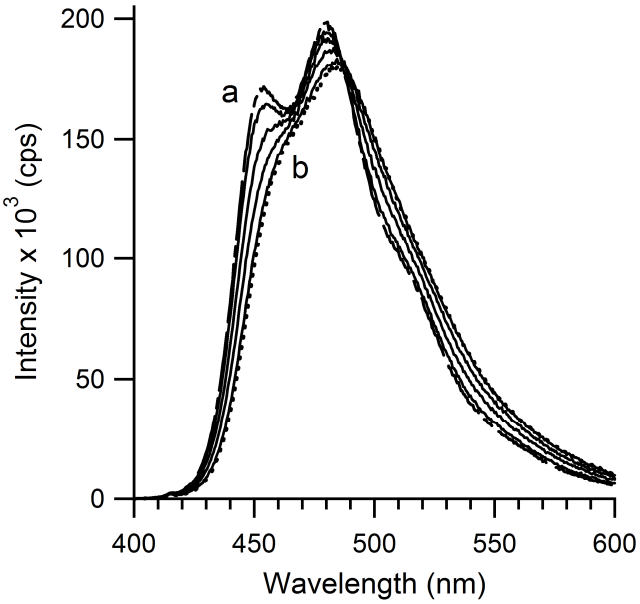

Figure 3.14 Emission from ethanol solutions of pure **1-CO_2^-** (a) and subsequent additions of zinc acetate to (a) until 1.8 x 10^{-5} moles of zinc acetate were added (b) (λ_{ex} = 370 nm).

3.3.11 Effect of Zinc Acetate on (1-CO_2^-)$_n$ZnO.

A dispersion of **(1-CO_2^-)$_n$**ZnO was prepared using 2.7 nm diameter NCs in which the concentration of **1-CO_2^-** was adjusted to yield the maximum degree of quenching (corresponding to a maximum in the Stern-Volmer plot in Figure 3.11). As increasing amounts of zinc acetate were added to this solution (Figure 3.15), a return of the **1-CO_2^-** emission was observed along with a change in spectral shape. The increase in emission intensity suggests that acetate displaces **1-CO_2^-** from the ZnO NC surface as seen in the

previously described sodium acetate experiment. The change in spectral shape suggests complexation of Zn^{2+} to **1-CO_2^-** as observed when zinc acetate was added to a solution of **1-CO_2^-**. There were no changes to the absorption spectra following the addition of zinc acetate to **(1-CO_2^-)**$_n$ZnO.

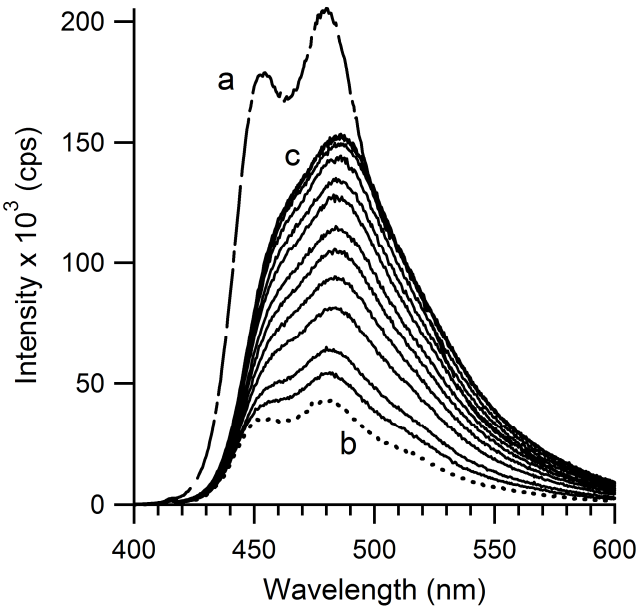

Figure 3.15 Emission from ethanol solutions of pure **1-CO_2^-** (a), **(1-CO_2^-)**$_n$ZnO dispersions at maximum quenching (b) and subsequent additions of zinc acetate to (b) up to 1.8 x 10^{-5} mol (c) (λ_{ex} = 370 nm).

3.4 Discussion

The adsorption of dyes on nanoparticle films of TiO_2, ZnO or related metal oxides forms the basis of dye-sensitized solar cell technology.[16,80,93] The adsorption process involves treating the nanoparticle film with a solution containing the dye. After removal of the substrate from the solution, unbound dye is removed by washing with fresh

solvent. After drying the dye-sensitized film is ready for further study or device construction. Studies involving dye adsorption on nanocrystals dispersed in solvent must establish that the dye is indeed bound to the particles, or more specifically, measure the fraction of adsorbed dye. From this research we were able to better understand how many and by what mechanism dye molecules bind to the surface of ZnO NCs. The use of two dyes with different excited-state reduction potentials allowed for a more specific determination of the location of the conduction band energy of the ZnO NCs. Obtained quenching constants and adsorption constants add to the breadth of knowledge regarding ZnO NC surfaces as well as interactions between ZnO surfaces and dyes containing carboxylic acid linking groups.

3.4.1 Adsorption of 2-CO_2^- on ZnO Nanocrystals.

The nature of the binding between the **2-CO_2H** and ZnO NCs was well defined through FT-IR analysis. Carboxylic acids form bonds with semiconductor surfaces primarily through bidentate carboxylate bonds[26,27,146,148] and the adsorption of polypyridyl-ruthenium molecules to ZnO nanocrystalline films is documented.[24,92,94,149] As stated in Section 3.3.5, the disappearance of the carboxylic acid group region from 1735-1530 cm^{-1} with the addition of ZnO NCs revealed that the protonated form (**2-CO_2H)** was no longer present but was rather converted to **2-CO_2^-** when it attached to the NC surface. That there was absolutely no signal in this area suggests that all carboxylic acid groups were completely transformed into carboxylate groups indicating that bidentate binding of both linking groups to the nanocrystal surface was the primary mode

of attachment. Also observed was that the PF_6^- counter anion had fully disappeared and again supported the conclusion that bidentate binding occurred from two carboxylate groups as it was no longer required to balance the +2 charge on the metal center.

Although the emission of the **2-CO_2H** was not quenched with addition of ZnO, it allowed us to more precisely define the conduction band energy of the ZnO NCs. The excited state reduction potential for **2-CO_2H** is -0.73 eV (vs. NHE in acetonitrile)[70] while the conduction band energy for a 2.5 nm diameter ZnO nanocrystal was semi-empirically calculated to be -0.6 eV (vs. NHE) which is approximately 0.4 eV more negative than bulk ZnO. Due to the energetically favorable conditions for electron transfer from the dye to the semiconductor by 0.13 eV, one would predict charge injection to occur. However, no quenching was observed and is indicative of an uphill process. The fact that the excited state of **2-CO_2H** is quenched when adsorbed on continuous ZnO films and on large (30 nm) particles suggests that quantum confinement plays an important role in the smaller particles.

In response, **1-CO_2H** was selected, in part, for its higher excited state reduction potential energy of -1.61 eV (vs. NHE in acetonitrile). As discussed previously, the emission of **1-CO_2H** was quenched with ZnO NC addition and supported our conclusion that the rate of electron injection of **2-CO_2H** into ZnO was too comparable to the rate of radiative decay of the dye for quenching to occur.

3.4.2 Adsorption of 1-CO_2^- on ZnO Nanocrystals.

The excited state of the phenylterthiophene carboxylic acid derivative, **1-CO_2H**, shown in Figure 3.7 is quenched by small ZnO particles. Using a combination of absorption and fluorescence measurements, we determined the amount of **1-CO_2H** adsorbed on ZnO NCs in ethanol. We assumed that the excited states of adsorbed dyes were quenched. This is consistent with observation of complete quenching of dyes by ZnO films.[24,69,96,117] Despite the many assumptions implicit in the Langmuir model for describing the adsorption isotherm, Figure 3.9 shows reasonable fits. In these experiments we maintained a constant concentration of NCs, thus dispersions of the larger particles had a higher surface area and therefore a larger number of available binding sites. Comparing the maximum number of occupied sites to the calculated surface area of the three sizes of NCs suggests that each dye occupies 0.5 ± 0.1 nm^2. From the flattest possible conformation of **1-CO_2H** one would estimate a molecular footprint of 0.4 nm^2. At the other extreme the calculated structure of an isolated molecule gives a footprint of 1.5 nm^2 because in the absence of intermolecular interactions the two n-butyl groups point to different sides of the molecular plane. This suggests that at full coverage the dye molecules are packed closely on the surface and forced into a constricted conformation. The curvature of the particle surface will help to reduce the congestion.

The adsorption experiments involve adding **1-CO_2H** to the NCs. Deprotonation of **1-CO_2H** involves reaction with surface bound acetates or hydroxides. Infrared and emission spectra clearly indicate the dye is bound as the carboxylate, which could form a discreet Zn-O bond or the interaction could be ionic in nature. Our spectroscopic results

cannot differentiate between these bonding modes. The surface area per carboxylate estimated from the above measurements is substantially larger than the surface area of zinc ions on the close-packed $(0001)_{ZnO}$ face (~0.1 nm^2/Zn^{2+}). It is likely that even on crystallographic planes that have a lower Zn^{2+} density, enough zinc sites would be available to accommodate the maximum coverage of dyes.

An additional test was applied that confirmed the importance of the $–CO_2^-$ binding group. Replacement of the $–CO_2H$ functional group with a -Br resulted in little change to excited state potential and spectroscopic properties of the molecule. Fluorescence measurements, however, established the excited state of **1-Br** was not quenched by the presence of ZnO (Figure 3.8). *This comparison emphasizes the static nature of the quenching process and the importance of the $–CO_2^-$ binding group for quenching*. Beek and Janssen used this approach to establish that the excited state of [2,2':5',2"]-terthiophene-5-carboxylic acid was quenched by TiO_2 particles via a static mechanism.[28]

The average adsorption equilibrium constant based on the experiments described above was $2.3 \pm 1.0 \times 10^5$ M^{-1} and did not depend systematically on the NC diameter. Ghanem recently reported an association constant of 6.7×10^4 M^{-1} of a zinc phthalocyanine complex bearing pendant tyrosines with ZnO NCs.[150] Hasnat and coworkers determined $K_{ads} = 1.5 \times 10^5$ M^{-1} for erythrosine molecules attached via carboxylate groups to ZnO particles.[31] For the more thoroughly studied TiO_2 surface Parkinson and coworkers have reported binding constants of 2.8×10^4 and 8.9×10^3 M^{-1}, respectively, for the adsorption of **N3** from ethanol solution onto films and single crystal

(anatase) surfaces.[29,30] Gray and coworkers reported that values of K_{ads} on TiO_2 films for several ruthenium-based dyes bound via carboxylates ranged from 2000 to 3 x 10^5 M^{-1} in ethanol.[26] Beek and Janssen report that terthiophene carboxylic acid binds to TiO_2 NC dispersions in nonpolar solvents with a K_{ads} = 8.5 x 10^4 M^{-1}.[28] Considering the differences in metal oxide substrates and the molecular structures of the dyes, the small range of observed binding constants highlights the dominant role of the carboxylate anchoring group.[25]

3.4.3 Dye Displacement by Acetate.

The ZnO NCs were prepared using zinc acetate, and infrared spectroscopy confirms that some acetate remains bound to the NC surface. Excess acetate ion can be used to displace bound **1-CO_2^-** from the ZnO NC surface. A study of the competitive binding of the two carboxylate ions in ethanol reveals that **1-CO_2^-** binds more strongly to the NC than does acetate by a factor of 25. We find the differences in the binding constants interesting and will probe the causes in future studies.

3.4.4 Stern-Volmer Behavior.

The complicated behavior of ZnO NC quenching of the excited state of **1-CO_2^-** is evident in the Stern-Volmer plot shown in Figure 3.11. Two distinct regimes are observed as a function of ZnO NC quencher concentration. At low ZnO NC concentrations, nearly linear behavior is observed. In this regime the number of molecules outnumber the ZnO NCs. When the dye/NC ratio reaches approximately 20, a

maximum in quenching is reached and at higher NC concentrations a rapid fall off is followed by a slow approach to an I_0/I value greater than 1.

We considered the possibility that the ZnO NCs serve merely to organize many molecules of **1-CO_2^-** into a closely packed surfactant layer, thus promoting concentration quenching.[34] As the surface density of molecules decreases with increasing ZnO NC concentration, concentration quenching would be expected to decrease. We discard this mechanism for two reasons. First, there are no signatures in the absorption spectra of these solutions that change as a function of ZnO NC concentration. Concentration quenching of molecular dyes works through excited state migration to molecules that have an altered electronic structure in which coupling promotes non-radiative relaxation. One expects to see spectroscopic evidence for the fraction of adsorbed molecules having the altered electronic structure. Second, ultrafast spectroscopic measurements of this system, published in the companion paper, establish that quenching occurs at all dye/NC ratios primarily by an electron transfer event.[151]

An alternative explanation of the Stern-Volmer behavior is based on the observation that addition of zinc acetate to a quenched solution of **1-CO_2^-** and ZnO NCs caused a reduction in the amount of quenching. The reaction of zinc acetate with **1-CO_2^-** forms a complex that emits with nearly the same efficiency as uncomplexed **1-CO_2^-**. If the ZnO NCs retained a small amount of free or weakly bound Zn^{2+}, the competition indicated in eqs. 3.7-3.11 would be established. In the case where the concentrations of Zn^{2+} and ZnO far exceed that of **1-CO_2^-**, we would expect the partitioning between the two binding sites to reach a constant value. Those molecules of **1-CO_2^-** bound to Zn^{2+}

would continue to emit, while those bound to ZnO NCs would be silent. This would be consistent with the zero-slope region of the SV plot observed at high quencher concentration.

At low quencher concentration, the large [**1-CO$_2^-$**]/[ZnO] and [**1-CO$_2^-$**]/[Zn^{2+}] values mean that all Zn^{2+} and ZnO sites will be saturated. Because each ZnO NC can bind many dye molecules (the adsorption isotherms establish that a 3 nm NC will bind as many as 60 molecules of **1-CO$_2^-$**) an initially rapid and nearly linear increase in I_o/I is observed. As more quencher is added, unbound **1-CO$_2^-$** is depleted and the ratio of dye molecules bound to ZnO NC vs. Zn^{2+} will decrease to reflect the stronger binding to Zn^{2+}. This leads to the observed reduction in quenching efficiency. The model based on eqs. 3.7-3.11 does an excellent job of capturing the qualitative shape of the Stern-Volmer plots. The quantitative values of the variables used to fit the data are close to those derived from the adsorption isotherm experiments, except for K_{ads} where the values are approximately an order of magnitude higher for the Stern-Volmer experiments. At the present time, we can offer no explanation for this difference. We considered that a systematic increase in the contribution of dynamic vs. static quenching is possible as a function of the increase in ZnO NC concentration. If this were occurring, but not included in the model, the value of K_{ads} would increase to compensate. Ultrafast spectroscopic measurements to be published separately, however, find no change in the lifetime of unbound **1-CO$_2^-$** as a function of ZnO NC concentration.[151] Ultimately, we believe that the best value to use for K_{ads} is $2.3 \pm 1.0 \times 10^5$ M^{-1}, which is based on the Langmuir model and includes the small compensation for the effect due to free Zn^{2+}.

3.5 Conclusions

The terthiophene-based dye, **1-CO_2H**, was found to bind to ZnO NCs as the carboxylate and its excited state was quenched. For a constant concentration of NCs, measurement of the proportion of bound vs. unbound **1-CO_2^-** as a function of dye concentration produced an adsorption isotherm that was fit to a Langmuir model. The value of K_{ads} of 2.3 ± 1.0 x 10^5 M^{-1} did not depend on the size of the NC, but the maximum number of adsorbed dyes per NC increased with increasing NC diameter. At low dye concentrations, observation of a small deviation of the experimental values from the Langmuir model was attributed to a second equilibrium in which a portion of the dye is ligated to free zinc ions. Although linear at lower quencher (ZnO NC) concentrations Stern-Volmer plots exhibited complex behavior, which was also consistent with the presence of free zinc ion in the solutions. Acetate ions were used to displace **1-CO_2^-** from the surface of the NC dyads.

Chapter 4: Photoinitiated Electron Transfer Dynamics of a Terthiophene Carboxylate on Monodispersed Zinc Oxide Nanocrystals*

4.1 Introduction.

First reported by Grätzel and co-workers in 1991, dye-sensitized solar cells (DSSCs) are typically made using nanocrystalline titanium dioxide films and an inorganic bipyridine based sensitizer.[9] Conversion efficiencies have been reported in excess of 10%, suggesting that this technology has the potential to become competitive with standard p-n junction devices in some applications.[116] Zinc oxide has been considered as a potential alternative component in DSSCs due to the similar energetic alignment of the conduction band, higher electron mobility, and flexibility in terms of synthesis and film morphology.[71,152-155] However, DSSCs utilizing ZnO typically show poorer conversion efficiencies and slower dye to nanocrystal electron transfer rates compared to analogous TiO_2 systems.[80,115,116] Several possible reasons for the reduced performance with ZnO have been hypothesized, including problems related to chemical stability of the ZnO and differences in donor/acceptor electronic coupling.[80,91]

* This chapter is adapted from: Huss, A.S.; Rossini, J.E.; Ceckanowicz, D.J.; Bohnsack, J.N.; Mann, K.R.; Gladfelter, W.L.; Blank, D.A. *J. Phys. Chem. C* **2011**, 115, 2.

Electron transfer dynamics are complicated on nanocrystalline surfaces, where the heterogeneous dye environment exhibits multiple injection time scales for a given sensitizer. Reported time constants range from <100 fs to hundreds of picoseconds.[66-72,156,157] Measured injection rates have been found to depend on the preparation conditions of the semiconductor NC films.[63-65]

Investigating the charge transfer in dye:NC solvent dispersions can provide a more homogeneous ensemble of dye:NC binding configurations, thereby allowing a more detailed investigation of interfacial charge transfer and more consistent comparisons between systems. For example, Sundström and coworkers have measured electron injection from Fluorescein 27 to both thin films of TiO_2 and aqueous dispersions.[108,109] It was found that injection to the dispersed TiO_2 occurred with a characteristic time constant of 300 fs, while injection into the films was multiexponential requiring at least three time constants ranging from sub-100 fs to 8 ps. One conclusion from this study was that the injection rates into TiO_2 films are distributed among a variety of bound dye confirmations.

Solution phase colloidal TiO_2/sensitizer mixture studies have been reported for a number of organic and inorganic dye systems,[34,99-107] and ZnO NCs are well suited to analogous studies. There are synthetic routes available to making controlled relatively narrow size distributed ZnO NCs that can be dispersed in both nonpolar and polar solvents.[125,127,131,132,158-160] However, there are comparatively few examples where electron transfer between an attached sensitizer and a well-defined ZnO NC has been measured. The time scale for electron transfer was inferred from fluorescence quenching

of coumarin 343 in a solution of ZnO NCs.[35] Electron injection was found to be almost two orders of magnitude slower than for the same dye mixed in aqueous dispersions of TiO_2 nanocrystallites. The electron transfer rates were recently reported from a bound porphyrin donor using the size of the ZnO NC to shift the density of acceptor states systematically.[118]

In Chapter 3, a new organic sensitizer, 3',4'-dibutyl-2-phenyl-2,2':5',2''-terthiophene-5''-carboxylic acid (**1-CO_2H**) made by members of Kent Mann's group was described and static emission quenching in dispersions with ZnO NCs was demonstrated. In addition to being good light absorbers and hole conductors,[33,57,161-170] terthiophenes offer the ability to tune their electronic properties via synthetic substitution.[51,54,163,171,172] For studies of excited state charge transfer they also possess discernible spectroscopic signatures for the excited singlet, triplet, and reduced forms. In this chapter, Adam Huss and I investigated the electron transfer dynamics of **(1-CO_2^-)**$_n$ZnO as a function of the dye:NC ratio using a combination of ultrafast time-resolved fluorescence and frequency-resolved pump-probe spectroscopies. The results demonstrate that charge injection is dominated by a single component with a time constant of ~3.5 ps, which corresponds to a rate that is substantially faster than either intersystem crossing or internal conversion in the dye. A maximum in the static emission quenching was observed at a dye:ZnO NC near 20:1. A similar maximum in the emission quenching was previously observed for analogous TiO_2 systems, where it was concluded that intermolecular interaction between the dye molecules was responsible for enhanced quenching at high surface coverage.[34,173] Here we present direct evidence, probing both the dye excited state and cation, that there

is no measurable change in the excited state dynamics as a function of dye:NC ratio. Fluorescence quenching is shown to be dominated by electron transfer at all ratios, indicating that the enhanced quenching at high coverage is not the result of dye-dye interactions. The results support an alternative explanation for the complex quenching behavior, competitive binding of the dye between the ZnO NCs and free Zn^{2+} cations in solution as discussed in Chapter 3. The overall research described in this chapter involved collaboration with members of Kent Mann's and David Blank's research groups, specifically Adam Huss, who performed all of the spectroscopy detailed below.

4.2 Experimental Details.

4.2.1 General.

Synthesis and characterization of **1-CO_2H** and the ZnO NCs, as well as time integrated emission quenching behavior, are described in detail in the previous chapter. ZnO NC concentrations were estimated assuming full conversion of the starting material, and samples with dye:ZnO NC ratios of 250:1, 50:1, 8:1, 1:1.5, and 1:2 were prepared immediately prior to all experiments. The average ZnO NC diameter was estimated based on the absorption onset.[142] The ZnO NCs used in the experiments originated from three separate synthetic batches. One batch was used for the 250:1, 8:1, and 1:2 ratio samples and had an average diameter of 3.1 nm. A second batch was used for the 50:1 samples, which also had an average diameter of 3.1 nm. The third batch of particles was used for the 1:1.5 sample and had an average diameter of 3.8 nm. The solvent in all cases was ethanol (Parmco-Aaper, 200 proof, ACS/USP grade) and all experiments were conducted

at room temperature. Samples of **1-CO_2H** in solution included the addition of a small amount of tetramethylammonium hydroxide to maintain the deprotonated form of the dye, **1-CO_2^-.**

The dye concentration was ~10^{-4} M in all samples, with an optical density of ~0.1 at the excitation energy of 405.5 nm. We note that the dye:ZnO NC ratios represent the amount of each species that are prepared in solution, and do not directly indicate the actual binding ratios. The binding constant is estimated to be 2.3 x 10^5 M^{-1} from the static quenching studies using a Langmuir isotherm based model, as discussed in Chapter 3. The distribution of bound dye molecules per particle can be described by a Poisson distribution,[102,174-176] however, coverage may depend on additional factors such as competitive binding with any free Zn^{2+} cations present in solution.

4.2.2 Time Integrated Spectra.

Time integrated absorption and emission spectra were recorded using a Cary 14 using the OLIS Globalworks software suite and a Spex Fluorolog 1680 0.2 m double spectrometer using DataMax software, respectively. The fluorescence quantum yield was determined relative to coumarin 153 in two solvents (φ_{fl} = 0.45 in methanol, φ_{fl} = 0.45 in cyclohexane).[177] Coumarin 153 was purchased from Exciton and used as received. Emission spectra were measured in a 1 cm quartz cell using 400 nm excitation. Optical densities were below 0.1 for all measurements.

4.2.3 Spectroelectrochemistry.

Cyclic voltammograms were obtained on a BAS-100B electrochemical analyzer using methods previously described.[178] All solutions were dissolved in acetonitrile with 0.1 M tetrabutylammonium hexafluorophosphate ($TBA^+PF_6^-$) as the supporting electrolyte and degassed with argon. Reported E^0 potentials are referenced to an Ag/AgCl electrode and are uncorrected for junction potentials. The ferrocenium/ferrocene couple was measured, under otherwise identical conditions, to have an E^0 = +0.42 V with $E_{pa} - E_{pc}$ = 110 mV.

Absorption spectroelectrochemical measurements were performed in a specular reflectance thin-layer (0.2 mm) cell using a BAS-100B bulk electrolysis program. Solutions were prepared identical to those in the electrochemistry experiment. Spectra in the UV-vis region were recorded using and Ocean Optics USB4000 spectrometer.

4.2.4 Time-Resolved Measurements.

Time-resolved measurements were taken using a David Blank group, home-built, amplified ultrafast Ti:sapphire laser system, which has been described previously.[179] Briefly, a 200 mW, 85 MHz pulse train is produced by a mode-locked oscillator pumped by 2.7 W from a SW Nd:YVO_4 laser (Spectra Physics, Millenia Pro). Selected pulses are amplified at 1 kHz by a home-built regenerative amplifier pumped with a Q-switched Nd:YAG laser (Spectra Physics, Empower 15). After compression, the 1.53 eV pulses have an energy of approximately 400 μJ and are ~75 fs fwhm assuming a Gaussian profile. All samples were excited at 405.5 nm by frequency doubling the laser fundamental using a 1 mm BBO crystal.

4.2.4a Fluorescence Upconversion.

Fluorescence decays were measured using the Blank group's previously described fluorescence upconversion apparatus.[54,179,180] Sample solutions were flowed at 0.25 mL/s through a 1 mm path length quartz cell. The excitation beam was focused to a spot size of 300-400 μm by a 15 cm lens. Sample emission was gated with a residual 810 nm pulse using sum frequency generation in a BBO crystal. The timing between the gate and excitation pulses was controlled using the translation of a mirror via a computer-controlled delay stage (Newport UMT150PP.1). The resultant signal was frequency selected and detected using a photomultiplier tube (Hamamatsu R36-10). The output of the tube was monitored via lock-in detection (Standford Research 810 Lock-in Amplifier) synchronized to the repetition rate of the laser (1 kHz). The instrument response of this system was approximately 200 fs, measured as the sum frequency of the gate and excitation pulses. The polarization of the excitation pulse was set to the magic angle (54.7°) relative to the gate to remove anisotropic components from the time-dependent emission profiles. Typical excitation energies were 250-300 nJ/pulse, and the observed dynamics showed no dependence on intensity using energies up to 400 nJ/pulse.

4.2.4b Pump-Probe Spectroscopy.

The pump-probe experiments were done as described previously.[54] Briefly, a white light continuum probe (spanning 1000 – 451 nm) and the 405.5 nm pump were focused together into the sample using a 5 cm focus 90° parabola. The waist diameter at

the crossing was 150 μm. Typical pump energies ranged from 90-110 nJ/pulse, and the measured signals were found to be linearly dependent on pump energy up to 200 nJ/pulse. Samples were allowed to flow through a 1 mm path length quartz cell. The entire probe spectrum was collected using a 256 pixel silicon diode array on a shot-to-shot basis. The repetition rate of the pump was mechanically modulated to half the laser repetition rate and the change in optical density, ΔOD, was determined for every shot pair. The polarization of the pump beam relative to the probe was set to the magic angle (54.7°) to remove anisotropic effects. The instrument response, measured by crossing the probe continuum with the pump beam in an 80 μm thick type 1 BBO crystal (Super Optronics) cut from SFG in the range 752 – 451 nm, was ~90 fs fwhm and independent of probe wavelength. Data were corrected for the chirped continuum probe light as described previously.[54] Pump-probe transients were collected at individual probe energies using a photodiode fitted with a ±10 nm interference filter. An additional pump-probe trace taken at a delay of 11 ns was measured by inclusion of a static 3.3 m delay in the probe line.

4.3 Results.

4.3.1 Time-Integrated Absorption and Emission Spectra.

The absorption and emission spectra for **1-CO_2H** and ZnO NCs are shown in Figure 4.1. For **1-CO_2H** in solution, the absorption spectrum peaks at 376 nm. With the addition of ZnO NCs, there is additional absorption from the NCs at energies greater than ~ 340 nm and some broadening in the spectrum on the low energy side of the dye

absorption feature. The broadening appears to be the result of scattering caused by the NCs becoming less soluble in ethanol as full coverage of the NC with **1-CO_2^-** is approached. The ZnO NCs and **1-CO_2H** are each soluble in polar solvents; however it was found that the samples with dye:NC ratios around 50:1 had evidence of more limited solubility, with solutions becoming slightly cloudy. This ratio is comparable to the number of **1-CO_2^-** molecules that should fit on a 3 nm NC at monolayer coverage. As full coverage of the NC with **1-CO_2^-** is approached, the resulting complex presents a nonpolar exterior and becomes less soluble in ethanol. The broadening disappears and the solution remains transparent when the ratio is lowered (near 1:1). The fluorescence spectrum is peaked at 486.5 nm and has a quantum yield for **1-CO_2^-** alone of $\varphi_{fl} = 0.13$.

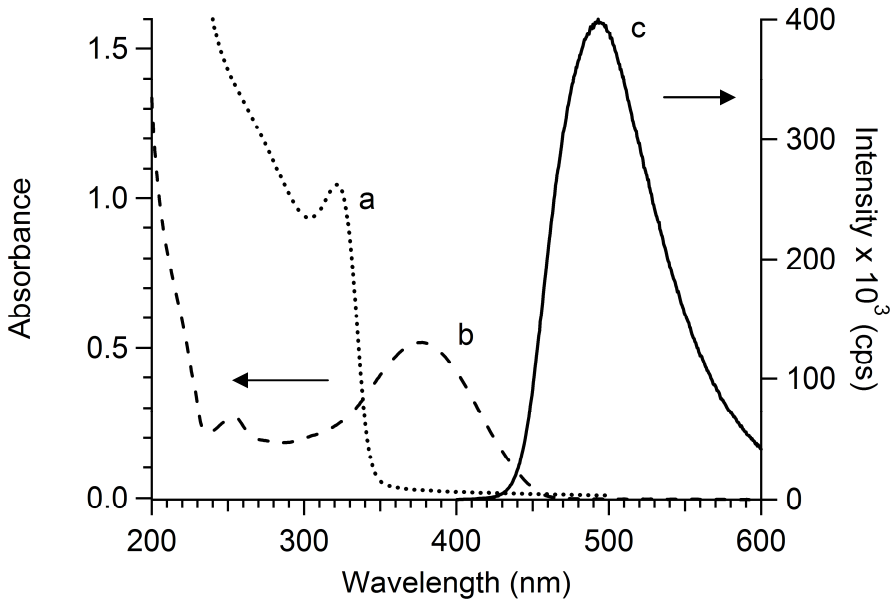

Figure 4.1 Absorption spectra of a) ZnO NCs and b) **1-CO_2H** in EtOH. Emission spectrum of c) **1-CO_2H** (λ_{ex} = 475 nm).

Emission spectra for **1-CO_2^-** and **(1-CO_2^-)$_n$**ZnO mixtures were indistinguishable in shape and varied only in intensity (Figure 4.2). The lack of evidence for any fluorescence from the NCs[137] suggest that excitation at 405.5 nm is limited to the dye.

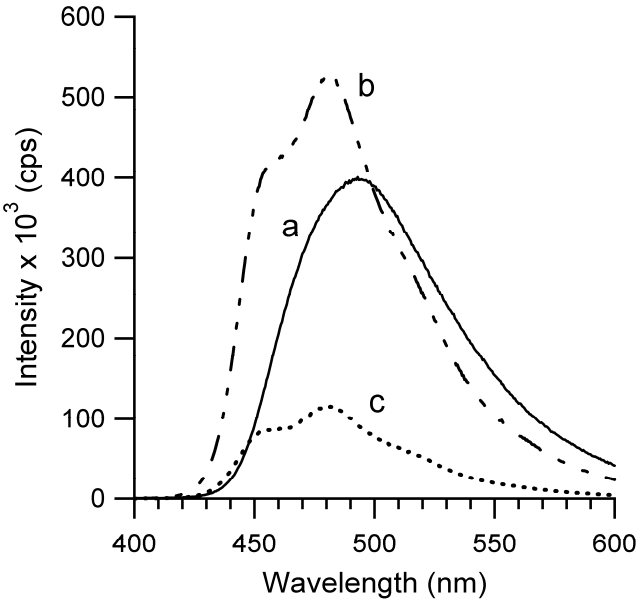

Figure 4.2 Emission of a) **1-CO_2H** b) **1-CO_2^-** and c) **(1-CO_2^-)$_n$**ZnO (λ_{ex} = 475 nm) in ethanol. The concentrations of **1-CO_2H** or **1-CO_2^-** for spectra a-c were 4.16 x 10^{-5} M and the concentration of ZnO NCs present in spectrum c was 2.00 x 10^{-6} M.

4.3.2 Spectroelectrochemistry.

Cyclic voltammetry was used to determine the reduction potential of **1-CO_2H**, and spectroelectrochemistry was used to obtain a spectrum for the oxidized form. Figure 4.3a shows the cyclic voltammogram (CV) of **1-CO_2^-** in which two processes are observed. A reversible oxidation is observed at E^0 = +1.11 V versus Ag/AgCl and an irreversible reduction is observed at E_{pc} = -1.73 V versus Ag/AgCl. Shown in Figure 4.3b are the changes observed in the absorption spectrum of **1-CO_2^-** upon bulk electrolysis of the sample at a potential ~0.1 V more positive than E^0. The growth of a new absorption band is observed with a maximum at 600 nm. The original absorption band at 390 nm diminishes and is accompanied by an energetic shift of ~3.5 nm. The appearance of an isosbestic point at 451 nm indicates clean conversion to the oxidized **1-CO_2^-** species. The original spectrum is regenerated when the potential is held at 0.00 V.

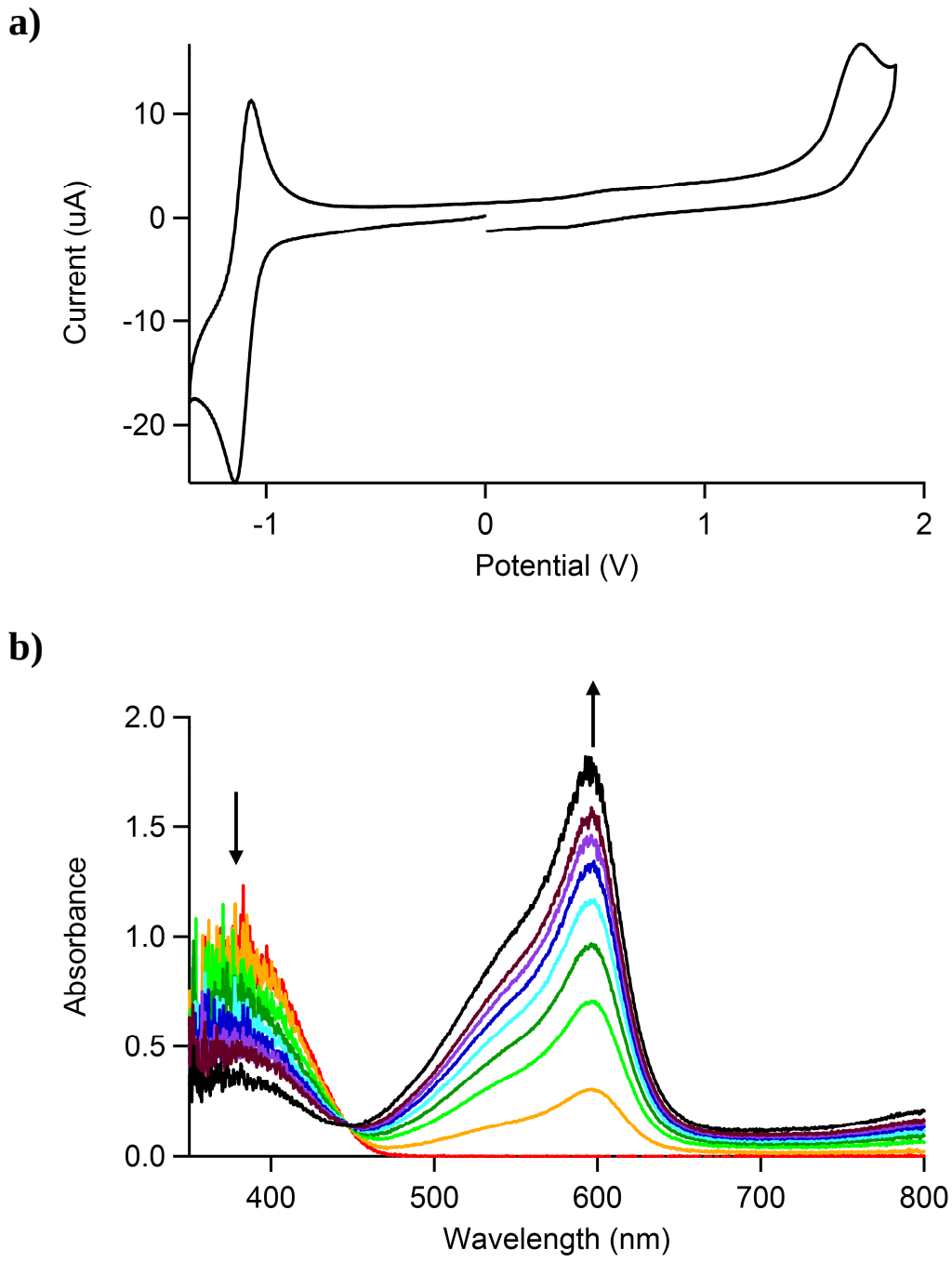

Figure 4.3 (a) Cyclic voltammogram of **1-CO_2^-** (1 mM) in 0.1 M $TBA^+PF_6^-$ / CH_3CN, υ = 100 mV/s. **(b)** The absorption spectrum of **1-CO_2^-** during bulk electrolysis of the reversible oxidative process.

4.3.3 Time-Resolved Experiments.

4.3.3a Dye Alone.

Time-resolved measurements were performed on **1-CO_2^-** alone in solution. Spectrally resolved pump-probe measurements are shown for a few selected delay times in Figure 4.4. The initially excited state appears within the time resolution of the experiment as a negative feature peaked (stimulated emission) centered at 486.5 nm, and a positive feature (transient absorption) centered at 653 nm. These features decay simultaneously, and there is correlated rise of a broad transient absorption centered at 577 nm, which persists for longer than the 11 ns range of our experiment. The transient spectra are very similar to previous reports for terthiophene and we assign the spectral components to the initially excited singlet state, both transient absorption and stimulated emission, transitioning to transient absorption of the triplet state after intersystem crossing occurs.[54,181,182]

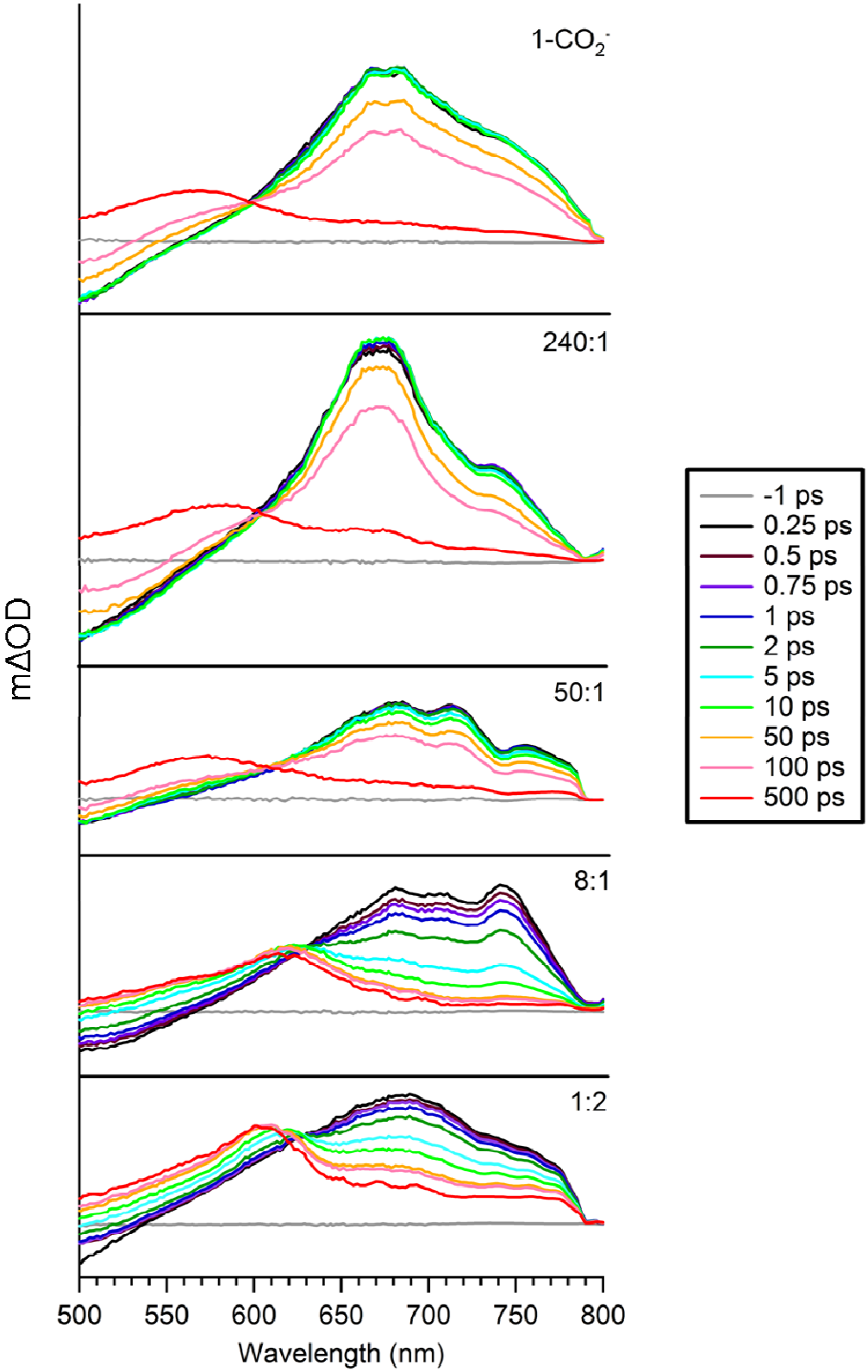
1-CO2-
240:1
50:1
8:1
1:2
mΔOD
500
550
600
650
700
750
800
Wavelength (nm)
-1 ps
0.25 ps
0.5 ps
0.75 ps
1 ps
2 ps
5 ps
10 ps
50 ps
100 ps
500 ps

Figure 4.4 Transient full frequency probe spectra for a series of **1-CO_2^-**:ZnO NC ratios.

Decay of the initially excited singlet state was independently measured using fluorescence upconversion of 486.5 nm emission and probing the transient absorption at 752 nm. The data are shown in Figure 4.5, including a direct comparison of the two methods. The measurements were fit to a single exponential decay with time constant τ_{lt}, Equation 4.1, and the resulting time constants following a least-squares minimization are shown in Table 4.1.

$$S(t) = Ae^{-t/\tau_{lt}} \tag{4.1}$$

TABLE 4.1 Single Exponential Decay Time Constants from Analysis of Upconverted Fluorescence (Fl) and Transient Absorption (TA) from **1-CO_2^-** Alone in Solution[a]

eV	**nm**	**τ_{lt} (ps)**
2.55 eV Fl	486.6 nm	190 ± 1
1.65 eV TA	752 nm	201 ± 2

a Errors are reported as the 95% confidence interval for the non linear regression fit. Data and fits are shown in Figure 4.5.

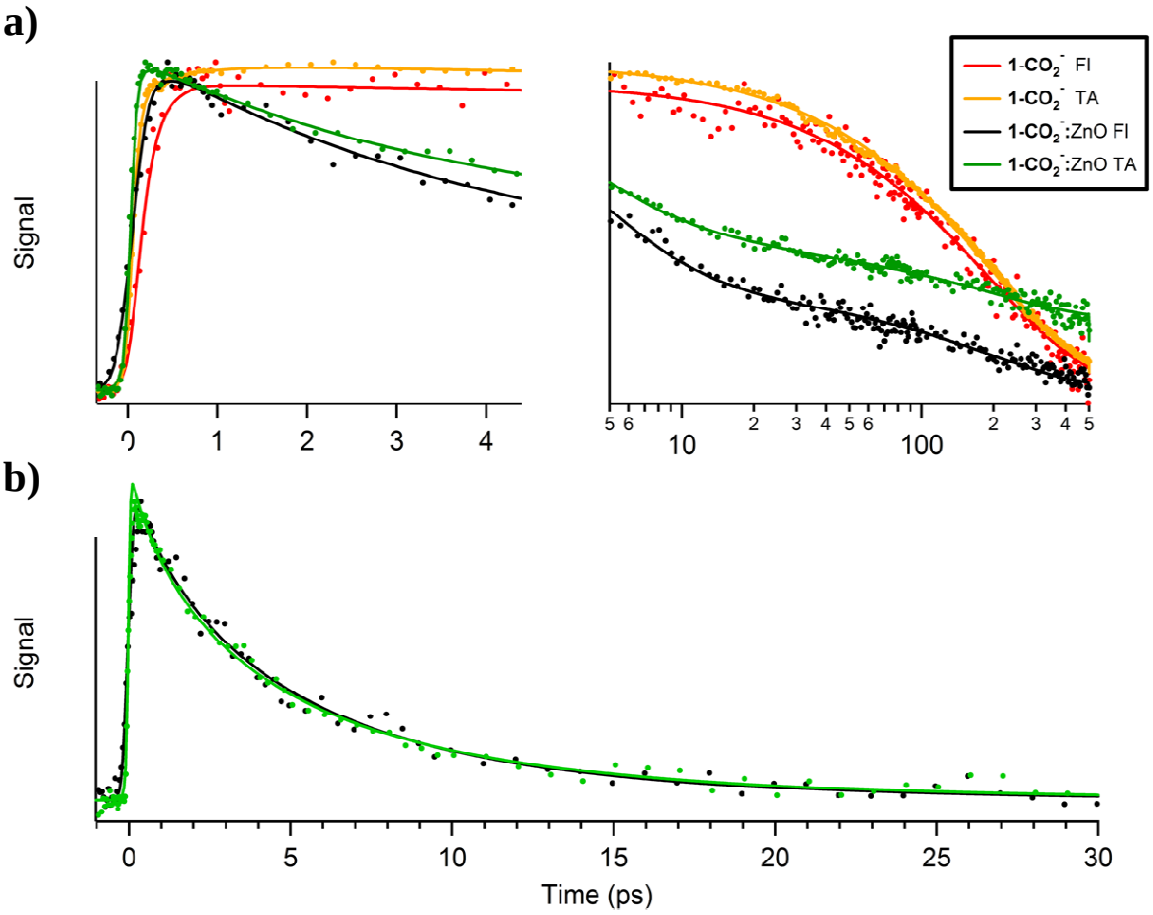

Figure 4.5 Comparison between upconverted fluorescence (Fl) at 486.5 nm and transient absorption (TA) at 752 nm for **1-CO_2^-** and a 1:1.5 **1-CO_2^-**:ZnO NC mixture with (a) the full transients and fits and (b) the residual following subtraction of the exponential lifetime component. Points are the raw data and lines are the fits as described in the text. Optimized fitting parameters are listed in Table 4.1.

Table 4.2 Fitting Parameters for Decay of Upconverted Fluorescence (Fl) and Transient Absorption (TA) from a 1:1.5 **1-CO_2**:ZnO NC Mixture.[a]

	τ_{et} (ps)	γ_{et}	*A*	τ_{lt} (ps)	*B*	*C*
2.55 eV Fl (486.6 nm)	3.9 ± 0.2	0.69 ± 0.03	0.90 ± 0.04	216 ± 2	0.29 ± 0.01	—
1.65 eV TA (752 nm)	3.8 ± 0.2	0.76 ± 0.02	0.63 ± 0.02	198 ± 2	0.24 ± 0.01	0.21 ± 0.01

a Errors are reported as the 95% confidence interval for the nonlinear regression fit. Data and fits are shown in Figure 4.5.

Both measurements fit well to a single exponential decay. Agreement between the determined time constants, 190 ps for fluorescence upconversion and 200 ps for transient absorption supports the fact that both methods probe the decay of the same state and that the transient absorption at 752 nm is dominated by the initially excited singlet state.

The fluorescence quantum yield was measured to be $\varphi_{fl} = 0.13$, and combining this value with the fluorescence lifetime of 190 ps, the radiative and nonradiative decay rate coefficients for **1-CO_2^-** are 6.8 x 10^8 and 4.6 x 10^9 s^{-1}, respectively.[183] This is consistent with previously reported rate coefficients for terthiophene[182] and with the observation that intersystem crossing is the primary singlet decay pathway for **1-CO_2^-** alone in solution.

4.3.3b (1-CO_2^-)$_n$ZnO Dispersions.

Figure 4.6 shows full spectrum transients for **(1-CO_2^-)$_n$**ZnO ratios from 250:1 to 1:2. With addition of ZnO NCs, the singlet transient absorption and stimulated emission develop a much faster decay component. Correlated with the more rapid decay of the initially excited state, a new feature grows in, peaked between the singlet and triplet absorption maxima at ~605 nm. Comparison with the cation absorption spectrum shown in Figure XX provides strong evidence that this new feature originates from absorption by the radical cation of **1-CO_2^-**. The accelerated quenching of the initially excited dye and correlated rise in absorption by the cation is assigned to electron transfer from the excited **1-CO_2^-** to the ZnO NC.

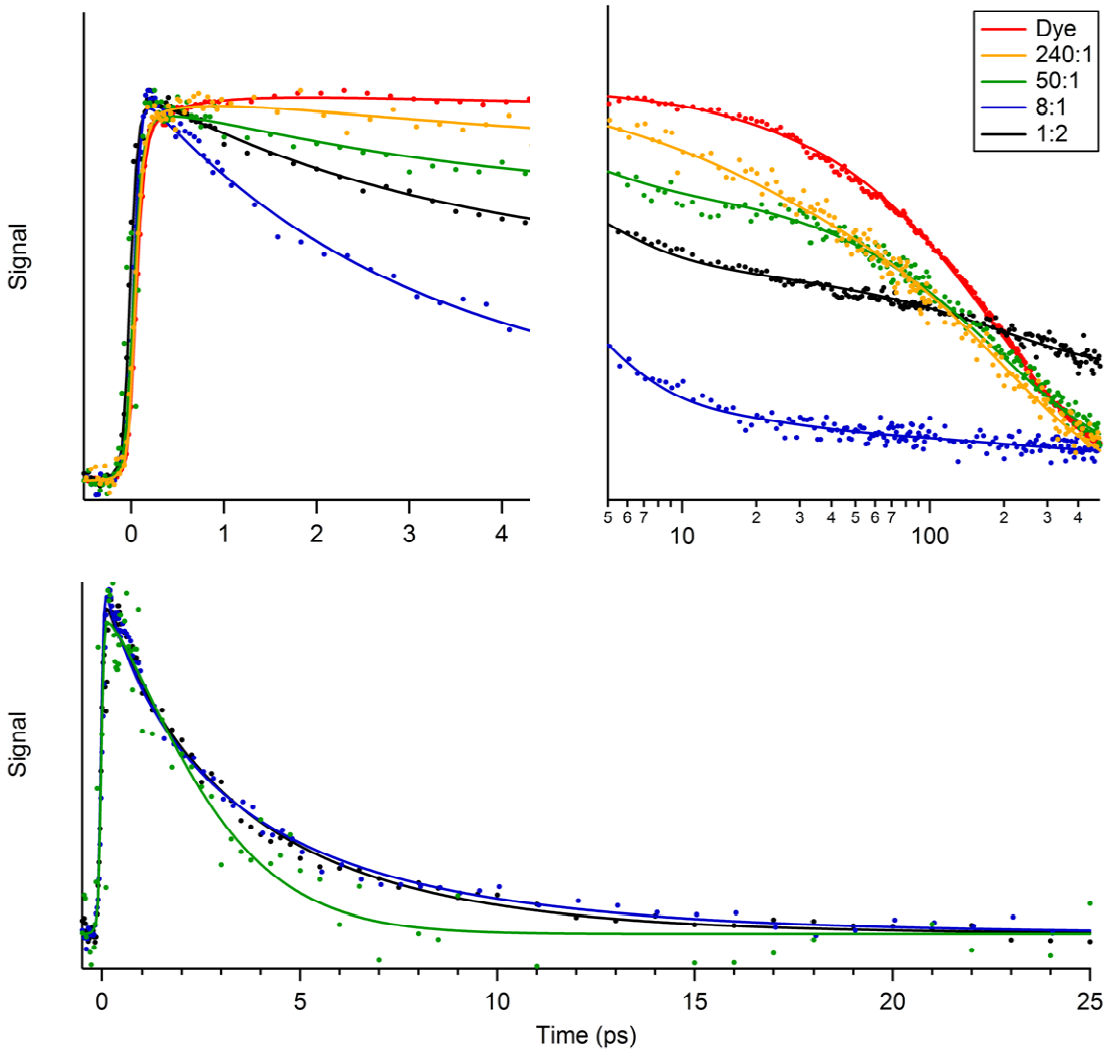

Figure 4.6 Transient absorption at 752 nm for **1-CO_2^-** and a series of **(1-CO_2^-)$_n$**ZnO ratios with (a) the full transients and fits and (b) the residual following subtraction of the exponential lifetime component. Points are raw data and lines are fits as described in the text. Fit parameters are given in Table 4.3.

Time scales for electron injection were determined from decay of the transient absorption at 752 nm and gain of the transient absorption at 605 nm. Transient absorption

has higher sensitivity than fluorescence upconversion, and this was needed to acquire reasonable transients at dye:ZnO NC ratios with higher dye coverages, where reduced solubility creates some limited, additional light scattering. However, transient absorption also has a much greater potential for interference from multiple overlapping signals than from upconverted spontaneous emission.

To establish that transient absorption at 752 nm is a reliable measure for quenching of the excited singlet state of **1-CO_2^-** in the presence of electron transfer, Figure 4.5 compares upconverted fluorescence at the peak of the **1-CO_2^-** fluorescence spectrum, 486.5 nm, with transient absorption at 752 nm for the 1:1.5 mixture **(1-CO_2^-)$_n$**ZnO. The primary difference between the data sets is the offset in the transient absorption at long delay times, which indicates residual absorption that appears static on the time scales of our experiments. The measure responses were fit to the sum of a stretched exponential decay, a single exponential decay, and in the case of transient absorption, a static offset (equation 4.2).

$$S(t) = Ae^{-(t/\tau_{et})^{\tau et}} + Be^{-(t/\tau_{lt})} + CH(t) \qquad (4.2)$$

H(t) is the Heaviside function defined as [H(t<0) = 0, H(t≥0) = 1]. The analysis proceeded by first fitting the tail, t>50 ps, to the single exponential decay and static offset on the right side of Equation 4.2. The data fit well to a single exponential, and the time constant from both experiments, τ_{lt} = 200 ps, indicates that this is the excited singlet lifetime component from unperturbed dye molecules. The unperturbed lifetime fit was

subtracted from the raw data and the remaining residual, shown in Figure 4.5b, was fit to the stretched exponential in the first term of Equation 4.2. This component is assigned to electron transfer. The optimized fitting parameters are listed in Table 4.2 and demonstrate excellent agreement between dynamics measured by the two different methods. Following subtraction of the long time tail, the early time dynamics are virtually indistinguishable, as shown in Figure 4.5b. We note that good fits to the residuals could also be obtained using a biexponential decay with time constants of ~3 and ~15 ps in place of the stretched exponential decay. The stretched exponential was selected because no discernible improvements in the fits were evident with the addition of a fourth adjustable parameter in the case of the biexponential decay.

Table 4.3 Fit Parameters for Decay of the Transient Absorption at 1.65 eV (752 nm) for a Series of Dye:ZnO NC Ratios[a]

dye:ZnO NC	τ_{et} **(ps)**	γ_{et}	***A***	τ_{lt} **(ps)**	***B***	***C***
1:2	3.2 ± 0.2	0.76 ± 0.03	0.5 ± 0.02	191 ± 2	0.25 ± 0.01	0.29 ± 0.01
8:1	2.8 ± 0.2	0.70 ± 0.02	1.01 ± 0.02	193 ± 5	0.06 ± 0.01	0.07 ± 0.01
50:1	3.1 ± 0.3	1.3 ± 0.2	0.21 ± 0.02	205 ± 2	0.69 ± 0.01	0.06 ± 0.01
240:1	17 ± 2	0.69 ± 0.1	0.23 ± 0.02	190 ± 2	0.73 ± 0.01	0.03 ± 0.01

a Errors are reported as the 95% confidence interval for the nonlinear regression fit. Data and fits are shown in Figure 4.6.

Figure 4.6 shows transient absorption at 752 nm for a series of **(1-CO_2^-)$_n$**ZnO ratios. These data were fit with Equation 4.2 following the same procedure outlined above, and the optimized parameters are listed in Table 4.3. At the lower dye:ZnO NC ratios there is a clear ~3.5 ps electron transfer component, and the amplitude of this component is anticorrelated with the amplitude of the unperturbed lifetime component. The quality of the data following subtraction of the unperturbed lifetime component is highest for the 8:1 and 1:2 ratios. At 50:1 the relative amplitude of the electron injection component has been reduced and there is additional scatter due to the lower solubility; however, these data still exhibit a clear 3 ps electron transfer component. The 250:1 sample is dominated by the unperturbed lifetime component, but there is evidence of an intermediate decay with an approximately 17 ps time scale left in the residual. The low signal-to-noise left in the residual at 250:1 reduces confidence in the fit and precludes additional analysis.

The maximum relative amplitude for the electron transfer component compared with the unperturbed lifetime component is found at the 8:1 **(1-CO_2^-)$_n$**ZnO ratio, suggesting this to be the cleanest measure of the electron transfer dynamics in the series. Having the maximum contribution from electron transfer at a dye:ZnO NC ratio of 8:1 (rather than 1:2, for example) is consistent with the static binding studies from Chapter 3 and will be considered in more detail in Section 4.4.2. The electron transfer time scales for the three lowest ratios are nearly identical, and the two highest quality residual data sets at 8:1 and 1:2 are practically indistinguishable, as shown in Figure 4.6b.

Time-dependent increase in the cation was probed by transient absorption at 602 nm for the 8:1 dye: ZnO NC sample and this is shown in Figure 4.7 along with the same experiment on a solution of **1-CO_2^-** . Probing at 605 nm was selected because this energy is very close to both the maximum in the cation absorption and the isosbestic point in the transient spectra of **1-CO_2^-** in solution, as shown at the top of Figure 4.3. As a result, time-dependent changes in the 8:1 sample should be dominated by absorption from the cation. Figure 4.7 shows that *both* **1-CO_2^-** and the 8:1 sample exhibits a large amplitude rise that plateaus by 50 ps. The 8:1 sample was fit with the sum of an instrument limited rise and a stretched exponential rise (equation 4.3).

$$S(t) = 1 - Ae^{-(t/\tau_{et})^{\tau_{et}}} \qquad (4.3)$$

The optimized fitting parameters are listed in Table 4.4. The time scale for the transient absorption rise at the peak of the cation absorption agrees very well with the decay in absorption at 752 nm in Table 4.3.

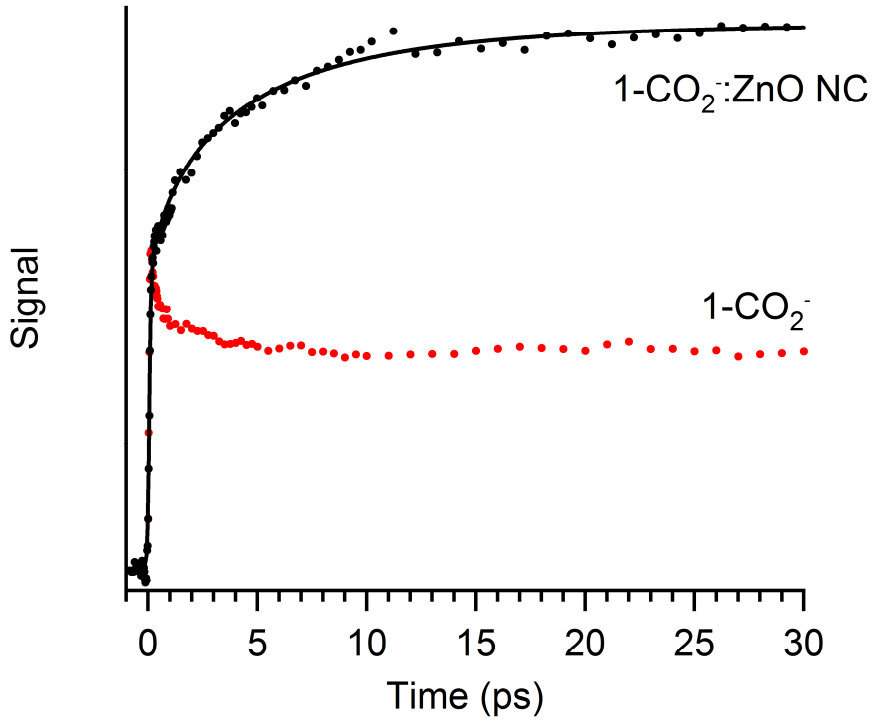

Figure 4.7 Transient absorption at 602 nm for **1-CO_2^-** alone and the 8:1 dye:ZnO NC ratio. Points are raw data and the line is the fit as described in the text. Fit parameters are given in Table 4.4.

Table 4.4 Fit Parameters for Transient Absorption at 2.06 eV (602 nm) for the 8:1 Sample[a]

τ_a (fs)	*a*	τ_{et} (ps)	γ_{et}	*A*
<70	0.49 ± 0.01	3.5 ± 0.1	0.70 ± 0.01	0.48 ± 0.01

[a] Errors are reported as the 95% confidence interval for the nonlinear regression fit. Data and fits are shown in Figure 4.7.

The average value of τ_{et} for the 1:1.5 dye:ZnO ratio fluorescence upconversion decay, the transient absorption decay at 752 nm for the 1:2, 1:1.5, and 8:1 ratios, and the transient absorption rise at 600 nm for the 1:1.5 sample is 3.5 ± 0.5 ps.

4.4 Discussion.

Figure 4.8 compares the ZnO conduction and valence band energy levels[125,184] with those of **1-CO_2^-** estimated via electrochemistry and spectroscopy. Electron transfer is thermodynamically favorable with the excited state of the terthiophene donor more than 1 eV above the conduction band edge of ZnO. All of the transient measurements presented here are well fit by the combination of an exponential lifetime that is consistent with the unperturbed dye (200 ps) and an additional stretched exponential component with a time constant of ~3.5 ps. The relative amplitude of the latter component depends on the **1-CO_2^-** : ZnO NC ratio, and the spectrum of the associated transient absorption is consistent with the spectrum measured for the dye cation using spectroelectrochemistry (figures 4.3 and 4.4). These facts and the correlation between the time scales measured for loss of the initially excited dye and gain of the dye cation spectrum indicate that electron transfer is the quenching mechanism.

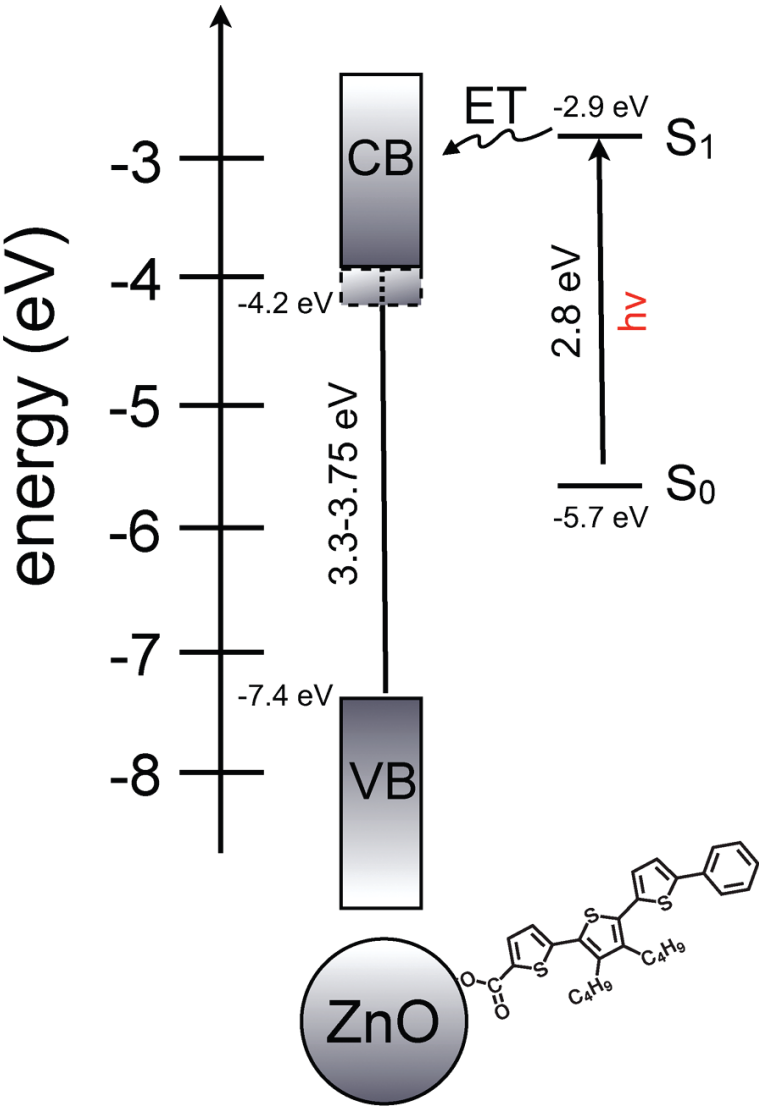

Figure 4.8 Energetic alignment between **1-CO_2^-** and ZnO NCs. All energy levels are relative to vacuum.

4.4.1 Electron Transfer Rate.

The ~3.5 ps injection component was the only electron transfer time scale found. The fact that the fits are improved by including a modest degree of stretch to the exponential time scale suggests some degree of heterogeneity in the electron transfer rates. Although the solution dispersed ZnO NCs provide a well-defined substrate in comparison with NC films, this likely reflects that their surfaces are not perfect single crystals. As a result, there will be some level of variance in the local environment between binding sites. However, the lack of any clearly separated electron transfer rates and the modest degree of deviation from a sing exponential fit, indicates that there are not multiple, significantly different binding sites and/or configurations contributing to electron transfer. This is in stark contrast with studies on NC films, where the additional complexity of the surfaces and potential for multilayer coverage leads to electron transfer rates that span orders of magnitude.[66-72,156,157] Observation of electron transfer on multiple time scales is typically associated with a variety of different binding sites.[67,80,185] In the more commonly studied TiO_2 system, Sundström and coworkers have demonstrated analogous isolation of a single characteristic electron transfer rate in dispersed colloids compared to the broad, heterogeneous kinetics found on the films.[108,109]

In comparison with investigations of electron injection kinetics on ZnO NC films, there have been very few direct measurements of the electron transfer time scales in dye:ZnO NC complexes dispersed in solution. Murakoshi et al. measured time-resolved fluorescence quenching of coumarin 343 (C343) and coumarin D-1421 (CD-1421) in methanol solutions of colloidal ZnO NCs.[35] They inferred electron transfer as the

quenching mechanism, and identified biexponential injection kinetics. Their data for C343 fit well using the time scales of 330 fs and 3.47 ps, with nearly equal weights, while slower time constants of 19.6 and 196.5 ps were required for CD-1421. Adam and Drew recently investigated the influence on the density of acceptor states in the electron transfer from a porphyrin donor to a dispersed ZnO NC acceptor. A single electron transfer time constant was found for each sample and the rate varied with average diameter of the ZnO NC acceptor from 240 to 370 ps.[118]

Our results for **1-CO_2H** agree well with the slower electron transfer time scale found for C343; however, we found no evidence for subpicosecond electron transfer and there is significant disparity in rates when comparing to the porphyrin donor. Within the framework of diabatic Marcus electron transfer, the electron transfer rate coefficient can be expressed in terms of the reorganization energy, λ, the free energy difference between the donor and the conduction band edge (CBE) of the acceptor, ΔG°, the energy above the CBE, *E*, the density of acceptor states, ρ(*E*), and the electronic donor-acceptor coupling, *H(E)*, (equation 4.4).[78,80]

$$k_{ET} = \frac{2\pi}{\eta} \int_{-\infty}^{\infty} dE\rho(E)(1 - f(E, E_F)) |\overline{H}(E)|^2 \frac{1}{\sqrt{4\pi\lambda k_B T}} \exp\times\left[-\frac{(\lambda + \Delta G_0 + E)^2}{4\lambda k_B T} \right] \quad (4.4)$$

The integration over *E* accounts for transfer into all energetically available conduction band states. In all four donors, the current dye, the coumarins, and the porphyrin, the donor state sits well above the ZnO conduction band edge energetically (~1 eV). We can

assume that λ is less than ΔG°, a similar system has been reported to have λ ~0.2 eV,[186] so the rate will be dominated by barrierless transfer to acceptor states that sit λ above the conduction band edge (λ + E = - ΔG°).[80] The result is that the rates are determined primarily by the density of acceptor states near barrierless transfer and the electronic coupling. While ρ(E) is expected to increase rapidly near the CBE, at energies well above the CBE the influence of ρ(E) becomes quite subtle with modest changes in E.[80,118] This leaves the electronic coupling as the largest potential influence on the relative k_{ET} values when comparing this set of donors. Agreement between the ~3.5 ps injection time constants for **1-CO$_2^-$** and C343 indicates similar donor-acceptor electronic coupling, while the much slower observed electron transfer from the porphyrin donor demonstrates a reduction in H(E) compared with **1-CO$_2^-$**. A simple explanation for the relative values of H(E) is suggested by the larger size of the porphyrin. Assuming the **1-CO$_2^-$**, C343 and the porphyrin all bind normal to the ZnO surface, the larger porphyrin increases the average distance between the donor and acceptor states reducing the overlap. However, any detailed explanation of the differences and quantitative values for the coupling will require future computational studies.

Murakoshi et al. contrasted their findings for ZnO with similar experiments using aqueous TiO_2 where injection dynamics were found to be much faster, 42 fs for C343 and 85 fs for CD-1421.[35] Sub-100-fs injection dynamics are fairly common for organic dye-TiO_2 systems, with similar rates reported for Fluorescein derivatives,[109,187] flavonoids,[188] alizarin and quinzarin,[103,119,189] triphenyl methane dyes,[190] and various dyes with catechol attachment groups.[99,123,191] One common conclusion among these studies is that the

electron transfer is very fast due to very large electronic coupling. This strong coupling results in the formation of what have been referred to as direct charge transfer to semiconductor states, and evidence for such states is provided by significant changes to the dye absorption spectrum after binding.[34,101,192,193] In the ZnO systems there is no evidence for such strong coupling and near adiabatic transfer. In addition, estimates of the density of states suggest that it may be as much as two orders of magnitude larger in TiO_2 than in ZnO.[67,194] The slower electron transfer rates to ZnO compared with TiO_2 are likely the result of both the weaker electronic coupling and a lower density of accepting states; see equation 4.4.

4.4.2 Dependence on 1-CO_2^-:ZnO NC Ratio.

On comparison of the 1:2, 8:1, and 50:1 dye:ZnO NC ratios, Table 4.3, the electron transfer rate remains unchanged within our experimental uncertainty, but there is a significant change in the amplitude of the electron transfer component relative to the residual, unperturbed **1-CO_2^-** lifetime component. The gain in electron transfer is correlated with the loss in the unperturbed fluorescence, but dependence on the **1-CO_2^-**:ZnO NC ratio is complicated, with maximum quenching of the fluorescence at the intermediate ratio of 8:1. Assuming that all bound dye molecules are quenched, a simple equilibrium for bound and unbound noninteracting **1-CO_2^-** molecules would predict a continuing decrease in fluorescence with the decrease in **1-CO_2^-**:ZnO NC ratio and a binding constant of 2.3 x 10^5 M^{-1} would leave almost no unperturbed fluorescence at a

1:2 ratio. Such a simple binding model is not sufficient to explain our observations and a detailed investigation of the complicated quenching behavior is presented in Chapter 3.

The work detailed in that chapter demonstrates deviation from standard Stern-Volmer behavior with a minimum in the fluorescence of **1-CO_2^-** at a ratio of ~20:1 **1-CO_2^-**:ZnO NCs and subsequent increase in the fluorescence of **1-CO_2^-** with decreasing dye:ZnO NC ratios. The conclusion often inferred from data of this type is that it indicates concentration quenching; i.e., at intermediate **1-CO_2^-**:ZnO NC ratios electronic interaction between proximally bound dye molecules provides the quenching mechanism.[34,173] However, the results presented here identify electron transfer as the primary quenching mechanism and demonstrate that the amplitude of the electron transfer component follows the same trend as the fluorescence quenching. The 50% decline in the electron transfer contribution going from a ratio 8:1 to 1:2 is correlated with recovery of the static fluorescence, confirming electron transfer as the quenching mechanism and demonstrating that concentration quenching is not responsible for the observed deviation from standard Stern-Volmer behavior. This conclusion is also supported by the lack of any decay components in the transient measurements in addition to electron transfer and unperturbed fluorescence. As outline and discussed in detail in Chapter 3, the complicated quenching behavior can be explained by competitive binding of **1-CO_2^-** between the ZnO NCs and free Zn^{2+} cations in solution.

4.5 Conclusions.

We have measured the electron transfer rates from the excited state of a new thiophene-based organic dye molecule bound to colloidal ZnO NCs dispersed in ethanol. The results show isolation of a single electron transfer time constant, τ_{ET} ~3.5 ps, in the dispersions and demonstrates that the complexes in solution lack the broad range of binding and associated injection rates typically found on nanocrystalline films. The rate is comparable to previous measurements for C343:ZnO NC dispersions but no evidence was found for an additional subpicosecond injection component analogous to that reported for C343 and commonly reported for injection into TiO_2. The electron transfer rate was two orders of magnitude faster than recently measured rates of injection from a porphyrin donor. Arguments were presented to support the conclusion that the differences in electron transfer rates are primarily the result of differences in donor-acceptor electronic coupling.

The results establish that electron transfer is the primary mechanism for fluorescence quenching of **1-CO$_2^-$** by ZnO NCs at all **1-CO$_2^-$**:ZnO NC ratios. In the context of previous chapter investigating the complex quenching behavior in this system, this conclusion excludes concentration quenching as a significant contribution to quenching at high surface coverages and supports the competitive binding model presented in Chapter 3 to explain deviation from standard Stern-Volmer behavior. The lack of concentration quenching even at high surface coverage indicates that the molecular structure of **1-CO$_2^-$** provides sufficient interference to hinder significant electronic interaction between adjacent chromophores at the oxide surface. The two butyl groups on the center ring probably play an important role in disrupting potential

interactions between dye molecules. The lack of concentration quenching while maintaining the ~3.5 ps electron injection as the dominant quenching mechanism at full surface coverage is a positive attribute of this new molecule in the context of a DSSC, where parasitic nonradiative deactivation could decrease charge injection quantum yields.

Chapter 5: Synthesis and Characterization of Zinc Oxide and Zinc Hydroxide

5.1 Introduction.

Zinc oxide is a wide bandgap semiconductor with extensive applications in optoelectronics, pigments, microelectronics and catalysts.[195] It has a direct band gap of 3.37 eV and transmits approximately 85 percent of incident visible light.[196] Synthesis of ZnO nanocrystals (NCs) emerged in the 1980s,[125,131,197] with many other methods of synthesis developed since then.[125,129-132,159,160,197-212] Most syntheses in solution use divalent zinc sources like zinc acetate or acetylacetonate.[125,130-132,160,199,200,213,214] This method of reacting a zinc salt with a hydroxide source in alcohol has the advantage of using commercially available, inexpensive precursors and relatively simple procedures but several problems exist, including unwanted particle growth with storage in solution, irreversible dissolution after removal of solvents, and the presence of impurities. Other methods involve precursors such as diethylzinc[202,203] or dicyclohexylzinc[129,159,198] both of which are pyrophoric. To a lesser extent, zinc dialkoxides have been used but simple zinc dialkoxides monomers tend to form oligomers in an effort to satisfy the coordination requirements of the zinc metal center, rendering them relatively insoluble. In one example of addressing this issue, Luo, *et al*. chelated a bulky amine to the zinc to make it soluble.[215] When heat is applied, the compound undergoes β-elimination to form ZnO, an amine and an alkene as shown in equation 5.1.

$$R_2N\text{-}Zn\text{-}OR' \xrightarrow{\Delta} ZnO + R_2NH + R' \qquad (5.1)$$

Even when ZnO is successfully synthesized from most synthetic procedures, the use of long-chain alkyl groups are necessary to cap the surface of the ZnO to obtain NCs or nanorods that are dispersible in organic solvents. Neutral surfactants include long-chain amines,[129,159,198] trioctylphosphine oxide (TOPO),[130,203] octanethiol,[199] and a combination of trioctylamine and oleic acid.[200] Transparent ZnO colloidal dispersions could be obtained in a variety of alcohols but precipitation gradually took place due to particle growth and/or agglomeration without the above mentioned surfactants protecting the surface.[125,131,132,160]

Chaudret and coworkers had previously prepared ZnO NCs capped with long-chain amines and used dicyclohexylzinc as the molecular precursor.[129,159,198] Luo, *et al.* synthesized ZnO NCs from bis(diisobutylamido zinc) - an amido zinc precursor – and capped them with hexylamine.[127] Using a set of 3.7 nm diameter NCs, it was determined that there were 200 hexyl groups on the surface of a ZnO NC, half of which were bound as ammonium ions and the other half as carbamates. Each hexyl group would take up ~22 $Å^2$ which is similar to the surface area occupied by straight chain alkyl thiols on gold surfaces[216] or tetradecylamine on ZnS nanorods.[217] It was interesting that the hexylamine surfactant had turned into hexylammonium hexylcarbamate (HAHC) from its exposure during the synthesis to atmospheric CO_2. This step proved to be an imperative one when making monodispersed ZnO NCs. Alkylammonium alkylcarbamates were found to stabilize ZnS NCs[218] and also form thermally reversible organogels with a variety of organic solvents.[219-221]

As previously described, precipitating ZnO from alcohols can result in relatively stable colloidal dispersions of nanocrystals[125,131,132,137,138,197,222] whereas synthesis from aqueous solutions yields formation of ZnO that frequently requires surfactants on the surfaces in order to be stable.[138]. Zinc hydroxide is believed to be an intermediate product in the aqueous synthesis of ZnO and its formation may be the reason these dispersions are often turbid and require surfactants for stability. [125] As we attempted to better understand ZnO NC formation, the role of $Zn(OH)_2$ was briefly explored. There are four $Zn(OH)_2$ polymorphs (α-, β-, γ-, and ε-) two of which (γ- and ε-) are relatively stable under standard, atmospheric conditions.[223-227] Understanding which, if any, $Zn(OH)_2$ polymorph is present as an intermediate product during a reaction could provide more information on the mechanisms leading to the final ZnO product.

5.2 Experimental Details.

5.2.1 General.

Absolute ethanol, 1-propanol, tetramethylammonium hydroxide ($NMe_4OH·5H_2O$), zinc acetate ($Zn(CH_3COO)_2·2H_2O$), zinc sulfate ($Zn(SO_4)·H_2O$) sodium hydroxide (NaOH), dimethylsulfoxide (DMSO), and ethyl acetate were used without further purification. Hexanes were dried with alumina in an MBraun solvent purification system. Hexylamine was distilled over calcium hydride under nitrogen. Hexylammonium hexylcarbamate (HAHC) was prepared as described in the literature.[228] Electronic absorption spectra were collected on an Online Instruments Cary-14 conversion spectrometer. The steady-state emission spectra were recorded on a Spex

Fluorolog 1680 0.22 m double spectrometer using a xenon source. Fluorescence spectra were corrected to compensate for changes in the instrument's sensitivity at longer wavelengths. All spectroscopy was performed in quartz cuvettes with a 3 mm path length using absolute ethanol unless otherwise noted. The IR spectra of solids (KBr pellet) were recorded on a Nicolet MAGNA-IR 560 spectrometer. The solid-state NMR spectra were obtained with the magic angle technique on a Varian VNMS spectrometer operating at a ^{1}H frequency of 600 MHz. The ^{15}N NMR spectra were obtained using the cross-polarization method with ^{1}H decoupling and were referenced to an NH_4Cl standard at 41.5 ppm.

5.2.2 Synthesis of ZnO NCs from Zinc Acetate and Sodium Hydroxide in Ethanol (Searson Method).

The synthesis of ZnO nanocrystals was adopted from Searson and coworkers[229] and a typical procedure is described below. A 0.0125 M ethanolic solution of $Zn(CH_3COO)_2 \cdot 2H_2O$ (72 mL, 1.0 mmol) was stirred at 50 °C until becoming optically clear. Meanwhile, a 0.02 M ethanolic NaOH (20 mL, 0.16 mmol) solution was prepared at 60 °C, stirring vigorously until dissolved. From this flask, 6.4 mL was removed and added to 21.6 mL of pure ethanol which was then added to the $Zn(CH_3COO)_2 \cdot 2H_2O$ solution. The contents of the flask were covered, heated to a temperature of either 35 or 55 °C and allowed to stir for 5 - 120 min. The dispersion was clear and colorless as it cooled to room temperature if the reaction time was less than ~60 min and turbid if the reaction time was greater than ~60 min. The optically clear dispersions were stable at

room temperature for approximately three weeks before a white precipitate became visible. The diameters of the NCs were determined using electronic absorption spectra as described in section 3.3.1.

5.2.3 Synthesis of ZnO NCs from Zinc Acetate and Tetramethylammonium Hydroxide in Ethanol (Gamelin Method).

The synthesis of ZnO nanocrystals was adapted from Gamelin and coworkers.[130] A 0.55 M ethanolic solution of $NMe_4OH•5H_2O$ (7.73 mL, 4.25 mmol) was dripped into a 0.1 M DMSO solution of $Zn(CH_3COO)_2·2H_2O$ (25 mL, 2.51 mmol) over 30 to 180 s and allowed to stir at room temperature (ca. 24 °C) for 5 - 30 m. The longer reaction times led to larger particles. The diameters were determined using electronic absorption spectra as described in section 3.3.1. To induce precipitation, an aliquot of the solution was removed and added to three times the volume of ethyl acetate. The turbid mixture was centrifuged using a LW Scientific Ultra – 8V centrifuge. After decanting the liquid the white pellet was added to ethanol to yield an optically clear dispersion of ZnO nanocrystals. Attempts to clean the ZnO NC surface by reprecipitating the NCs and redispersing them in ethanol yielded turbid dispersions that were not useful for the experiments described here.

5.2.4 Synthesis of ZnO/HAHC.

The synthesis of ZnO NCs is described above in section 5.2.3. The solution of $NMe_4OH•5H_2O$ and $Zn(CH_3COO)_2·2H_2O$ was stirred for 30 min at room temperature, at

which point 15 mL was transferred to a flask containing 25 mL of ethyl acetate to induce precipitation of the NCs. From the turbid mixture, 20 mL was removed and centrifuged. After decanting the liquid, the NCs were dispersed in ethanol (15 mL) to yield an optically clear dispersion. To this, HAHC (0.060 g) was added, and the dispersion was stirred for 24 h, during which time it became turbid. The ZnO NCs were precipitated with acetonitrile, centrifuged, separated from the liquid phase by decanting and allowed to dry in air for 30 min. The NCs were dispersed in hexanes to yield an optically clear mixture that was stable for several days if a small amount (ca. 0.1 mg) of HAHC was added to the hexanes. The ZnO/HAHC could also be dispersed in ethanol over time and remained stable if a small amount of the HAHC was added to the dispersion. These HAHC coated samples were made to compare the spectroscopy and dispersibility of the zinc acetate-based ZnO NCs to those of the $[Zn(N^{i}Bu_2)_2]_2$ –based ZnO NCs, also coated with HAHC.[127]

5.2.5 Reaction of ZnO NCs to $N_{2\,(g)}$ and $O_{2\,(g)}$.

A series of experiments were performed with ZnO NCs synthesized from Gamelin's method, described here in Section 5.2.3. The NCs had an average diameter of 3.8 nm and the ethanolic dispersion was slightly cloudy. A small amount of ethanolamine (two drops) was added to cap the ZnO surface and create an optically clear suspension which remained stable in EtOH for two months. The dispersion was purged for 10 min with N_2 gas, 0.5 mL was transferred via syringe to a purged and capped cuvette, and the emission intensity was recorded (λ_{ex}=290 nm). The ZnO NCs were syringed back into the

original flask which was purged for 30 seconds with O_2 gas. An equal aliquot (0.5 mL) was transferred via syringe to a purged and capped cuvette, and the emission was recorded for the O_2 purge. This cycle of N_2 then O_2 purging was repeated a total of seven times. Solvent that was lost due to evaporation during purging was replaced with pure solvent undergoing the same N_2/O_2 treatment. Electronic absorption data were also recorded to monitor any change in the ZnO NCs.

5.2.6 Synthesis of $Zn(OH)_2$.

Gamma zinc hydroxide was prepared according to literature methods.[225] A ~4 M solution of NH_4OH was prepared by diluting 3.2 mL of concentrated ammonia (29.6% by mass) up to 20 mL with water. This solution was slowly added via pipette to a rapidly stirring 0.185 M aqueous solution of $Zn(SO_4)\cdot H_2O$ (30 mL, 5.56 mmol) where a white precipitate immediately formed. Approximately 5 mL of NH_4OH was added to the $Zn(SO_4)\cdot H_2O$ solution. The mixture was filtered and rinsed very well with water. A scraping of the white solid was added to a wide, shallow jar where it was dissolved with a small amount of concentrated ammonia. The jar was placed in a desiccator containing concentrated sulfuric acid (H_2SO_4). After 24 h, a fluffy, powdery precipitate formed on the bottom of the jar.

Preparation of ε-$Zn(OH)_2$ was attempted four times following the literature procedure but all trials were unsuccessful.[230]

5.3 Results.

5.3.1 Zinc Oxide Nanocrystals.

This specific synthetic method of producing ZnO NCs as described by Searson and coworkers was chosen for its simplicity and the optically clear dispersions it yields.[229] The electronic absorption spectra of ZnO NCs allowed to stir in the reaction mixture for up 120 min before they were removed show a systematic red shift over time as the diameter of the NCs increased (Figure 5.1). After 15 min in the reaction mixture, the NCs had an average diameter of 2.44 nm which increased to 2.65 nm in diameter after reacting for 120 min. This is consistent with both experimental and theoretical studies associating bandgap energy with NC diameter.[125,130,132,137-139,141,142,231] As the reaction progresses, the NCs become larger which decreases the energy between the conduction and valence bands and shifts the energy of absorbed light to higher wavelengths.

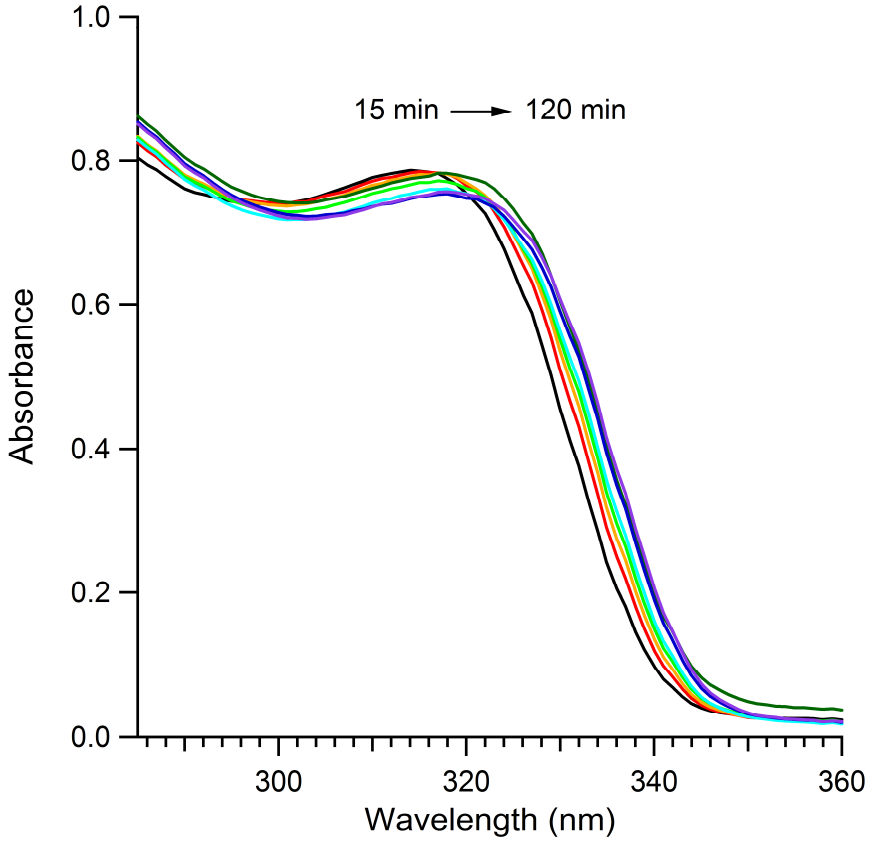

Figure 5.1 Effect of reaction time on electronic absorption spectra of ZnO NC dispersions. Small aliquots of NCs were removed after 15, 30, 45, 60, 75, 90, 105, and 120 minutes and their electronic absorbance recorded. The spectra illustrate a small but discernible bathochromic shift as the reaction time increased.

An attempt was made to use 1-propanol as the solvent instead of absolute ethanol as a way to decrease growth time when reproducing more of Searson's group's work. It was found that ethanol yielded more consistent and favorable results with respect to the ZnO synthesis and was determined to be the solvent of choice. Although a simple and short procedure, the synthesis described above resulted in dilute dispersions of ZnO NCs with low yields even when attempts to concentrate it were made. Nanocrystals could not

be precipitated in a reproducible manner which made us unwilling to pursue this procedure further. The characterization of the ZnO NCs produced via the process described by Gamelin and coworkers is described in Section 3.3.1 of this thesis.

5.3.2 Reaction of ZnO NCs to $N_{2\,(g)}$ and $O_{2\,(g)}$.

Exposure of the ZnO NCs in EtOH to atmospheres of either N_2 or O_2 drastically changed the intensity of the emission centered at 535 nm when λ_{ex}=290 nm. As illustrated in Figure 5.2, the emission decreased by ca. 50% when the NCs were purged thoroughly with N_2 after being exposed to O_2.

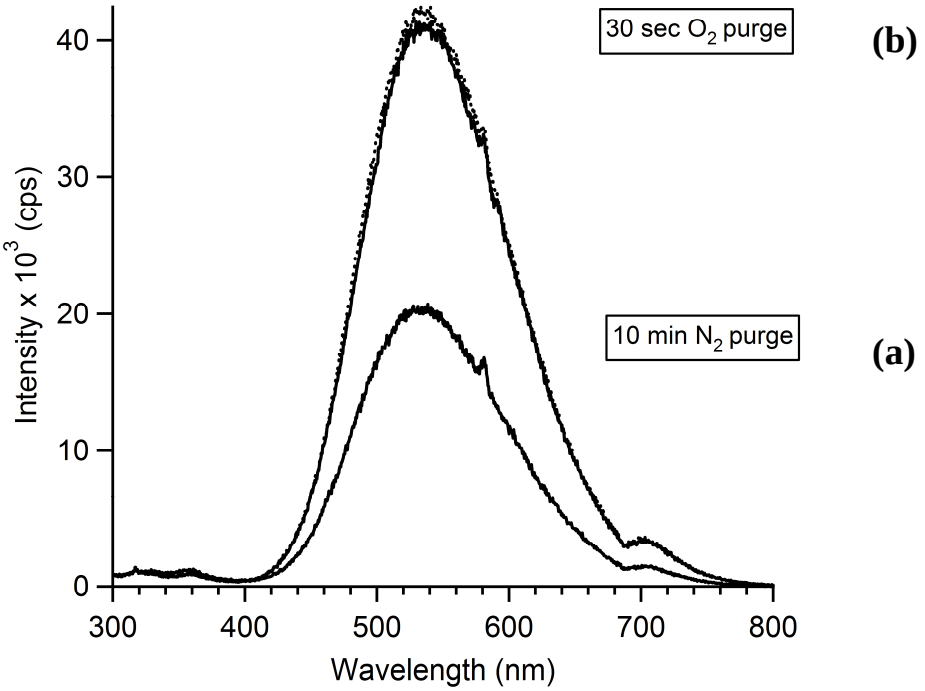

Figure 5.2 Emission spectra of ZnO NCs in EtOH after (a) a 10 min N_2 purge followed by (b) a 30 second O_2 purge (λ_{ex} = 290 nm).

The emission recorded after each cycle of N_2/O_2 purges are displayed chronologically (from left to right) in Figure 5.3. Each time the ZnO NCs were exposed to N_2, the intensity of the green, visible emission decreased by approximately half. After (re)exposure to O_2, the emission returned to its approximate original intensity. In the fourth (dark green), fifth (blue) and sixth (purple) cycles, the N_2 purged NCs were exposed to a 5 s O_2 burst, as compared to a 30 s burst, to see how quickly the emission responded. In each case the intensity had nearly returned to that of the previous O_2 purge but in 1/10 the time. Due to the 5 s time constraint for those samples, only the wavelengths near the 535 nm peak were collected.

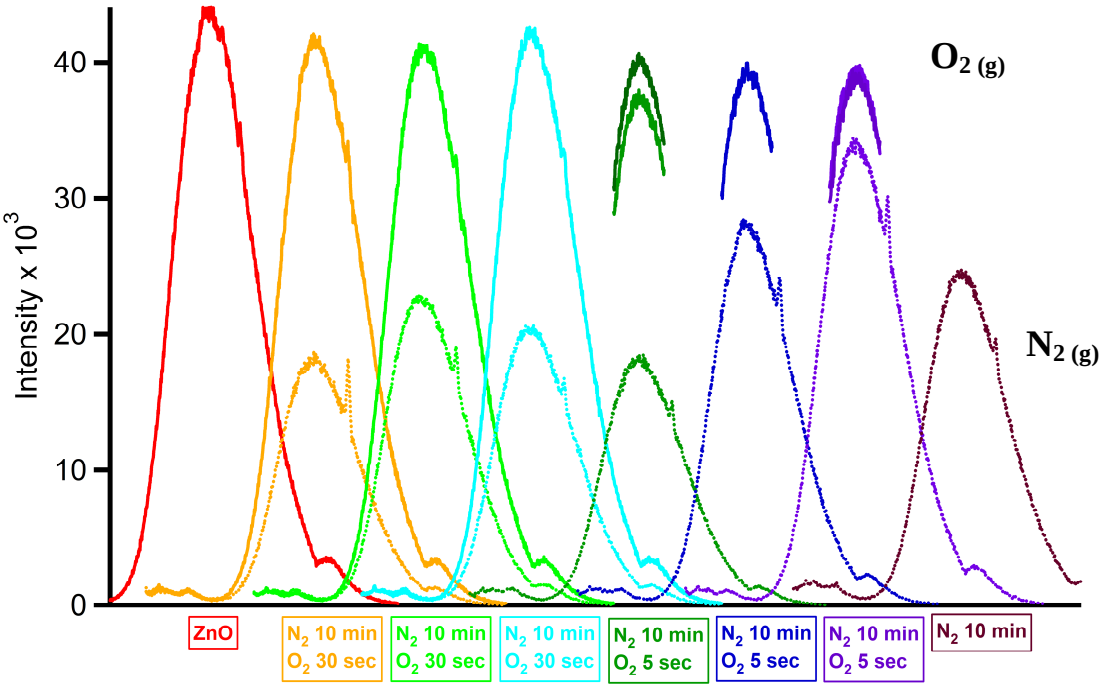

Figure 5.3 Emission spectra of ZnO NCs in EtOH after purging the solution with either N_2 for 10 min (dotted line) or O_2 for 30 s (solid line). The process was repeated seven times, as illustrated above (λ_{ex} = 290 nm).

Electronic absorbance spectra were recorded for every sample throughout the experiment to monitor the ZnO, although only two traces are displayed in Figure 5.4. The spectrum before the purging began and then after the experiment was completed are nearly identical, suggesting that changes in NC emission intensity are not a result of ZnO decomposition or precipitation.

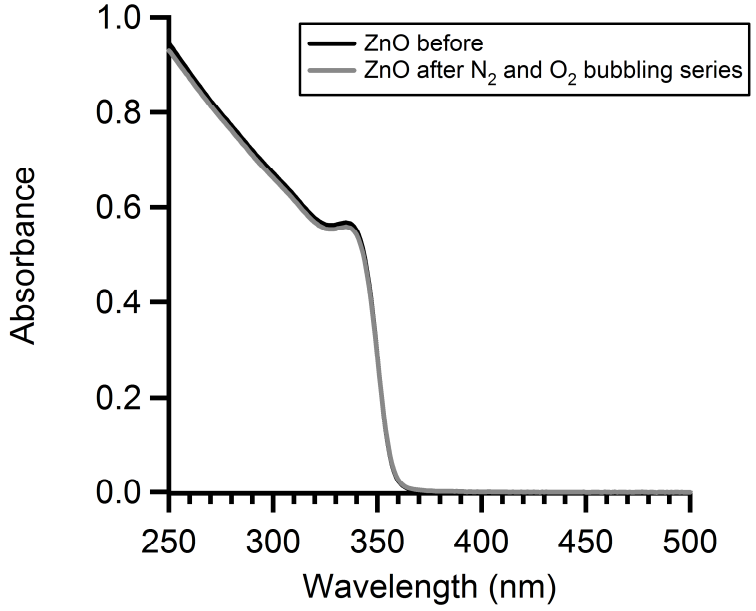

Figure 5.4 Electronic absorption spectra of ZnO NCs in EtOH before (black) and after (gray) the series of N_2/O_2 purges.

5.3.3 Characterization of γ-$Zn(OH)_2$.

Despite many efforts, the ε-$Zn(OH)_2$ polymorph, as it was described in the literature,[230] could not be isolated. However, crystals of the γ-$Zn(OH)_2$ polymorph were easily isolated and X-ray diffraction (XRD) patterns were obtained to verify the molecule's identity and compare it to that of wurtzite ZnO (Figure 5.5).

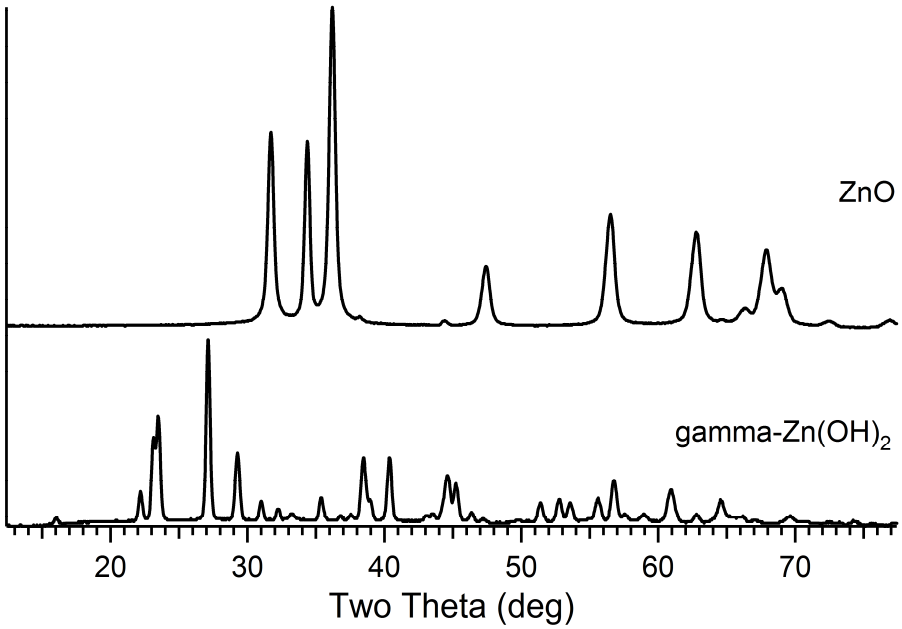

Figure 5.5 Experimentally obtained XRD patterns of ZnO and γ-$Zn(OH)_2$.

Using the Cerius[2] program at the Minnesota Supercomputing Institute, we constructed the cell parameters of the gamma form of $Zn(OH)_2$ from literature values[232] and allowed the computer to generate a theoretical XRD pattern (gray) which was overlaid in Figure 5.6 on an experimentally obtained pattern (black).

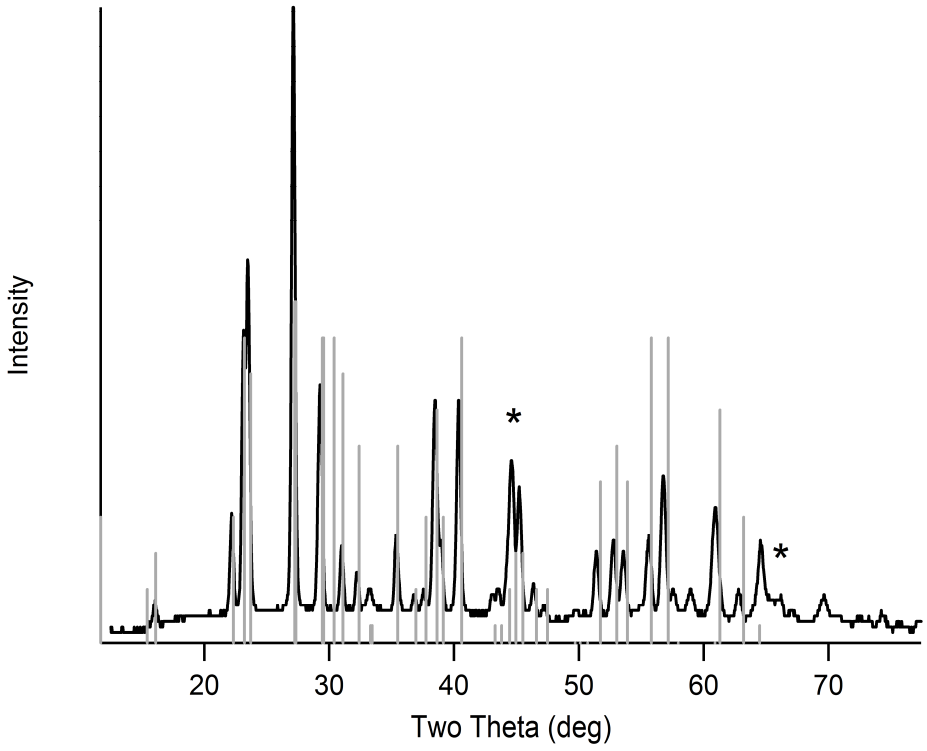

Figure 5.6 Computer generated XRD pattern for γ-$Zn(OH)_2$ (gray) overlaid on an experimentally collected XRD pattern (black) obtained from the synthesis described in section 5.2.5. Aluminum-backing peaks are indicated with an asterisk.

The Cerius^2 program was also used to construct schematics of the unit cell structures for both γ-$Zn(OH)_2$ and wurtzite ZnO (Figure 5.7) to highlight the differences between the two materials.

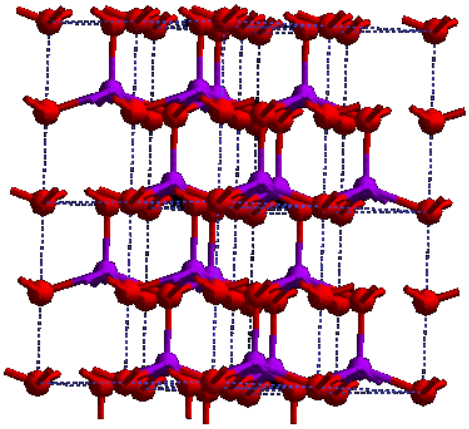

ZnO

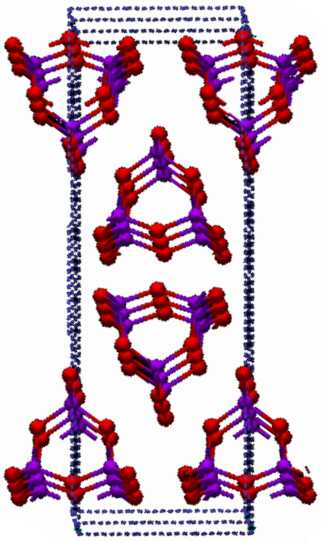

γ-$Zn(OH)_2$

Figure 5.7 Cerius^2-generated computer images of ZnO and γ-$Zn(OH)_2$ based on their known unit cell specifications, omitting hydrogens and showing the zinc molecules in purple and the oxygen molecules in red.

5.4 Discussion.

5.4.1 ZnO/HAHC.

The reaction of ZnO NCs prepared using zinc acetate (ZnO_{ZnOAc2}) with HAHC yields stabilized NCs that appear similar, but not identical, to samples of ZnO coated with HAHC synthesized by Luo, *et al*. The most notable difference is that the ZnO_{ZnOAc2} samples can be dispersed in ethanol, yielding stable, transparent dispersions whereas ZnO/HAHC samples from the $[Zn(N^{i}Bu_2)_2]_2$ method cannot. Both samples can be dispersed in hexanes. Infrared spectroscopy indicates that the carbamate group is present on the ZnO_{ZnOAc2} samples, but there exist small differences in relative peak intensities. The ability to disperse the ZnO_{ZnOAc2} NCs in ethanol may be due to the ability of a portion of less tightly bound surfactants to reorient with their polar head groups facing the solvent. While more work is needed to define the differences, we suggest that in the $[Zn(N^{i}Bu_2)_2]_2$ samples, where the surfactant was present during the entire synthesis, the surfactant is more fully ordered on the ZnO surface, forming a more stable shell. The ordered shell does not rearrange in response to a change in solvent; thus, the ZnO NCs from $[Zn(N^{i}Bu_2)_2]_2$ do not disperse in ethanol despite exposure to lengthy stirring and sonication.

5.4.2 Effect of $N_{2\,(g)}$ and $O_{2\,(g)}$ on ZnO Surfaces.

The surface of a nanocrystal is important when thinking about its properties because of the high surface-to-volume ratio present. In ZnO systems, it has been shown

that surface adsorbates, such as solvent molecules, dissolved gas or reaction byproducts, can influence the properties of a suspension of NCs.[125] The "green" emission often observed in ZnO NCs has been attributed to recombination of an electron in a trap state to a deeply trapped hole.[233] Van Dikjen and coworkers suggested that the emission was from the recombination of electrons in oxygen vacancies with photoexcited holes in the valence band.[233] Based only on the experiment described in Section 5.2.5, we conclude that oxygen adsorbed to the surface of ZnO NCs has an impact on the green emission but did not pursue the topic with additional experimentation. As discussed in Chapter 3, the high energy on the surface of ZnO NCs is partially responsible for the release of Zn^{2+} ions into solution.

5.4.3 $Zn(OH)_2$.

As stated previously, $Zn(OH)_2$ is a polymorphic compound. The alpha form was made at <110 kbar at temperatures ranging from room temperature to 600 °C, depending on reaction time.[224] The beta form has a brucite-like structure with stacked sheets of $Zn(OH)_2$ octahedrons. Each octahedron is composed of a Zn^{2+} ion coordinated to three $(OH)^-$ ions which neutralizes any charge. Because of this, there are only weak, residual interactions between the layers of $Zn(OH)_2$ and the material is easily cleaved. It can be produced at 110-120 kbar and 400 °C.[224] The structure for γ-$Zn(OH)_2$ is formed from ZnO_4 tetrahedra with three sharing corners to form a ring. The rings stack in the c-direction. Each oxygen is coordinated to two zinc atoms and one hydrogen atom.[225] The cell parameters for three of the described polymorphs are listed in Table 5.1.

Table 5.1 Cell parameters for $Zn(OH)_2$ polymorphs.

	a (Å)	**b (Å)**	**c (Å)**
β-$Zn(OH)_2$	3.194	3.194	4.714
γ- $Zn(OH)_2$	23.07	8.04	3.30
ε- $Zn(OH)_2$	4.9086	5.1464	8.488

5.5 Conclusions.

Much effort was put into finding a ZnO NC synthesis that would suit the needs of the research described in Chapters 3 and 4. Many methods were explored with the two most successful ones detailed here. To perform the desired experiments with dye molecules, they needed to generate relatively concentrated dispersions that could be reliably reproduced. Because the electronic absorption of the selected **1-CO_2H** dye did not overlap with the adsorption onset of the ZnO, the green emission was not an issue and little effort was expended to investigate that phenomenon further. Although examining $Zn(OH)_2$ as a way to learn more about the formation of ZnO NCs was briefly investigated, it was not taken up in detail, unlike in McCormack research group.[234] It was important to understand the synthetic conditions, formation, growth and properties of ZnO NCs in order to establish a baseline of knowledge on which the rest of the research described in this thesis was built.

References

(1) *Annual Energy Review 2008*, U.S. Department of Energy, 2009.

(2) Shah, A.; Torres, P.; Tscharner, R.; Wyrsch, N.; Keppner, H. *Science* **1999**, *285*, 692-698.

(3) Emery, K.; Myers, D.

(4) McEvoy, A. J.; Grätzel, M. *Sol. Energy Mater. Sol. Cells* **1994**, *32*, 221-227.

(5) Gregg, B. A. *J. Phys. Chem. B* **2003**, *107*, 4688-4698.

(6) Kallmann, H.; Pope, M. *J. Chem. Phys.* **1959**, *30*, 585-586.

(7) Nelson, R. C. *J. Phys. Chem.* **1965**, *69*, 714-718.

(8) Tollin, G.; Kearns, D. R.; Calvin, M. *J. Chem. Phys.* **1960**, *32*, 1013-1019.

(9) O'Regan, B.; Gratzel, M. *Nature* **1991**, *353*, 737-740.

(10) Nazeeruddin, M. K.; Kay, A.; Rodicio, I.; Humphrybaker, R.; Muller, E.; Liska, P.; Vlachopoulos, N.; Gratzel, M. *J. Am. Chem. Soc.* **1993**, *115*, 6382-6390.

(11) Chiba, Y.; Islam, A.; Watanabe, Y.; Komiya, R.; Koide, N.; Han, L. Y. *Jpn. J. Appl. Phys. 2* **2006**, *45*, L638-L640.

(12) Cahen, D.; Hodes, G.; Gratzel, M.; Guillemoles, J. F.; Riess, I. *J. Phys. Chem. B* **2000**, *104*, 2053-2059.

(13) Matthews, D.; Infelta, P.; Grätzel, M. *Sol. Energy Mater. Sol. Cells* **1996**, *44*, 119-155.

(14) Hagfeldt, A.; Gratzel, M. *Acc. Chem. Res.* **2000**, *33*, 269-277.

(15) Ardo, S.; Meyer, G. J. *Chem. Soc. Rev.* **2009**, *38*, 115-164.

(16) Gratzel, M. *Inorg. Chem.* **2005**, *44*, 6841-6851.

(17) Balzani, V.; Bergamini, G.; Campagna, S.; Puntoriero, F. In *Photochemistry and Photophysics of Coordination Compounds I* Springer-Verlag Berlin Heidelberg: 2007; Vol. 280, p 1-36.

(18) Balzani, V.; Moggi, L.; Manfrin, M. F.; Bolletta, F.; Laurence, G. S. *Coord. Chem. Rev.* **1975**, *15*, 321-433.

(19) Caspar, J. V.; Westmoreland, T. D.; Allen, G. H.; Bradley, P. G.; Meyer, T. J.; Woodruff, W. H. *J. Am. Chem. Soc.* **1984**, *106*, 3492-3500.

(20) Kalyanasundaram, K.; Zakeeruddin, S. M.; Nazeeruddin, M. K. *Coord. Chem. Rev.* **1994**, *132*, 259-264.

(21) Giordano, P. J.; Bock, C. R.; Wrighton, M. S.; Interrante, L. V.; Williams, R. F. X. *J. Am. Chem. Soc.* **1977**, *99*, 3187-3189.

(22) Kalyanasundaram, K.; Grätzel, M. *Coord. Chem. Rev.* **1998**, *177*, 347-414.

(23) Hagfeldt, A.; Graetzel, M. *Chem. Rev.* **1995**, *95*, 49-68.

(24) Taratula, O.; Galoppini, E.; Wang, D.; Chu, D.; Zhang, Z.; Chen, H. H.; Saraf, G.; Lu, Y. C. *J. Phys. Chem. B* **2006**, *110*, 6506-6515.

(25) Galoppini, E. *Coord. Chem. Rev.* **2004**, *248*, 1283-1297.

(26) Kilsa, K.; Mayo, E. I.; Brunschwig, B. S.; Gray, H. B.; Lewis, N. S.; Winkler, J. R. *J. Phys. Chem. B* **2004**, *108*, 15640-15651.

(27) Argazzi, R.; Bignozzi, C. A.; Heimer, T. A.; Castellano, F. N.; Meyer, G. J. *Inorg. Chem.* **1994**, *33*, 5741-5749.

(28) Beek, W. J. E.; Janssen, R. A. J. *Adv. Funct. Mater.* **2002**, *12*, 519-525.

(29) Fillinger, A.; Parkinson, B. A. *J. Electrochem. Soc.* **1999**, *146*, 4559-4564.

(30) Fillinger, A.; Soltz, D.; Parkinson, B. A. *J. Electrochem. Soc.* **2002**, *149*, A1146-A1156.

(31) Hasnat, M. A.; Uddin, M. M.; Samed, A. J. F.; Alam, S. S.; Hossain, S. *J. Hazard. Mater.* **2007**, *147*, 471-477.

(32) Mishra, A.; Fischer, M. K. R.; Bauerle, P. *Angew. Chem. Int. Edit.* **2009**, *48*, 2474-2499.

(33) Kim, S.; Choi, H.; Baik, C.; Song, K.; Kang, S. O.; Ko, J. *Tetrahedron* **2007**, *63*, 11436-11443.

(34) Moser, J.; Graetzel, M. *J. Am. Chem. Soc.* **1984**, *106*, 6557-6564.

(35) Murakoshi, K.; Yanagida, S.; Capel, M.; Castner, E. W. In *Nanostruct. Mater.*; American Chemical Society: 1997, p 221-238.

(36) Nasr, C.; Liu, D.; Hotchandani, S.; Kamat, P. V. *J. Phys. Chem.* **1996**, *100*, 11054-11061.

(37) Hara, K.; Kurashige, M.; Ito, S.; Shinpo, A.; Suga, S.; Sayama, K.; Arakawa, H. *Chem. Commun.* **2003**, 252-253.

(38) Hara, K.; Sato, T.; Katoh, R.; Furube, A.; Yoshihara, T.; Murai, M.; Kurashige, M.; Ito, S.; Shinpo, A.; Suga, S.; Arakawa, H. *Adv. Funct. Mater.* **2005**, *15*, 246-252.

(39) Kitamura, T.; Ikeda, M.; Shigaki, K.; Inoue, T.; Anderson, N. A.; Ai, X.; Lian, T.; Yanagida, S. *Chem. Mater.* **2004**, *16*, 1806-1812.

(40) Hwang, S.; Lee, J. H.; Park, C.; Lee, H.; Kim, C.; Park, C.; Lee, M.-H.; Lee, W.; Park, J.; Kim, K.; Park, N.-G.; Kim, C. *Chem. Commun.* **2007**, 4887-4889.

(41) Cherian, S.; Wamser, C. C. *J. Phys. Chem. B* **2000**, *104*, 3624-3629.

(42) Kay, A.; Graetzel, M. *J. Phys. Chem.* **1993**, *97*, 6272-6277.

(43) Odobel, F.; Blart, E.; Lagree, M.; Villieras, M.; Boujtita, H.; El Murr, N.; Caramori, S.; Alberto Bignozzi, C. *J. Mater. Chem.* **2003**, *13*, 502-510.

(44) Schmidt-Mende, L.; Campbell, W. M.; Wang, Q.; Jolley, K. W.; Officer, D. L.; Nazeeruddin, M. K.; Grätzel, M. *ChemPhysChem* **2005**, *6*, 1253-1258.

(45) Tian, H.; Liu, P.-H.; Zhu, W.; Gao, E.; Wu, D.-J.; Cai, S. *J. Mater. Chem.* **2000**, *10*, 2708-2715.

(46) Rochford, J.; Chu, D.; Hagfeldt, A.; Galoppini, E. *J. Am. Chem. Soc.* **2007**, *129*, 4655-4665.

(47) Hao, E.; Anderson, N. A.; Asbury, J. B.; Lian, T. *J. Phys. Chem. B* **2002**, *106*, 10191-10198.

(48) Koops, S. E.; O'Regan, B. C.; Barnes, P. R. F.; Durrant, J. R. *J. Am. Chem. Soc.* **2009**, *131*, 4808-4818.

(49) Robertson, N. *Angew. Chem. Int. Ed.* **2006**, *45*, 2338-2345.

(50) Mishra, A.; Ma, C.-Q.; Bauerle, P. *Chem. Rev.* **2009**, *109*, 1141-1276.

(51) Demanze, F.; Cornil, J.; Garnier, F.; Horowitz, G.; Valat, P.; Yassar, A.; Lazzaroni, R.; Bredas, J.-L. *J. Phys. Chem. B* **1997**, *101*, 4553-4558.

(52) Garcia, P.; Pernaut, J. M.; Hapiot, P.; Wintgens, V.; Valat, P.; Garnier, F.; Delabouglise, D. *J. Phys. Chem.* **1993**, *97*, 513-516.

(53) Hapiot, P.; Demanze, F.; Yassar, A.; Garnier, F. *J. Phys. Chem.* **1996**, *100*, 8397-8401.

(54) Huss, A. S.; Pappenfus, T.; Bohnsack, J.; Burand, M.; Mann, K. R.; Blank, D. A. *J. Phys. Chem. A* **2009**, *113*, 10202-10210.

(55) Qin, H.; Wenger, S.; Xu, M.; Gao, F.; Jing, X.; Wang, P.; Zakeeruddin, S. M.; GraÌˆtzel, M. *J. Am. Chem. Soc.* **2008**, *130*, 9202-9203.

(56) Chen, R.; Yang, X.; Tian, H.; Sun, L. *J. Photoch. Photobio. A* **2007**, *189*, 295-300.

(57) Justin Thomas, K. R.; Hsu, Y.-C.; Lin, J. T.; Lee, K.-M.; Ho, K.-C.; Lai, C.-H.; Cheng, Y.-M.; Chou, P.-T. *Chem. Mater.* **2008**, *20*, 1830-1840.

(58) Zhang, X.-H.; Cui, Y.; Katoh, R.; Koumura, N.; Hara, K. *J. Phys. Chem. C* **2010**, *114*, 18283-18290.

(59) Yum, J.-H.; Hagberg, D. P.; Moon, S.-J.; Karlsson, K. M.; Marinado, T.; Sun, L.; Hagfeldt, A.; Nazeeruddin, M. K.; Grätzel, M. *Angew. Chem. Int. Ed.* **2009**, *48*, 1576-1580.

(60) Koumura, N.; Wang, Z.-S.; Mori, S.; Miyashita, M.; Suzuki, E.; Hara, K. *J. Am. Chem. Soc.* **2006**, *128*, 14256-14257.

(61) Fischer, M. K. R.; Wenger, S.; Wang, M.; Mishra, A.; Zakeeruddin, S. M.; GraÌˆtzel, M.; BaÌˆuerle, P. *Chem. Mater.* **2010**, *22*, 1836-1845.

(62) Benko, G.; Kallioinen, J.; Korppi-Tommola, J. E. I.; Yartsev, A. P.; Sundstrom, V. *J. Am. Chem. Soc.* **2002**, *124*, 489-493.

(63) Kallioinen, J.; Benko, G.; Myllyperkio, P.; Khriachtchev, L.; Skarman, B.; Wallenberg, R.; Tuomikoski, M.; Korppi-Tommola, J.; Sundstrom, V.; Yartsev, A. P. *J. Phys. Chem. B* **2004**, *108*, 6365-6373.

(64) Tachibana, Y.; Nazeeruddin, M. K.; Grätzel, M.; Klug, D. R.; Durrant, J. R. *Chem. Phys.* **2002**, *285*, 127-132.

(65) Wenger, B.; Gratzel, M.; Moser, J.-E. *J. Am. Chem. Soc.* **2005**, *127*, 12150-12151.

(66) Anderson, N. A.; Ai, X.; Lian, T. *J. Phys. Chem. B* **2003**, *107*, 14414-14421.

(67) Asbury, J. B.; Wang, Y. Q.; Lian, T. Q. *J. Phys. Chem. B* **1999**, *103*, 6643-6647.

(68) Bauer, C.; Boschloo, G.; Mukhtar, E.; Hagfeldt, A. *J. Phys. Chem. B* **2001**, *105*, 5585-5588.

(69) Fessenden, R. W.; Kamat, P. V. *J. Phys. Chem.* **1995**, *99*, 12902-12906.

(70) Katoh, R.; Furube, A.; Hara, K.; Murata, S.; Sugihara, H.; Arakawa, H.; Tachiya, M. *J. Phys. Chem. B* **2002**, *106*, 12957-12964.

(71) Quintana, M.; Edvinsson, T.; Hagfeldt, A.; Boschloo, G. *J. Phys. Chem. C* **2007**, *111*, 1035-1041.

(72) Szarko, J. M.; Neubauer, A.; Bartelt, A.; Socaciu-Siebert, L.; Birkner, F.; Schwarzburg, K.; Hannappel, T.; Eichberger, R. *J. Phys. Chem. C* **2008**, *112*, 10542-10552.

(73) Das, S.; Kamat, P. V. *J. Phys. Chem. B* **1998**, *102*, 8954-8957.

(74) Hannappel, T.; Burfeindt, B.; Storck, W.; Willig, F. *J. Phys. Chem. B* **1997**, *101*, 6799-6802.

(75) Moser, J. E.; Noukakis, D.; Bach, U.; Tachibana, Y.; Klug, D. R.; Durrant, J. R.; Humphry-Baker, R.; Gratzel, M. *J. Phys. Chem. B* **1998**, *102*, 3649-3650.

(76) Tachibana, Y.; Moser, J. E.; Gratzel, M.; Klug, D. R.; Durrant, J. R. *J. Phys. Chem.* **1996**, *100*, 20056-20062.

(77) Martinson, A. B. F.; Hamann, T. W.; Pellin, M. J.; Hupp, J. T. *Chemistry-a European Journal* **2008**, *14*, 4458-4467.

(78) Marcus, R. A. *J. Chem. Phys.* **1965**, *43*, 679-701.

(79) Moser, J. E.; Grätzel, M. *Chem. Phys.* **1993**, *176*, 493-500.

(80) Anderson, N. A.; Lian, T. *Annu. Rev. Phys. Chem.* **2005**, *56*, 491-519.

(81) Soedergren, S.; Hagfeldt, A.; Olsson, J.; Lindquist, S.-E. *J. Phys. Chem.* **1994**, *98*, 5552-5556.

(82) Brus, L. *Physical Review B* **1996**, *53*, 4649.

(83) Gaal, D. A.; McGarrah, J. E.; Liu, F.; Cook, J. E.; Hupp, J. T. *Photochemical & Photobiological Sciences* **2004**, *3*, 240-245.

(84) Nelson, J. *Physical Review B* **1999**, *59*, 15374.

(85) Ferber, J.; Stangl, R.; Luther, J. *Sol. Energy Mater. Sol. Cells* **1998**, *53*, 29-54.

(86) Papageorgiou, N.; Grätzel, M.; Infelta, P. P. *Sol. Energy Mater. Sol. Cells* **1996**, *44*, 405-438.

(87) Levy, B.; Liu, W.; Gilbert, S. E. *J. Phys. Chem. B* **1997**, *101*, 1810-1816.

(88) Asbury, J. B.; Ellingson, R. J.; Ghosh, H. N.; Ferrere, S.; Nozik, A. J.; Lian, T. *J. Phys. Chem. B* **1999**, *103*, 3110-3119.

(89) Haque, S. A.; Tachibana, Y.; Willis, R. L.; Moser, J. E.; Gratzel, M.; Klug, D. R.; Durrant, J. R. *J. Phys. Chem. B* **2000**, *104*, 538-547.

(90) Kuang, D.; Ito, S.; Wenger, B.; Klein, C.; Moser, J.-E.; Humphry-Baker, R.; Zakeeruddin, S. M.; Gratzel, M. *J. Am. Chem. Soc.* **2006**, *128*, 4146-4154.

(91) Chou, T. P.; Zhang, Q.; Cao, G. *J. Phys. Chem. C* **2007**, *111*, 18804-18811.

(92) Keis, K.; Lindgren, J.; Lindquist, S.-E.; Hagfeldt, A. *Langmuir* **2000**, *16*, 4688-4694.

(93) Watson, D. F.; Meyer, G. J. *Annu. Rev. Phys. Chem.* **2005**, *56*, 119-156.

(94) Westermark, K.; Rensmo, H.; Siegbahn, H.; Keis, K.; Hagfeldt, A.; Ojamae, L.; Persson, P. *J. Phys. Chem. B* **2002**, *106*, 10102-10107.

(95) Ferrere, S.; Zaban, A.; Gregg, B. A. *J. Phys. Chem. B* **1997**, *101*, 4490-4493.

(96) Huang, J.; Stockwell, D.; Boulesbaa, A.; Guo, J. C.; Lian, T. Q. *Journal of Physical Chemistry C* **2008**, *112*, 5203-5212.

(97) Park, N. G.; van de Lagemaat, J.; Frank, A. J. *J. Phys. Chem. B* **2000**, *104*, 8989-8994.

(98) Tang, H.; Prasad, K.; Sanjinés, R.; Lévy, F. *Sensors and Actuators B: Chemical* **1995**, *26*, 71-75.

(99) Ghosh, H. N. *The Journal of Chemical Sciences* **2007**, *119*, 205-215.

(100) Ghosh, H. N.; Asbury, J. B.; Lian, T. *J. Phys. Chem. B* **1998**, *102*, 6482-6486.

(101) Kamat, P. V. *Journal of Photochemistry* **1985**, *28*, 513-524.

(102) Kamat, P. V. *Chem. Rev.* **1993**, *93*, 267-300.

(103) Kaniyankandy, S.; Verma, S.; Mondal, J. A.; Palit, D. K.; Ghosh, H. N. *J. Phys. Chem. C* **2009**, *113*, 3593-3599.

(104) Moser, J.; Grätzel, M.; Sharma, D. K.; Serpone, N. *Helv. Chim. Acta* **1985**, *68*, 1686-1690.

(105) Rehm, J. M.; McLendon, G. L.; Nagasawa, Y.; Yoshihara, K.; Moser, J.; Gratzel, M. *J. Phys. Chem.* **1996**, *100*, 9577-9578.

(106) Willner, I.; Eichen, Y.; Frank, A. J.; Fox, M. A. *J. Phys. Chem.* **1993**, *97*, 7264-7271.

(107) Zhang, H.; Zhou, Y.; Zhang, M.; Shen, T.; Li, Y.; Zhu, D. *J. Phys. Chem. B* **2002**, *106*, 9597-9603.

(108) Benko, G.; Hilgendorff, M.; Yartsev, A. P.; Sundstrom, V. *J. Phys. Chem. B* **2001**, *105*, 967-974.

(109) Hilgendorff, M.; Sundstrom, V. *J. Phys. Chem. B* **1998**, *102*, 10505-10514.

(110) Dang, X. J.; Hupp, J. T. *J. Am. Chem. Soc.* **1999**, *121*, 8399-8400.

(111) Dang, X. J.; Hupp, J. T. *J. Photoch. Photobio. A* **2001**, *143*, 251-256.

(112) Gaal, D. A.; Hupp, J. T. *J. Am. Chem. Soc.* **2000**, *122*, 10956-10963.

(113) Ford, W. E.; Rodgers, M. A. J. *J. Phys. Chem.* **1994**, *98*, 3822-3831.

(114) Mulvaney, P.; Grieser, F.; Meisel, D. *Langmuir* **1990**, *6*, 567-572.

(115) Asbury, J. B.; Hao, E.; Wang, Y.; Ghosh, H. N.; Lian, T. *J. Phys. Chem. B* **2001**, *105*, 4545-4557.

(116) Li, B.; Wang, L.; Kang, B.; Wang, P.; Qiu, Y. *Sol. Energy Mater. Sol. Cells* **2006**, *90*, 549-573.

(117) Jensen, R. A.; Van Ryswyk, H.; She, C.; Szarko, J. M.; Chen, L. X.; Hupp, J. T. *Langmuir* **2009**, *26*, 1401-1404.

(118) Huss, A. S.; Bierbaum, A.; Chitta, R.; Ceckanowicz, D. J.; Mann, K. R.; Gladfelter, W. L.; Blank, D. A. *J. Am. Chem. Soc.* **2010**, *132*, 13963-13965.

(119) Huber, R.; Moser, J. E.; Grätzel, M.; Wachtveitl, J. *Chem. Phys.* **2002**, *285*, 39-45.

(120) Kamat, P. V. *J. Phys. Chem.* **1989**, *93*, 859-864.

(121) Pagba, C.; Zordan, G.; Galoppini, E.; Piatnitski, E. L.; Hore, S.; Deshayes, K.; Piotrowiak, P. *J. Am. Chem. Soc.* **2004**, *126*, 9888-9889.

(122) Ramakrishna, G.; Ghosh, H. N. *J. Phys. Chem. A* **2002**, *106*, 2545-2553.

(123) Verma, S.; Kar, P.; Das, A.; Palit, D. K.; Ghosh, H. N. *J. Phys. Chem. C* **2008**, *112*, 2918-2926.

(124) Antony, J.; Chen, X. B.; Morrison, J.; Bergman, L.; Qiang, Y.; McCready, D. E.; Engelhard, M. H. *Appl. Phys. Lett.* **2005**, *87*, 3.

(125) Bahnemann, D. W.; Kormann, C.; Hoffmann, M. R. *J. Phys. Chem.* **1987**, *91*, 3789-3798.

(126) Kim, C. G.; Sung, K.; Chung, T.-M.; Jung, D. Y.; Kim, Y. *Chem. Commun.* **2003**, 2068-2069.

(127) Luo, B.; Rossini, J. E.; Gladfelter, W. L. *Langmuir* **2009**, *25*, 13133-13141.

(128) Meulenkamp, E. A. *J. Phys. Chem. B* **1998**, *102*, 5566-5572.

(129) Rataboul, F.; Nayral, C.; Casanove, M.-J.; Maisonnat, A.; Chaudret, B. *J. Organomet. Chem.* **2002**, *643-644*, 307-312.

(130) Schwartz, D. A.; Norberg, N. S.; Nguyen, Q. P.; Parker, J. M.; Gamelin, D. R. *J. Am. Chem. Soc.* **2003**, *125*, 13205-13218.

(131) Spanhel, L.; Anderson, M. A. *J. Am. Chem. Soc.* **1991**, *113*, 2826-2833.

(132) Wong, E. M.; Bonevich, J. E.; Searson, P. C. *J. Phys. Chem. B* **1998**, *102*, 7770-7775.

(133) Huss, A. S.; Bierbaum, A.; Chitta, R.; Ceckanowicz, D. J.; Mann, K. R.; Gladfelter, W. L.; Blank, D. A. *J. Am. Chem. Soc.* **2010**, *132*, submitted for publication.

(134) Pappenfus, T. M.; Mann, K. R. *Org. Lett.* **2002**, *4*, 3043-3046.

(135) Rossini, J. E.; Huss, A. S.; Bohnsack, J. N.; Blank, D. A.; Mann, K. R.; Gladfelter, W. L. *J. Phys. Chem. C* **2011**, *115*, 11-17.

(136) Sauve, G.; Cass, M. E.; Coia, G.; Doig, S. J.; Lauermann, I.; Pomykal, K. E.; Lewis, N. S. *J. Phys. Chem. B* **2000**, *104*, 6821-6836.

(137) Kamat, P. V.; Patrick, B. *J. Phys. Chem.* **1992**, *96*, 6829-6834.

(138) Koch, U.; Fojtik, A.; Weller, H.; Henglein, A. *Chem. Phys. Lett.* **1985**, *122*, 507-510.

(139) Brus, L. *J. Phys. Chem.* **1986**, *90*, 2555-2560.

(140) Brus, L. E. *J. Chem. Phys.* **1984**, *80*, 4403-4409.

(141) Rossetti, R.; Ellison, J. L.; Gibson, J. M.; Brus, L. E. *J. Chem. Phys.* **1984**, *80*, 4464-4469.

(142) Viswanatha, R.; Sapra, S.; Satpati, B.; Satyam, P. V.; Dev, B. N.; Sarma, D. D. *J. Mater. Chem.* **2004**, *14*, 661-668.

(143) van Dijken, A.; Meulenkamp, E. A.; Vanmaekelbergh, D.; Meijerink, A. *J. Phys. Chem. B* **2000**, *104*, 1715-1723.

(144) Vanheusden, K.; Warren, W. L.; Seager, C. H.; Tallant, D. R.; Voigt, J. A.; Gnade, B. E. *J. Appl. Phys.* **1996**, *79*, 7983-7990.

(145) Cheng, H. M.; Hsu, H. C.; Chen, S. L.; Wu, W. T.; Kao, C. C.; Lin, L. J.; Hsieh, W. F. *J. Cryst. Growth* **2005**, *277*, 192-199.

(146) Keis, K.; Bauer, C.; Boschloo, G.; Hagfeldt, A.; Westermark, K.; Rensmo, H.; Siegbahn, H. *J. Photoch. Photobio. A* **2002**, *148*, 57-64.

(147) Horiuchi, H.; Katoh, R.; Hara, K.; Yanagida, M.; Murata, S.; Arakawa, H.; Tachiya, M. *J. Phys. Chem. B* **2003**, *107*, 2570-2574.

(148) Hugot-Le Goff, A.; Joiret, S.; Falaras, P. *J. Phys. Chem. B* **1999**, *103*, 9569-9575.

(149) Wang, Z.-S.; Huang, C.-H.; Huang, Y.-Y.; Hou, Y.-J.; Xie, P.-H.; Zhang, B.-W.; Cheng, H.-M. *Chem. Mater.* **2001**, *13*, 678-682.

(150) Ghanem, R. *Spectrochimica Acta Part a-Molecular and Biomolecular Spectroscopy* **2009**, *72*, 455-459.

(151) Huss, A. S.; Rossini, J. E.; Mann, K. R.; Gladfelter, W. L.; Blank, D. A. *In Preparation* **2010**, *X*, X-X.

(152) Galoppini, E.; Rochford, J.; Chen, H.; Saraf, G.; Lu, Y.; Hagfeldt, A.; Boschloo, G. *J. Phys. Chem. B* **2006**, *110*, 16159-16161.

(153) Gonzalez-Valls, I.; Lira-Cantu, M. *Energy & Environmental Science* **2009**, *2*, 19-34.

(154) Schmidt-Mende, L.; MacManus-Driscoll, J. L. *Mater. Today* **2007**, *10*, 40-48.

(155) Zhang, Q.; Dandeneau, C. S.; Zhou, X.; Cao, G. *Adv. Mater.* **2009**, *21*, 4087-4108.

(156) Katoh, R.; Furube, A.; Yoshihara, T.; Hara, K.; Fujihashi, G.; Takano, S.; Murata, S.; Arakawa, H.; Tachiya, M. *J. Phys. Chem. B* **2004**, *108*, 4818-4822.

(157) Willis, R. L.; Olson, C.; O'Regan, B.; Lutz, T.; Nelson, J.; Durrant, J. R. *J. Phys. Chem. B* **2002**, *106*, 7605-7613.

(158) Andelman, T.; Gong, Y.; Polking, M.; Yin, M.; Kuskovsky, I.; Neumark, G.; O'Brien, S. *J. Phys. Chem. B* **2005**, *109*, 14314-14318.

(159) Kahn, M. L.; Monge, M.; Collière, V.; Senocq, F.; Maisonnat, A.; Chaudret, B. *Adv. Funct. Mater.* **2005**, *15*, 458-468.

(160) Meulenkamp, E. A. *J. Phys. Chem. B* **1998**, *102*, 5566-5572.

(161) Gebeyehu, D.; Brabec, C. J.; Sariciftci, N. S.; Vangeneugden, D.; Kiebooms, R.; Vanderzande, D.; Kienberger, F.; Schindler, H. *Synth. Met.* **2001**, *125*, 279-287.

(162) Glenis, S.; Benz, M.; LeGoff, E.; Kanatzidis, M. G.; DeGroot, D. C.; Schindler, J. L.; Kannewurf, C. R. *Synth. Met.* **1995**, *75*, 213-221.

(163) Hagberg, D. P.; Yum, J.-H.; Lee, H.; De Angelis, F.; Marinado, T.; Karlsson, K. M.; Humphry-Baker, R.; Sun, L.; Hagfeldt, A.; GrÃ¤tzel, M.; Nazeeruddin, M. K. *J. Am. Chem. Soc.* **2008**, *130*, 6259-6266.

(164) Houarner-Rassin, C.; Blart, E.; Buvat, P.; Odobel, F. *J. Photoch. Photobio. A* **2007**, *186*, 135-142.

(165) Houarner-Rassin, C.; Blart, E.; Buvat, P.; Odobel, F. *Photochemical & Photobiological Sciences* **2008**, *7*, 789-793.

(166) Huang, S.-T.; Hsu, Y.-C.; Yen, Y.-S.; Chou, H. H.; Lin, J. T.; Chang, C.-W.; Hsu, C.-P.; Tsai, C.; Yin, D.-J. *J. Phys. Chem. C* **2008**, *112*, 19739-19747.

(167) Huisman, C. L.; Huijser, A.; Donker, H.; Schoonman, J.; Goossens, A. *Macromolecules* **2004**, *37*, 5557-5564.

(168) Li, R.; Lv, X.; Shi, D.; Zhou, D.; Cheng, Y.; Zhang, G.; Wang, P. *J. Phys. Chem. C* **2009**, *113*, 7469-7479.

(169) Saito, Y.; Azechi, T.; Kitamura, T.; Hasegawa, Y.; Wada, Y.; Yanagida, S. *Coord. Chem. Rev.* **2004**, *248*, 1469-1478.

(170) Smestad, G. P.; Spiekermann, S.; Kowalik, J.; Grant, C. D.; Schwartzberg, A. M.; Zhang, J.; Tolbert, L. M.; Moons, E. *Sol. Energy Mater. Sol. Cells* **2003**, *76*, 85-105.

(171) Casado, J.; Ruiz Delgado, M. C.; Rey Merchán, M. C.; Hernández, V.; López Navarrete, J. T.; Pappenfus, T. M.; Williams, N.; Stegner, W. J.; Johnson, J. C.; Edlund, B. A.; Janzen, D. E.; Mann, K. R.; Orduna, J.; Villacampa, B. *Chemistry – A European Journal* **2006**, *12*, 5458-5470.

(172) Xu, M.; Wenger, S.; Bala, H.; Shi, D.; Li, R.; Zhou, Y.; Zakeeruddin, S. M.; GraÌˆtzel, M.; Wang, P. *J. Phys. Chem. C* **2009**, *113*, 2966-2973.

(173) Liang, Y.; Ponte Goncalves, A. M.; Negus, D. K. *J. Phys. Chem.* **1983**, *87*, 1-4.

(174) Kamat, P. V.; Dimitrijevic, N. M.; Fessenden, R. W. *J. Phys. Chem.* **1987**, *91*, 396-401.

(175) Pileni, M.; Lisiecki, I.; Motte, L.; Petit, C. *Res. Chem. Intermed.* **1992**, *17*, 101-113.

(176) Ramsden, J. J.; Webber, S. E.; Graetzel, M. *J. Phys. Chem.* **1985**, *89*, 2740-2743.

(177) Lewis, J. E.; Maroncelli, M. *Chem. Phys. Lett.* **1998**, *282*, 197-203.

(178) Freedman, D. A.; Gill, T. P.; Blough, A. M.; Koefod, R. S.; Mann, K. R. *Inorg. Chem.* **1997**, *36*, 95-102.

(179) Wells, N. P.; Boudouris, B. W.; Hillmyer, M. A.; Blank, D. A. *Journal of Physical Chemistry C* **2007**, *111*, 15404-15414.

(180) Kahlow, M. A.; Jarzeba, W.; DuBruil, T. P.; Barbara, P. F. *Rev. Sci. Instrum.* **1988**, *59*, 1098-1109.

(181) Grebner, D.; Helbig, M.; Rentsch, S. *J. Phys. Chem.* **1995**, *99*, 16991-16998.

(182) Rossi, R.; Ciofalo, M.; Carpita, A.; Ponterini, G. *J. Photoch. Photobio. A* **1993**, *70*, 59-67.

(183) Lakowicz, J. R. *Principles of Fluorescence Spectroscopy*; 3 ed.; Springer US: Baltimore, MD, 2006.

(184) Ravirajan, P.; PeirÃ³, A. M.; Nazeeruddin, M. K.; Graetzel, M.; Bradley, D. D. C.; Durrant, J. R.; Nelson, J. *J. Phys. Chem. B* **2006**, *110*, 7635-7639.

(185) Xiong, W.; Laaser, J. E.; Paoprasert, P.; Franking, R. A.; Hamers, R. J.; Gopalan, P.; Zanni, M. T. *J. Am. Chem. Soc.* **2009**, *131*, 18040-18041.

(186) Chukharev, V.; Tkachenko, N.; Efimov, A.; Vainiotalo, P.; Lemmetyinen, H. *Photochemical & Photobiological Sciences* **2003**, *2*, 1044-1049.

(187) Ramakrishna, G.; Das, A.; Ghosh, H. N. *Langmuir* **2004**, *20*, 1430-1435.

(188) Cherepy, N. J.; Smestad, G. P.; Gratzel, M.; Zhang, J. Z. *J. Phys. Chem. B* **1997**, *101*, 9342-9351.

(189) Ramakrishna, G.; Singh, A. K.; Palit, D. K.; Ghosh, H. N. *J. Phys. Chem. B* **2004**, *108*, 4775-4783.

(190) Ramakrishna, G.; Ghosh, H. N.; Singh, A. K.; Palit, D. K.; Mittal, J. P. *J. Phys. Chem. B* **2001**, *105*, 12786-12796.

(191) Ramakrishna, G.; Singh, A. K.; Palit, D. K.; Ghosh, H. N. *J. Phys. Chem. B* **2004**, *108*, 12489-12496.

(192) Ghosh, H. N. *J. Phys. Chem. B* **1999**, *103*, 10382-10387.

(193) Ramakrishna, G.; Ghosh, H. N. *J. Phys. Chem. B* **2001**, *105*, 7000-7008.

(194) Redmond, G.; O'Keeffe, A.; Burgess, C.; MacHale, C.; Fitzmaurice, D. *J. Phys. Chem.* **1993**, *97*, 11081-11086.

(195) Ozgur, U.; Alivov, Y. I.; Liu, C.; Teke, A.; Reshchikov, M. A.; Dogan, S.; Avrutin, V.; Cho, S. J.; Morkoc, H. *J. Appl. Phys.* **2005**, *98*, 041301-103.

(196) Demichelis, F.; E. Minetti-Mezzetti; V. Smurro; Tagliaferro, A.; Tresso, E. *J. Phys. D: Appl. Phys.* **1985**, *18*, 1825-1832.

(197) Haase, M.; Weller, H.; Henglein, A. *J. Phys. Chem.* **1988**, *92*, 482-487.

(198) Monge, M.; Kahn, M. L.; Maisonnat, A.; Chaudret, B. *Angew. Chem. Int. Ed.* **2003**, *42*, 5321-5324.

(199) Pesika, N. S.; Hu, Z. S.; Stebe, K. J.; Searson, P. C. *J. Phys. Chem. B* **2002**, *106*, 6985-6990.

(200) Yin, M.; Gu, Y.; Kuskovsky, I. L.; Andelman, T.; Zhu, Y.; Neumark, G. F.; O'Brien, S. *J. Am. Chem. Soc.* **2004**, *126*, 6206-6207.

(201) Guo, J. C. **2002**.

(202) Carnes, C. L.; Klabunde, K. J. *Langmuir* **2000**, *16*, 3764-3772.

(203) Shim, M.; Guyot-Sionnest, P. *J. Am. Chem. Soc.* **2001**, *123*, 11651-11654.

(204) Lao, J. Y.; Wen, J. G.; Ren, Z. F. *Nano Lett.* **2002**, *2*, 1287-1291.

(205) Gao, P. X.; Ding, Y.; Wang, Z. L. *Nano Lett.* **2003**, *3*, 1315-1320.

(206) Kong, X. Y.; Wang, Z. L. *Nano Lett.* **2003**, *3*, 1625-1631.

(207) Lyu, S. C.; Zhang, Y.; Lee, C. J.; Ruh, H.; Lee, H. J. *Chem. Mater.* **2003**, *15*, 3294-3299.

(208) Boyle, T. J.; Bunge, S. D.; Andrews, N. L.; Matzen, L. E.; Sieg, K.; Rodriguez, M. A.; Headley, T. J. *Chem. Mater.* **2004**, *16*, 3279-3288.

(209) Cozzoli, P. D.; Kornowski, A.; Weller, H. *J. Phys. Chem. B* **2005**, *109*, 2638-2644.

(210) Lao, J. Y.; Huang, J. Y.; Wang, D. Z.; Ren, Z. F. *Nano Lett.* **2003**, *3*, 235-238.

(211) Pinna, N.; Garnweitner, G.; Antonietti, M.; Niederberger, M. *J. Am. Chem. Soc.* **2005**, *127*, 5608-5612.

(212) Wang, X.; Ding, Y.; Summers, C. J.; Wang, Z. L. *J. Phys. Chem. B* **2004**, *108*, 8773-8777.

(213) Li, H.; Wang, J.; Liu, H.; Yang, C.; Xu, H.; Li, X.; Cui, H. *Vacuum* **2004**, *77*, 57-62.

(214) Silva, R. F.; Zaniquelli, M. E. D. *Thin Solid Films* **2004**, *449*, 86-93.

(215) Luo, B.; Kucera, B. E.; Gladfelter, W. L. *Polyhedron* **2006**, *25*, 279-285.

(216) Poirier, G. E.; Tarlov, M. J. *Langmuir* **1994**, *10*, 2853-2856.

(217) Belman, N.; Acharya, S.; Konovalov, O.; Vorobiev, A.; Israelachvili, J.; Efrima, S.; Golan, Y. *Nano Lett.* **2008**, *8*, 3858-3864.

(218) Belman, N.; Israelachvili, J. N.; Li, Y.; Safinya, C. R.; Bernstein, J.; Golan, Y. *Nano Lett.* **2009**, *9*, 2088-2093.

(219) George, M.; Weiss, R. G. *J. Am. Chem. Soc.* **2001**, *123*, 10393-10394.

(220) George, M.; Weiss, R. G. *Langmuir* **2002**, *18*, 7124-7135.

(221) George, M.; Weiss, R. G. *Langmuir* **2003**, *19*, 1017-1025.

(222) Guo, L.; Yang, S.; Yang, C.; Yu, P.; Wang, J.; Ge, W.; Wong, G. K. L. *Appl. Phys. Lett.* **2000**, *76*, 2901-2903.

(223) Aigueperse, J.; Arghiropoulos, B.; Teichner, S. *Compt. rend.* **1960**, *250*, 550-2.

(224) Baneeva, M. I.; Popova, S. V. *Geokhimiya* **1969**, 1014-16.

(225) Christensen, A. N. *Acta Chem. Scand.* **1969**, *23*, 2016-2020.

(226) Feitknecht, W. *Helv. Chim. Acta* **1930**, *13*, 314-345.

(227) Schnering, H. G. *Z. Anorg. Allg. Chem.* **1964**, *330*, 170-178.

(228) Holas, T.; Zbytovska, J.; Vavrova, K.; Berka, P.; Madlova, M.; Klimentova, J.; Hrabalek, A. *Thermochim. Acta* **2006**, *441*, 116-123.

(229) Hu, Z.; Oskam, G.; Searson, P. C. *J. Colloid Interface Sci.* **2003**, *263*, 454-460.

(230) Srivastava, O. K.; Secco, E. A. *Can. J. Chem.* **1967**, *45*, 579-583.

(231) Brus, L. E. *J. Lumin.* **1984**, *31-32*, 381-384.

(232) Giovanoli, R.; Oswald, H. R.; Feitknecht, W. *Helv. Chim. Acta* **1966**, *49*, 1971-83.

(233) van Dijken, A.; Meulenkamp, E. A.; Vanmaekelbergh, D.; Meijerink, A. *J. Phys. Chem. B* **2000**, *104*, 4355-4360.

(234) McBride, R. A.; Kelly, J. M.; McCormack, D. E. *J. Mater. Chem.* **2003**, *13*, 1196-1201.